# POLITECNICO DI TORINO

Energy Department

Master’s degree in Energy and Nuclear Engineering

Innovation in energy production

Master’s degree Thesis

# *Experimental selection of optimal chemical looping conditions using iron oxides for applications in CSP systems*

Supervisors:

Prof. Massimo Santarelli

Dr. Domenico Ferrero

Dr. Davide Papurello

Candidate:

Serena Colombo

March 2021

*Ai miei genitori,*
*per la loro costante dedizione*
*nel rendermi felice*

*A Ilaria,*
*il regalo più bello che mamma e papà*
*mi abbiano mai fatto*

*A Federico,*
*forza e centro gravitazionale*
*del mio mondo*

*“Pour ce qui est de l’avenir, il ne s’agit pas de le prévoir, mais de le rendre possible”*

**Antoine de Saint Exupéry**, *Citadelle, 1948*

# ABSTRACT

The persistent rise of the average temperature of the Earth shows that global warming is an obvious fact. This is connected to increasing greenhouse gas (GHG) emissions, pollution and the resulting climate changes, causing alterations to the environment. All this can be traced back to the use of fossil fuels as the world's main energy source. One alternative to counteract global warming is to investigate technologies for capturing $CO_2$ already generated by current fossil fuel energy systems and develop methods to convert $CO_2$ into useful chemicals or combustible gases. Among the possible methods, one of the most promising is the chemical looping process composed of two-step thermochemical cycles for $CO_2$ conversion to syngas.

The objective of this dissertation is to investigate the feasibility to perform chemical looping processes for syngas production in the CSP system located on the rooftop of the Energy Center building. In this way, it would be possible to store intermittent solar energy in the form of chemical energy through the conversion of $CO_2$ molecules. For this purpose, at first, a geometrical optics model and an interconnected heat transfer model have been developed, using COMSOL Multiphysics, to simulate and predict the temperature evolution of the receiver for the four seasons. Then, to find the best set-up of the system, different chemical looping processes at different temperatures, $CO_2$ concentrations and reducing conditions were investigated at the $CO_2$ Circle Lab (CCL) in Environment Park. An electrically heated tubular furnace is utilized to simulate a real solar thermochemical reactor and iron oxides powder is used as the oxygen carrier.

The isothermal chemical looping cycle at 1000 °C with 5% $H_2$ in reduction and 40% $CO_2$ in oxidation with $N_2$ performs best, among all those analyzed, in terms of process yield. The total CO production during a single cycle is 0.00422 mol/g, while the obtained CO peak production rate is 27.63 µmol/g/s. In a second moment, the CO produced can be mixed with $H_2$ with a controlled $H_2$/CO ratio. Based on the temperature evolution prediction of the Energy Center reactor obtained from the COMSOL model, is possible to consider the opportunity to translate this ideal test in real-world condition. A different minimum number of cycles per day can be performed depending on the weather season, except for winter, for which the above process is not applicable due to the low temperatures. In the last case, it can be considered to replicate the process but at a lower temperature and consequently with a lower process yield expected.

***Key-words:*** Chemical looping; $CO_2$ conversion; syngas; solar energy; energy storage; CSP; COMSOL model; iron oxides; thermal reduction; $H_2$ assisted reduction.

# CONTENTS

# LIST OF FIGURES

# LIST OF TABLES

# Acronyms

| | |
|---|---|
| GHG | Greenhouse Gas |
| CCS | Carbon Capture and Storage |
| DME | Dimethyl ether |
| FT | Fischer-Tropsch |
| HT | High temperature |
| SOEC | Solid oxide electrolyzer |
| CSP | Concentrated solar power |
| WGS | Water-gas shift |
| SMR | Steam methane reforming |
| ASU | Air separation unit |
| CCU | Carbon Capture and Utilization |
| CL | Chemical Looping |
| TR | Thermal reduction |
| MeO | Metal oxide |
| WS | Water splitting |
| CDS | Carbon dioxide splitting |
| OC | Oxygen carrier |
| ETH | Swiss Federal Institute of Technology |
| PSI | Paul Scherrer Institute |
| PROMES | Processes, Materials and Solar Energy laboratory |
| YSZ | Yttria-stabilized zirconia |
| CLRM | Chemical looping reforming of methane |
| CLC | Chemical looping combustion |
| CLDH | Chemical looping dry reforming with hydrogen production |
| TGA | Thermogravimetric analysis |
| HTF | Heat transfer fluid |
| PT | Parabolic Trough |
| LF | Linear Fresnel |
| DE | Dish-Engine |
| CR | Central Receivers |
| DIR | Directly-irradiated receiver |
| IIR | Indirectly-irradiated receiver |
| SNL | Sandia National Laboratories |
| MPSZ | Magnesia-Partially-Stabilized Zirconia |
| CR5 | Counter-Rotating-Ring Receiver-Reactor-Recuperator |
| RPM | Revolutions per minute |
| EC-Lab | Energy Center Lab |
| EC | Energy Center |
| CCL | $CO_2$ Circle Lab |
| MFC | Mass Flow Controller |
| RES | Renewable Energy Sources |
| SCADA | Supervisory control and data acquisition |
| TCD | Thermal Conductivity Detector |
| IR | Infrared Detector |
| FEM | Finite Element Method |
| GOP | Geometrical Optics |
| XRD | X-ray diffraction |
| SEM | Scanning electron microscope |

# 1 INTRODUCTION

Nowadays fossil fuels are the main players for the fulfilment of the energy demand worldwide. These are associated with increasing greenhouse gas (GHG) emissions, pollution, global warming and the resulting climate changes, causing alternations to the environment. “Climate change is a problem of every country on every continent. It is disrupting national economies and affecting lives. Weather patterns are changing, sea levels are rising, and weather events are becoming more extreme” [1]. Among all the fossil fuels products, $CO_2$ seems to be the main contributor to the greenhouse effect. This condition has arisen after the industrial revolution when it was no longer possible to balance the carbon dioxide due to the increasing usage of fossil fuels [2]. The Paris Agreement (2016) principal aim is to strengthen the global response to the threat of climate change by keeping a global temperature rise this century below 2 °C above pre-industrial levels and to pursue efforts to limit the temperature increase even further to 1.5 °C. To achieve this long-term temperature goal, countries aim to reach global peaking of greenhouse gas emissions as soon as possible to achieve a climate-neutral world by mid-century [3]. Today we are still too far from the possible realization of this target: 2019 was the second warmest year on record and global temperatures are projected to rise by up to 3.2 °C by the year 2100. Moreover, investment in fossil fuels continues to be higher than investment in climate activities [1].

In this context, one of the biggest challenges of the 21st century is the transition from fossil fuels to renewables energy systems [4]. As long as fast measures for this transition are not adopted, it is important to find temporary solutions to contain the ecological imbalance linked to the $CO_2$ emissions. Carbon Capture and Storage (CCS) processes can represent a valid short-term solution, storing the captured carbon dioxide in depleted oil wells or deep oceans. It has to be highlighted that, on a long-term basis, this procedure is not completely safe for the possible damages linked to the storage sites. $CO_2$ can also be used in enhanced oil recovery considering, however, that the recovery rates are as low as 10% [5].

Taking into account all the negative aspects concerning CCS, the aim to sequestrate $CO_2$ can be coupled to a re-utilization of the same, using it to produce useful products, such as syngas. This can be then used as an alternative fuel source or raw material for industrial processes that still rely on fossil fuels [2]. Producing energy without dangerous emissions and no damage to the environment when burning, syngas ($H_2$ and CO) has the greatest potential to replace fossil fuels [6]. It can be also used as the raw material for different chemical products such as dimethyl ether (DME), ethanol and methanol. Moreover, through the well-known Fischer-Tropsch (FT) technology, syngas can be used for the productions of synthetic liquid fuel [7].

50,000 EJ per year is the harvestable solar energy potential compared with a word energy consumption of "only" 504 EJ per year [4]. This means that using only solar energy, the world would be able to satisfy all its own needs. However, it has to be considered that solar energy is intermitted, stochastic and not equally distributed and so a storage system, for use during non-solar periods, is required to match the society energy demand. In this framework, converting solar energy (when available) into storable and transportable fuels is an attractive solution [8]. When a fuel is produced using solar energy is termed solar fuels [5]. Among all the possible pathways, the production of hydrogen and syngas seems to be a really good choice for storing intermittent renewable energy. Nowadays syngas is produced using biomass, coal and natural gas in two different carbonaceous processes: reforming and gasification [8]. These conventional processes have some drawbacks linked to the use of fossil fuels for the combustion step and the associated carbon dioxide emissions. If instead solar energy is used as an external source of heat to drive these processes, the problem of the $CO_2$ emissions will be overcome [7]. The syngas production coupled with solar energy, constituting properly a storage system, become even more attractive if $CO_2$ can be used in the process, removing it from the atmosphere. With this aim, non-carbonaceous routes can be crossed, such as high temperature (HT) electrolysis, thermolysis and thermochemical cycles, by which syngas is obtained through the solar splitting of $H_2O$ and $CO_2$ [8]. Figure 1 illustrates all the possible routes for solar syngas production.

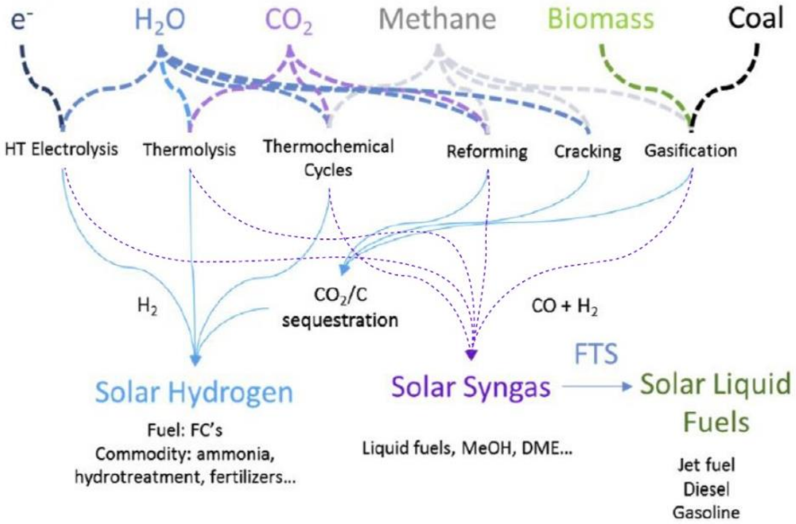

*Figure 1 | Different solar thermal routes for solar syngas production [8].*

The HT electrolysis uses electrical energy to split $H_2O$ and $CO_2$ molecules into a solid oxide electrolyzer (SOEC). This is composed of two noble-metal coated electrodes (anode and cathode) with an electrolyte in between, which allows ions transfer. The principal negative aspect of the process is the conversion from solar energy into an electrical one, losing efficiency. On the other hand, the electrolyzer size can be really small, increasing the system functionality.

To overcome the problem of the efficiency reduction linked to the energy conversion we need to move to thermolysis and thermochemical cycles for syngas production. It is important to highlight that in these cases, as the opposite condition, the system size will be bigger (trade-off).

Thermolysis of $H_2O$ and $CO_2$ requires ultra-high temperatures (> 2500 K) at which separation of gaseous products is needed to avoid recombination. If this does not happen, an explosive mixture will be formed. Both for temperature and possible explosive mixture formation, the realization of the process is really difficult [9].

Thermochemical cycles overcome these disadvantages, reducing process temperature and by-passing the separation problem through two-step thermochemical cycles based on metal oxide redox reactions [9]. The first step of the cycle consists of reducing the metal oxide (also called oxygen carrier) with the help of a high-temperature heat source (endothermic reaction). Solar energy through concentrated solar power (CSP) system is used to drive the reaction. The CSP system utilizes lenses or mirrors and tracking systems to focus a large area of sunlight into a small concentrated beam [7]. In the second step, which is exothermic, the operative temperature is lower. The reduced metal oxide will be oxidized thanks to the simultaneous interaction with $H_2O$ and $CO_2$ that, in contrast, are reduced to syngas. $H_2O$ and $CO_2$ can be also sent in two different moments, allowing the separate production of $H_2$ and CO which, in a second moment, can be mixed with a controlled $H_2/CO$ ratio [4]. At the end of the cycle, solar fuel is produced, storing on it all the energy potential coming from the sun, and the $CO_2$ is transformed. After the oxidation, the metal oxide can return to the reduction step ready to face another cycle.

Is also possible to mix carbonaceous and non-carbonaceous pathways, coupling a thermochemical cycle with a reducing agent (like methane) that will further reduce the reduction step temperature and will increase the reduction extent [8].

## 1.1 Objective

The objective of this dissertation is to investigate the feasibility to perform chemical looping processes for syngas production in the CSP system located on the rooftop of the Energy Center building. In this way, it would be possible to store intermittent solar energy in the form of chemical energy through the conversion of $CO_2$ molecules. For this purpose, at first, a geometrical optics model and an interconnected heat transfer model have been developed, using COMSOL Multiphysics, to simulate and predict the temperature evolution of the receiver for the four seasons. Then, to find the best set-up of the system, different chemical looping processes at different temperatures, $CO_2$ concentrations and reducing conditions were investigated at the $CO_2$ Circle Lab in Environment Park using iron oxides powder as the oxygen carrier. An electrically heated tubular furnace is utilized to simulate a real solar thermochemical reactor. After having chosen the best test in terms of process yield and based on the temperature evolution of the Energy Center reactor obtained from the model, it is possible to consider the opportunity to translate this ideal test in real-world condition.

## 1.2 Thesis structure

The thesis is organized into six different chapters to trace, in an orderly way, the path made to reach the objective outlined in the above section. Here is reported a brief description of the main topic analyzed in every single chapter.

1. INTRODUCTION
   Gives a global introduction, contextualizing the general topic. Moreover, the main objective of the thesis is explained to provide a better reading key for all the following chapters.
2. LITERATURE REVIEW
   This chapter is dedicated to a detailed literature review. The itinerary starts with the analysis of carbon capture and sequestration technologies. Then is provided with a comparison between different processes able to convert $CO_2$ starting from solar energy, until you get to thermochemical redox cycles. At this point, different oxygen carriers are presented, highlighting the differences between the two main families: volatile and non-volatile. Finally, different reactors and their classification based on different oxygen carriers involved are investigated.
3. TESTING METHODS
   The main objective of this chapter is to give a detailed overview of laboratory configurations. It is divided into two sections, one for each laboratory examined. As regards the $CO_2$ Circle Lab, is also provided with a description of the procedure applied for filling the reactor used in our tests.
4. CONCENTRATOR-RECEIVER SYSTEM MODELLING
   Here is presented a procedure applied for the analysis of the Energy Center reactor temperature variation over time. The objective is to evaluate the feasibility to perform a chemical looping process, with the relative production of syngas, using a solar concentration system. The evaluation of the operative temperature is also fundamental for the choice of materials to be used for all the accessories of the system. In this context, a geometrical optics model and an interconnected heat transfer model have been developed, using COMSOL Multiphysics, to predict the temperature evolution of the receiver, giving the global radiation data as input.
5. EXPERIMENTAL RESULTS
   This chapter is dedicated to the experimental results obtained from tests performed at the $CO_2$ Circle Lab in Environment Park. These tests are based on the chemical looping process for $CO_2$ conversion using iron oxides powder as the oxygen carrier. The objective is to find the optimal

one for each group of tests in terms of yield, after having studied the response of the process at different oxidation temperatures and $CO_2$ concentrations. Is possible then to consider the opportunity to translate these ideal tests in real-world condition, such as the concentrator-receiver system on the rooftop of the Energy Center.

6. CONCLUSIONS

   The last section compiles the conclusions of this dissertation.

# 2 LITERATURE REVIEW

## 2.1 CCS: Carbon Capture and Storage

Carbon Capture and Storage seems to be a good solution to temporarily reduce the $CO_2$ emissions while fossil fuels are still in use and as long as there is no total transition towards renewable energy.

The first part of the process consists of the capture/separation of the $CO_2$ that, in a second moment, will be stored in suitable bodies. Figure 2 shows three possible routes to be followed [10]:

- *Pre-combustion*;
- *Post-combustion*;
- *Oxy-fuel*.

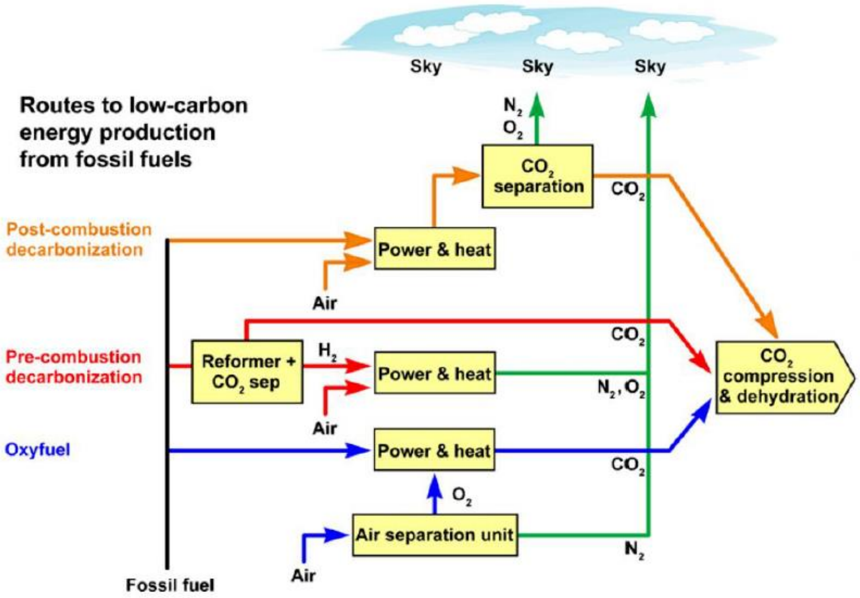

*Figure 2 | Principal routes for carbon capture [10].*

The *post-combustion* CCS consists of the $CO_2$ separation downstream from the flue gases after the combustion [11]. Because of that, this kind of system can be retrofitted to existing fossil fuel power plants at the expense of a reduction of plant efficiency [5]. Moreover, the $CO_2$ separation is not energy efficient because of the ambient pressure at which the flue gases are [10]. Chemical and physical absorptions are the two main paths chosen for the separation process. A liquid solvent is used to scrub $CO_2$. As the same word says, in chemical absorption, the solvent captures the $CO_2$ through chemical reactions into an absorber. This is followed by a stripper column that is used to regenerate the solvent rich in $CO_2$ by heating the stream [12]. This type of process is used when the $CO_2$ content in the flue gas is lower than 15% vol [5]. On the other hand, physical adsorption is preferred when the $CO_2$ content in the flue gas is higher than 15% vol. In this case, the $CO_2$ is captured at the surface of the solvent. Higher the pressure, the higher the absorption ability [13].

For the *pre-combustion* CCS is needed a pre-treatment of the fuel used in the system. If coal is involved, $H_2$ and CO are produced through a gasification process and then the $H_2$ content is increased thanks to a water gas shift (WGS) reaction (2.1). If the fuel is methane, first a steam methane reforming (SMR) (2.2) is performed, followed by the WGS reaction to increasing the $H_2$ content [5].

$$\mathbf{CO + H_2O \leftrightarrow H_2 + CO_2} \tag{2.1}$$

$$\mathbf{CH_4 + H_2O \leftrightarrow 3H_2 + CO} \tag{2.2}$$

Then $CO_2$ and $H_2$ are then separated via chemical or physical absorption.

In the *oxyfuel* CCS, the fuel is burned with pure $O_2$. Consequently, among the products of combustion, there will be only water and carbon dioxide (no $N_2$). In this context, $CO_2$ can be easily separated through water condensation [5]. The biggest energy consumption is not linked to the condensation but to the production of $O_2$ in the air separation unit (ASU): around 0.16-0.25 kWh per kg of $O_2$ are used for the production of a 95% pure $O_2$ stream [14].

After the separation process, $CO_2$ needs to be stored. The most typical options are oil and gas depleted reservoirs, but $CO_2$ can be also stored in oceans [5]. This last case is critical because of the possible acidification of water. For that reason, it is not considered in the near term [15]. $CO_2$ can also be used in enhanced oil recovery considering, however, that the recovery rates are as low as 10% [5].

To summarize, CCS can be considered as a valid solution to temporarily prevent the diffusion of the greenhouse effect while the entire world is still relying on fossil fuels. However, this process has some negative effects, like the reduction of plant efficiency and possible damages linked to the storage sites. As an alternative, $CO_2$ can be seen as a carbon feedstock for the production of new synthetic fuels (such as syngas) and chemicals [16]. In this context, the Carbon Capture and Utilization (CCU) procedure will be discussed in the next section.

## 2.2 CCU: Carbon Capture and Utilization

Instead of storing $CO_2$ in the Earth's crust or deep oceans after the separation process, a different route of carbon cycle may be built to compensate for its emission [2]. In this context, we move from CCS to Carbon Capture and Utilization (CCU) in which $CO_2$ will be re-utilized to obtain useful products. The main advantage compared to CCS methods are the end products that can be used as fuels or raw materials of chemicals [17]. Syngas ($H_2$ and CO) is one of the fuels that can be obtained by exploiting the $CO_2$ captured from the atmosphere. It can be used as a fuel itself or as raw material for chemicals production such as DME, ethanol and methanol. Moreover, through the well-known Fischer-Tropsch (FT) technology, syngas can be used for the production of synthetic liquid fuels [7]. The external heat needed to drive the process can be provided by solar energy. In this way, besides the mitigation of environmental issues, a new route for energy storage will be provided [2]. The fuel produced using solar energy is termed "solar fuel" [5].

The main alternatives for $CO_2$ conversions are:

- *Hydrogenation*;
- *Photo-electro-chemical* process;
- *HT Electrolysis*;
- *Thermochemical* processes [17].

The catalytic *hydrogenation* process consists of the reduction of $CO_2$ into CO by hydrogen or hydrocarbons (typically $CH_4$). When carbon dioxide reacts with $CH_4$, syngas ($H_2$+CO) is produced. The negative aspect of this process consists in the high cost of hydrogen or hydrocarbons [17]. Hydrogenation can also be used to produce fuel and chemicals such as higher alcohols, hydrocarbons, methanol and formic acid [18].

Through the dissociation of water and the consequent production of electrons and protons, the *photo-electrochemical* process converts $CO_2$ using solar energy. The conversion rate is strictly dependent on $CO_2$ solubility [17]. There are several problems linked to the photocatalysts such as low selectivity, high charge recombination and poor solar light utilization [19], [20]. To increase selectivity, a good semiconductor needs to be developed. In the study of Jiang et al. [21], graphite-like carbon nitride (g-$C_3N_4$) has been found as a good photocatalyst for its high stability and low cost. Due to the low surface area and the poor charge separation, there are still some improvements to be performed, like metal or non-metal elements doping [22].

The *HT electrolysis* uses electrical energy, since the reactions are non-spontaneous ($\Delta G>0$), to split $H_2O$ and $CO_2$ molecules into a solid oxide electrolyzer (SOEC) [23]. This is composed of two noble-metal coated electrodes (anode and cathode) with an electrolyte in between, which allows ions transfer. The process is limited by the deactivation of electrodes and by the cost of electricity [17]. Lower the temperatures, lower the efficiency of both the reactions involving $H_2O$ and $CO_2$, as a result of slow kinetic and high internal resistance of cell materials [23]. Among all, the principal negative aspect of the process is the conversion from solar energy into electricity, losing efficiency. On the other hand, the electrolyzer size can be really small, increasing the system functionality.

To overcome the problem of the efficiency reduction linked to the energy conversion we need to move to *thermochemical processes* for syngas production. It is important to highlight that in these cases, as the reverse condition, the system size will be bigger, reducing the system functionality (trade-off).

## 2.3 Thermochemical processes for $CO_2$ conversion

The three conversion methods mentioned above show different negative aspects that can be translated into high process costs. Thermochemical $CO_2$ conversion seems to be the best choice among the others because it is cost-effective [17]. A CSP plant can be used to collect high-temperature solar heat useful to sustain the process.

In this contest two different paths will be analyzed:

- *Thermolysis;*
- *Thermochemical cycles.*

### 2.3.1 Thermolysis

The direct dissociation of $CO_2$, also known as thermolysis, is the simplest way to split the molecule. Extremely high temperatures are needed (above 2500 K) at which gaseous products (CO and $O_2$) must be separated to avoid recombination (quenching process) or resulting in an explosive mixture [24]. In this frame, the realization is really difficult. Traynor et al. [25] have analyzed this process with a prototype in the USA. After having preheated the carbon dioxide to 1900 °C and then heated up to 2400 °C, only 6% of $CO_2$ was converted into CO.

### 2.3.2 Thermochemical cycles: Chemical looping process

Thermochemical cycles overcome the problems linked to the direct dissociation mentioned above, reducing process temperature and by-passing the separation problem through a multiple-step process.

In this case, the maximum-temperature step (the endothermic one) takes place at a temperature lower than that one of the single-step thermochemical process [24]. Nonetheless, a high-temperature source of heat is still needed to feed the endothermic reaction. Concentrated solar power can be used to drive this reaction to produce green energy vectors at the end of the process [4].

Chemical Looping (CL) is the name that can be attributed to the whole thermochemical cycles process. A particular interest is given to the two-step cycle. The basic principle is the splitting of $CO_2$ and $H_2O$, for the production of CO and $H_2$ respectively, by exploiting the transition between the oxidized and reduced form of a metal oxide (MeO) showing multiple oxidation states [24]. Figure 3 shows a scheme of the process.

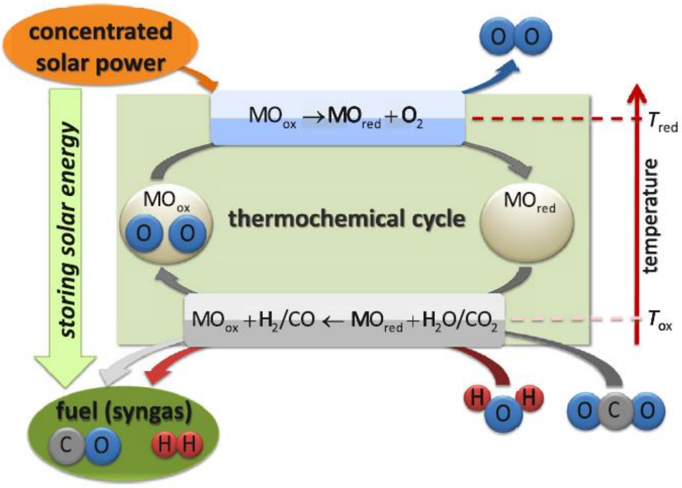

*Figure 3 | Two-step chemical looping process scheme [24].*

In the first high-temperature endothermic step (typically above 1300 °C, depending on the material), the metal oxide is thermally reduced (2.3) thanks to the external energy provided by the CSP system, releasing $O_2$ and assuming a lower-valence state. This step will be called TR that stays for "thermal reduction". An inert gas is used to remove the oxygen and maintain a low oxygen partial pressure in the reduction reaction ambient. In the following step, both water splitting (WS) (2.4) and carbon dioxide splitting (CDS) (2.5) occurs. This second and last step is exothermic and occurs at a lower temperature (around 1000 °C or even less). The MeO reduced in the first step will be re-oxidized thanks to the released oxygen from $CO_2$ and $H_2O$ mixture, returning to a higher-valence state. The $CO_2$ and $H_2O$ splitting will give syngas as a product (CO and $H_2$). $H_2O$ and $CO_2$ can be also sent in two different moments, allowing the separate production of $H_2$ and CO. In a second moment, the two gases can be mixed with a controlled $H_2$/CO ratio [4]. At the end of the cycle the solar fuel is produced, storing on it all the energy potential coming from the sun, and, as the second positive effect, the $CO_2$ is transformed. After the oxidation, the metal oxide can return to the reduction step ready to face another cycle.

$$\mathbf{MeO_{oxidized} \rightarrow\ MeO_{reduced} + \frac{1}{2}O_{2(g)}} \tag{2.3}$$

$$\mathbf{MeO_{reduced} + H_2O_{(g)} \rightarrow\ MeO_{oxidized} + H_{2(g)}} \tag{2.4}$$

$$\mathbf{MeO_{reduced} + CO_{2(g)} \rightarrow\ MeO_{oxidized} + CO_{(g)}} \tag{2.5}$$

The two steps form a redox (reduction/oxidation) cycle of the metal oxide which works as the catalyst of the system.

If the achievable temperature for the reduction step is too low to perform a thermal reduction as the one described above, it is possible to consider the use of reducing gases ($CH_4$, $H_2$) that enhance the reduction of the metal oxide and makes it possible even at lower temperatures (and so reducing the temperature gradient between the two steps of the cycle). The reduction extent will be higher but is important to consider the carbon deposition consequence if the $CH_4$ will be used.

Azharuddin E Farooqui [5] reported this possibility to combine the redox cycle with methane reforming. The reduction reaction of such a modified cycle is written below while the following oxidation step will be identical to 2.4 and 2.5. A complete schematic is then shown in Figure 4.

$$\mathbf{MeO_{oxidized} + CH_{4(g)} \rightarrow MeO_{reduced} + CO_{(g)} + 2H_{2(g)}} \tag{2.6}$$

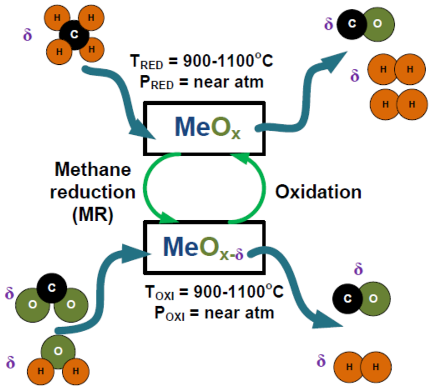

*Figure 4 | Two-step methane-reduction chemical looping process scheme [5].*

In this case, we are no longer talking about TR but assisted reduction. Bio-methane can be used, considering its importance in the renewable energy mix. The positive aspect of that kind of process is the simultaneous production of syngas from both reduction and oxidation steps.

## 2.4 MeO: Oxygen carriers for CL process

There are a lot of different oxygen carriers (OCs) that can be utilized for the redox cycles. The main necessary condition is that they must have at least two states of oxidation, otherwise, CL cannot be performed.

In general, a gas splitting metal oxide should exhibit the following properties [8]:

1. Large redox extent;
2. Adequate thermochemical properties;
3. Fast redox kinetics;
4. High mechanical stability and sintering resistance;
5. Low toxicity and low cost.

The differences between the possible metal oxides are linked to:

- Potential for oxygen storage;

- Reduction and oxidation reactions temperature;
- Phase transformation or not during the redox cycle [5].

In literature, there are numerous studies performed to find the suitable oxygen carrier for the chemical looping splitting cycle [24], [26], [27], [28], [29].

Based on the eventual phase transformation during redox cycles, the oxygen carriers can be divided into two families:

1. *Volatile oxygen carriers*
2. *Non-volatile oxygen carriers*

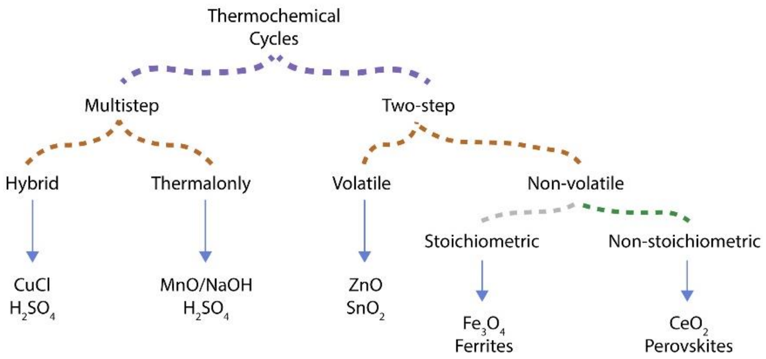

*Figure 5 | Characterization of oxygen carriers [8].*

In Table 1 are reported temperature ranges at which the main oxygen carriers work during a CL cycle. Note that in the case of CdO/Cd the values are not accurate because of the toxicity of the OC and so the difficulty of performing different studies.

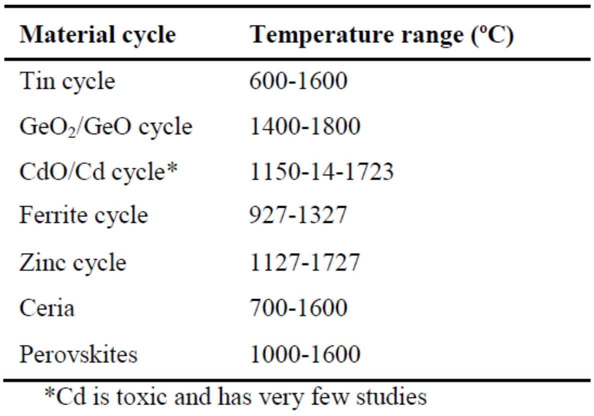

| **Material cycle** | **Temperature range (°C)** |
|---|---|
| Tin cycle | 600-1600 |
| $GeO_2$/GeO cycle | 1400-1800 |
| CdO/Cd cycle* | 1150-14-1723 |
| Ferrite cycle | 927-1327 |
| Zinc cycle | 1127-1727 |
| Ceria | 700-1600 |
| Perovskites | 1000-1600 |

*Cd is toxic and has very few studies

*Table 1 | Temperature ranges for different OCs [5].*

For temperature values largely above the ranges indicated in the table, we go towards the degradation of the material.

### 2.4.1 Volatile oxygen carriers

Volatile oxygen carriers undergo a solid-to-gas phase transition during the reduction step. The metal produced during the TR is usually in a vapour state because of the lower boiling temperature concerning that one of the corresponding metal oxide. Recombination with $O_2$ needs to be avoided with a fast quench. Nonetheless, a certain quantity of $O_2$ recombines with the metal oxide during the quenching process reducing the cycle efficiency [5].

The positive aspect is that the fuel production capacity is high since the reduction reaction of the metal oxide is fully stoichiometric (high oxygen release capacity) [7].

However, the quenching step is considered as the major issue connected with this kind of OCs. Because of that, non-volatile oxygen carriers are more considered in recent times.

The most common volatile oxygen carriers are ZnO/Zn, MgO/Mg, $SnO_2$/SnO and CdO/Cd.

#### 2.4.1.1 ZnO/Zn

The TR of the ZnO/Zn chemical looping cycle occurs at approximately 2300 K using solar process heat. Given that Zn melts at 692 K and has a boiling point of 1180 K, it undergoes a phase change (solid-to-gas) [24].

$$\mathbf{ZnO_{(s)}} \rightarrow \mathbf{Zn_{(g)}} + \frac{\mathbf{1}}{\mathbf{2}}\mathbf{O_{2(g)}} \tag{2.7}$$

Because of that, at the end of this phase, a fast quench is needed. Fractional crystallization in a temperature-gradient tube furnace was used to study the condensation of $Zn_{(g)}$ in the presence of $O_2$ [30]. The dilution ratio of $Zn_{(g)}$ in an inert gas flow was discovered to be an important parameter determining the quenching efficiency together with the surface temperature on which the quench takes place.

An optimized quench apparatus attached to a solar-driven thermogravimeter was synthetically explained by Peter G. Loutzenhiser et al. [9]. Figure 6 reports a schematic of the system where 1, 2 and 3 represent three different temperature zones.

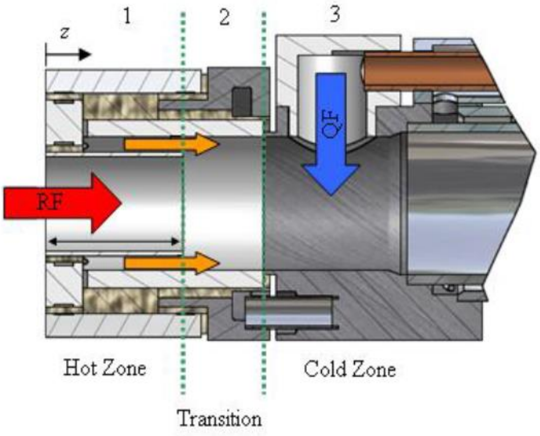

*Figure 6 | Quench apparatus schematic [9].*

Subsequently, takes place the non-solar step. Both $CO_2$ and $H_2O$ react with Zn that will be re-oxidized and will be sent back to the first step ready to face another cycle.

$$\mathbf{Zn_{(s)} + H_2O_{(g)} \rightarrow ZnO_{(s)} + H_{2(g)}} \tag{2.8}$$

$$\mathbf{Zn_{(s)} + CO_{2(g)} \rightarrow ZnO_{(s)} + CO_{(g)}} \tag{2.9}$$

$H_2$ and CO can be produced on demand independently from the solar energy availability since the oxidation step is decoupled from the TR one [9].

Zn is very reactive in the oxidation with $CO_2$ and $H_2O$, producing a high purity $H_2$ and CO [7].

The portion of solar energy that is converted into chemical one by CO and/or $H_2$ production can determine the conversion efficiency of the system. 39% is the value of the efficiency obtained by Galvez et al. that have ignored in their study heat transfer loss, pump work, solar radiation loss, etc. [31].

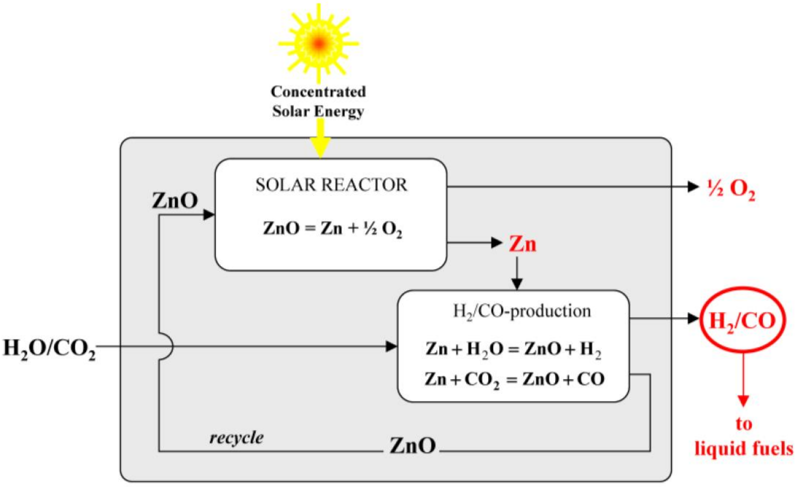

*Figure 7 | Schematic of the two-step solar thermochemical cycle based on ZnO/Zn redox reactions [9].*

Palumbo R et al. [32] have analyzed different aspects of the thermal dissociation of ZnO at the Swiss Federal Institute of Technology/Paul Scherrer Institute (ETH/ PSI) Zurich.

Incentive policies and higher carbon tax are needed for the economic feasibility of the ZnO/Zn cycle with a consequent implementation of the solar $H_2$ plant [9].

#### 2.4.1.2 MgO/Mg

Chuayboon and Abanades [7] talk about the possibility of using solar thermochemical reduction of MgO as a $CO_2$-free way to obtain Mg commodity that is commonly used as a structural material.

$$\mathbf{MgO_{(s)} \rightarrow\ Mg_{(g)} + \frac{1}{2} O_{2(g)}} \qquad 2.10$$

The negative aspect is that this reaction is not practical due to the extremely high dissociation temperature (3600 °C). Carbothermal (2.11) and methano-thermal (2.12) reduction can be considered as valid alternatives for the reduction of MgO since they can occur at lower temperatures.

$$\mathbf{MgO_{(s)} + C \rightarrow\ Mg_{(g)} + CO_{(g)}} \qquad 2.11$$

$$\mathbf{MgO_{(s)} + CH_4 \rightarrow\ Mg_{(g)} + CO_{(g)} + 2H_{2(g)}} \qquad 2.12$$

The only drawback is that the presence of carbon may contaminate MgO.

#### 2.4.1.3 SnO2/SnO

Agrafiotis et al. [24] have written about the $SnO_2$/SnO cycle. In their analysis report that the thermal reduction temperature is around 1873 K. SnO will be in gaseous form under atmospheric pressure due to its lower boiling temperature (1800 K).

$$\mathbf{SnO_{2(s)} \rightarrow\ SnO_{(g)} + \frac{1}{2} O_{2(g)}} \qquad 2.13$$

To suppress the recombination, both quenching devices and reduction of $O_2$ partial pressure can be adopted. Compared with ZnO, $SnO_2$ has a higher dissociation rate in addition to a lower reactivity with $O_2$ in the TR step.

The re-oxidation with $H_2O$ occurs at around 873 K.

$$\mathbf{SnO_{(s)} + H_2O_{(g)} \rightarrow\ SnO_{2(s)} + H_{2(g)}} \qquad 2.14$$

The conversion rate of $H_2O$ to $H_2$ can reach over 90%. In the case of the ZnO/Zn cycle, it was around 55%.

The negative aspect compared to the ZnO cycle is that the oxidation pace is slower [17].

When we are dealing with CDS, if you wanted to reach the same conversion rate as $H_2O$, the temperature needs to be higher.

The simultaneous splitting of $CO_2$ and $H_2O$ seems to be not convenient as a result of the higher reactivity of SnO with water compared to carbon dioxide.

#### 2.4.1.4 CdO/Cd

Always Agrafiotis et al. [24] briefly explain the solar thermochemical cycle involving CdO/Cd.

The thermal reduction/CdO decomposition is shown below:

$$\mathbf{CdO_{(s)} \rightarrow Cd_{(g)} + \frac{1}{2}O_{2(g)}} \tag{2.15}$$

1423 - 1723 K is the temperature range at which the reaction above was demonstrated in a laboratory. The exact value depends on the carrier gas. Even in this case, since we are talking about volatile OC, quenching must be implemented. To close the cycle, the reoxidation of the metal occurs and $H_2$ is produced (2.16).

$$\mathbf{Cd_{(s)} + H_2O_{(g)} \rightarrow CdO_{(s)} + H_{2(g)}} \tag{2.16}$$

None of the decomposition, quenching or hydrolysis has been already demonstrated under real-world conditions.

### 2.4.2 Non-volatile oxygen carriers

Since non-volatile oxides remain in the solid-state during the CL process, only $O_2$ is released from the structure after the TR and the recovery of the obtained solid product is facilitated. The problem of recombination and so the fast quench does not exist. However, there are issues connected to the non-stoichiometric reaction (perovskite and ceria) for which fuel productivity is lower due to the lower $O_2$ release capacity [7]. In this contest, the storage capacity for non-volatile OCs will be reduced from 2 to 5 times concerning that one of the volatile OCs [5].

Due to the preservation of the solid-state, the particle size, the specific surface area and the intra-particle porosity are really important parameters for the oxidation reaction with $H_2O$ and $CO_2$ [24].

#### 2.4.2.1 Iron-oxides

Among all the solid oxygen carriers, an iron-based catalyst is attractive due to the properties of environmentally friendly and low cost. It has to be considered that iron ores are abundant, and mining and production technologies are mature. Moreover, many iron ores can be directly used as OC after simple treatments [33]. They are characterized by high oxygen release capacity but can have sintering issues and a consequent low cyclic stability [7].

The use of porous iron oxide as OC will enhance redox kinetics thanks to the reduced diffusion length and the favoured intra-particle diffusion [34]. As can be seen in Figure 8 [35], the fresh sample structure has already a low porosity with small pores. As the reduction advance (figure is referred to 800 °C reduction with 5% of $H_2$ balanced by $N_2$), we can see a porous structure formation both on the surface and interior of the oxygen carrier. The mean pore volume increases with reduction time and there is a porous particle formation. The reason for the changes in the surface areas and pore volume of the OC samples could be attributed to the oxygen vacancies formation that took place during the reduction process.

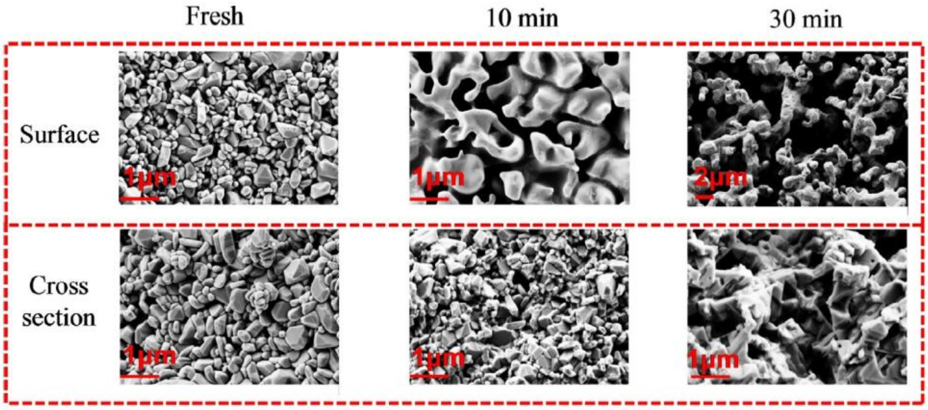

*Figure 8 | Morphology evolution in surface and cross-section for fresh and reduced OC samples under different reduction time at 800 °C with 5% of $H_2$ balanced by $N_2$ [35].*

In the context of iron oxide, it has to be highlighted that the iron can assume different oxidation state:

1. FeO, constituent of the wüstite mineral;
2. $Fe_3O_4$, constituent of the magnetite mineral;
3. $Fe_2O_3$, constituent of the hematite mineral;

respectively the lowest, the intermediate and the highest.

If the OC considered is hematite (highest oxidation state), after the CL reduction it becomes wüstite. At this point, oxidating with $CO_2$ and/or $H_2O$, the iron will assume the intermediate oxidation state ($Fe_3O_4$): the kinetic is slow, is not possible to directly reach $Fe_2O_3$ during CDS or WS [36]. If we want to obtain again $Fe_2O_3$, another oxidation step with pure oxygen or air (where oxygen is readily available) is needed.

The redox reactions of the cycle involving $Fe_3O_4$/FeO are reported below:

$$\mathbf{Fe_3O_{4(s)} \rightarrow\ 3FeO_{(s)} + \frac{1}{2}O_{2(g)}} \tag{2.17}$$

$$\mathbf{3FeO_{(s)} + H_2O_{(g)} \rightarrow\ Fe_3O_{4(s)} + H_{2(g)}} \tag{2.18}$$

$$\mathbf{3FeO_{(s)} + CO_{2(g)} \rightarrow Fe_3O_{4(s)} + CO_{(g)}} \qquad 2.19$$

Nakamura [37] first analyzed the $Fe_3O_4$/FeO cycle. 2500 K was the TR reaction temperature. Since the melting point of FeO is 1650 K, at the output of the reduction step it is in liquid form. After the TR, $H_2$ is produced (together with $Fe_3O_{4(s)}$) from the WS step.

Abanades et al. [38] converted $CO_2$ using a CSP system with the $Fe_3O_4$/FeO cycle. The reduction temperature tested was 2000-2500 °C (higher than the melting point of $Fe_3O_4$). Changing the oxidation temperature will change the conversion rate of $CO_2$ which resulting equal to 95% at 1100 °C and 93% at 800 °C.

According to the research group of PROMES [39], when sending $H_2O/CO_2$ mixture in the oxidation step, the $H_2$ production is favoured (80% of FeO is oxidized thanks to WS) concerning CO production. In this context, it may be better to consider sending in different moments $H_2O$ and $CO_2$, to separately obtain $H_2$ and CO.

The possibility to improve the stability and reactivity of iron oxides by doping them with spinel structure was discussed by Chuayboon and Abanades [7] referring to some literature information. The alternative of using $Fe_2O_3$/YSZ for WS and CDS is reported by Agrafiotis et al. [24] which give information about a study of the SNL group. Multiple cycles have been performed to demonstrate both WS and CDS. The dissolution with YSZ seems to make the material more “redox-active” with a higher oxygen yield. Moreover, the solubility limit of Fe in the 8% YSZ, limits the maximum amount of syngas produced.

It is possible to reduce the temperature of the reduction steps by performing an assisted reduction with $H_2$ or with $CH_4$. These are two reducing gases that will accelerate the reaction, also increasing the reduction extent and so increasing the production in the following oxidation step.

Azharuddin E Farooqui et al. [36] analyze a CL process with a mixture of 5% $H_2$ and 95% Ar for the reduction step. The following CO production was studied changing the $CO_2$ concentration in the oxidation step from 20% to 40% in the temperature range of 700 – 1000 °C. The CO production is given in µmol/g/s and the graphs for the different oxidation temperatures are reported in Figure 9. From the obtained results is noticeable that the CO production is faster at the beginning (higher oxygen vacancies), going down in time. The material shows a gradual deactivation at 1000°C with a decreasing CO yield, compared with the increasing of the same quantity going from 700 °C to 900 °C. The formation of $Fe_3C$ at high temperatures can be the explanation for the phenomena.

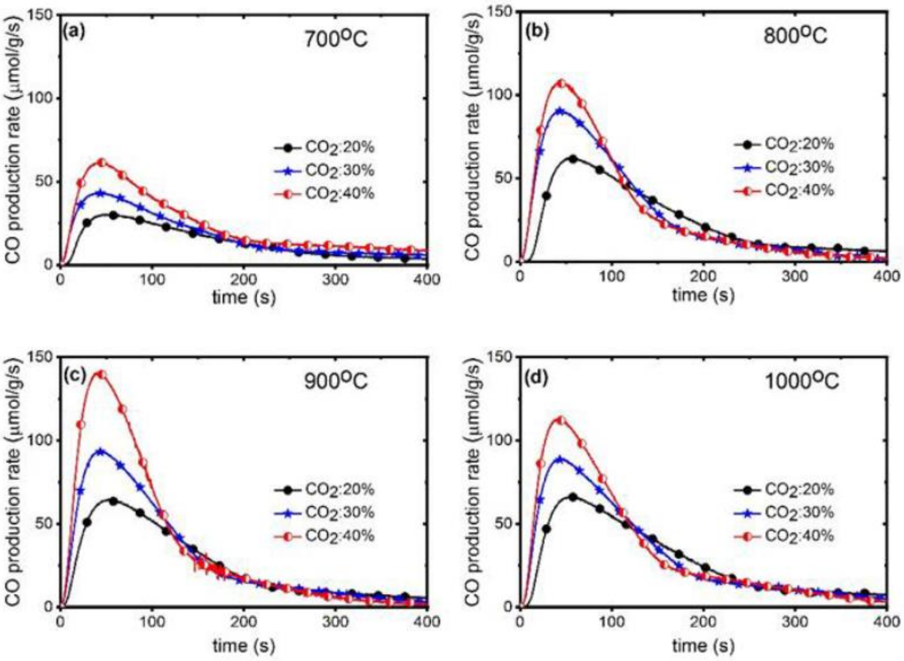

*Figure 9 | CO production rate [36].*

Lu et al. [40] studied a chemical looping reforming of methane (CLRM) and so using methane as reducing fuel and steam as an oxidizing gas, putting 300 mg of iron oxides powder in the reactor. The mixture for the reduction reaction is made of 10% $CH_4$ and 90% $N_2$ and it is sent at 1223 K. The oxidation step is then performed at 1123 K. The experiment was composed of six cycles and the results are shown for each of them. During the reduction reaction, the syngas is produced together with a very little amount of $CO_2$. At the beginning of the reaction, products concentration is negligible, but increasing in time. Such behaviour can be attributed to the dense structure of magnetite. Moreover, the intensity of $H_2$ is almost twice the one of CO. In the end, the syngas yield results equal to 10.29 mmol/g (95.11% purity). $H_2$ is also produced at the oxidation step with a yield of 4.94 mmol/g (purity 96.22%).

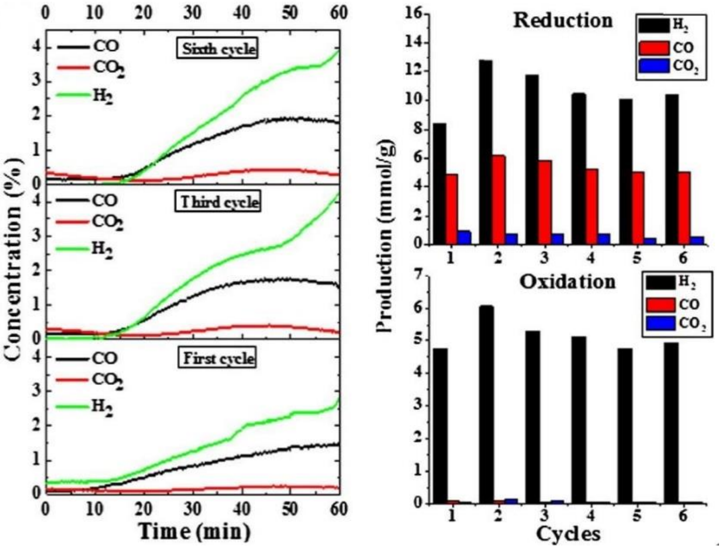

*Figure 10 |Results of the experimental analysis [40].*

Another study focused on the reduction with methane is that one of Monazam et al. [41] which, however, analyzed chemical looping combustion (CLC). The reaction of $CH_4$ with iron oxide was performed at different $CH_4$ concentrations (15 – 35%) in $N_2$, in the temperature range of 700-820 °C for 10 cycles. At a fixed $CH_4$ percentage, increasing temperature will increase the degree of reduction, as can be seen in Figure 11.

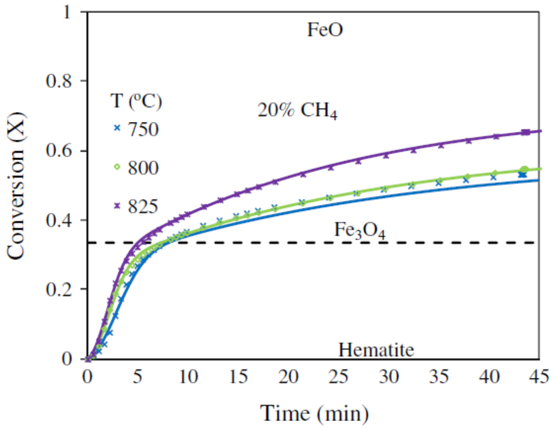

*Figure 11 | Effect of reaction temperature on the conversion of hematite using 20% $CH_4$ [41].*

As a negative effect, the temperature increase will also increase the carbon deposition (which increase also with $CH_4$ concentrations). In this context, a trade-off for choosing the temperature values is needed.

Even Zhu e al. [42] analyzed a process (CLDH, chemical looping dry reforming with hydrogen production) using methane as a reducing agent. The oxygen carrier used was $Fe_2O_3/Al_2O_3$ and the process was performed in a fluidized-bed reactor at 900 °C and 1.01 bar. Different tests were performed using different $CH_4/CO_2$ ratios (i.e. 1, 2, 3) in the dry reforming step. As a result, the $H_2/CO$ ratio increased as well, changing from 1.04 to 1.44 and finally to 1.69 respectively. At the same time, also the carbon deposition increased while the CO selectivity reduced. When the feed ratio of $CH_4/CO_2$ was 1 and the reduction extent of iron was 33%, the $CH_4$ conversion reached 98.32% while the syngas yield (syngas output/$CH_4$ in input) was 3.84.

#### 2.4.2.2 Perovskites

Bayon et al. [8] give general information on the basic principles of perovskite materials.

Perovskites are all the materials with the same crystal structure of $CaTiO_3$. Calcium titanate was first discovered in 1839. The structure contains two cations and an anion. If the perovskite is a metal oxide, the oxygen represents the anion, and the formula is like $ABO_3$. A is larger than B and the oxygen is collocated in the edge centres. Figure 12 shows three different possible structures.

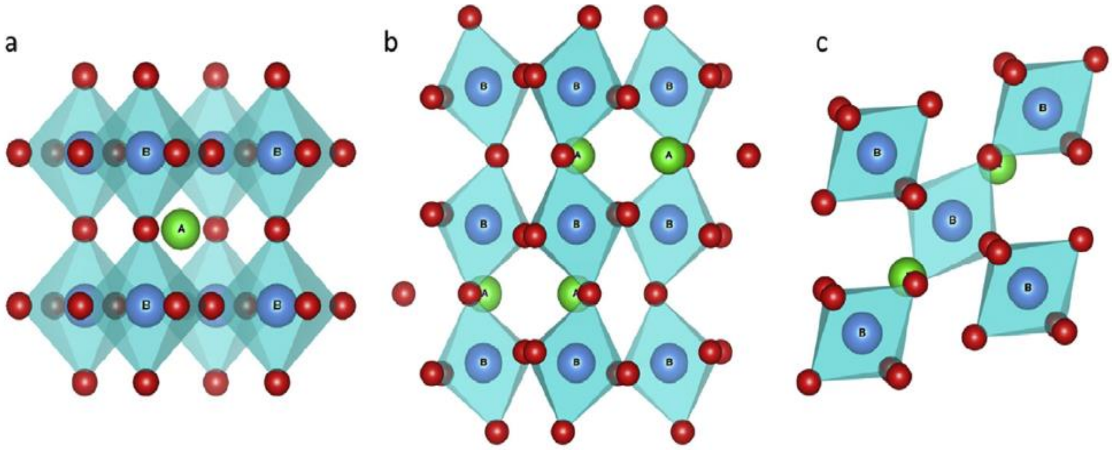

*Figure 12 | Perovskite structures with $ABO_3$ formula: (a) cubic; (b) orthorhombic; (c) rhombohedral [8].*

A and B sites can be occupied by more than one element, creating a doped perovskite or double perovskite.

In the case of a solar thermochemical cycle, perovskites can be used as catalysts, becoming the protagonists of the redox reactions. These reactions are reported below, where δ indicates the extent of the reduction:

$$\mathbf{ABO_3 \rightarrow ABO_{3-\delta} + \frac{\delta}{2} O_{2(g)}} \tag{2.20}$$

$$\mathbf{ABO_{3-\delta} + \delta H_2O_{(g)} \rightarrow ABO_3 + \delta H_{2(g)}} \tag{2.21}$$

$$\mathbf{ABO_{3-\delta} + \delta CO_{2(g)} \rightarrow ABO_3 + \delta CO_{(g)}} \tag{2.22}$$

The reduction is non-stoichiometric (oxygen vacancies formation), so the energy needed to produce the oxygen vacancies is a critical parameter for the quantification of syngas produced.

As Haeussler et al. [4] wrote in their article, many studies have been performed on Lanthanum-manganite perovskites doped with strontium (A-site substitution). The presence of $Sr^{2+}$ increases the reduction extent with an optimum stoichiometry in the range 0.3 - 0.5. In addition, the presence of $Mg^{2+}$ in the B-site will increase thermal stability and reduce the sintering problem. Generally, $La_{0.5}Sr_{0.5}Mn_{0.9}Mg_{0.1}O_3$ (LSMMg) is considered a good OC for the solar thermochemical cycle due to its high fuel production.

Agrafiotis et al. [24] give information about the two following studies.

The group of ETH/PSI [43] have experimentally studied a CL process using the Lanthanum-Strontium-Manganates ($La_{1-x}Sr_xMnO_{3-\delta}$) as OC. The $O_2$ yield seems to be higher than that one obtained with ceria during the TR performed at 1273 K. On the other hand, at 1073, 1173 and 1273 K the perovskites showed an incomplete re-oxidation from $CO_2$.

Lanthanum-Strontium-Aluminates ($La_{1-x}Sr_xMn_yAl_{1-y}O_{3-\delta}$) have been studied from SNL [44]. It exhibits a good multi-cyclic capability during different TR reactions at 1623 K and different WS and CDS reactions at 1273 K, reporting a higher reduction extent than ceria.

#### 2.4.2.3 Ceria

Ceria has a huge variety of good characteristics which makes this oxygen carrier a perfect candidate for the CL process. Chuayboon and Abanades [7] have listed a series of properties that are reported below:

- Reproducible oxygen storage and release capacity;
- Rapid oxygen exchange rates;
- Stability during multiple thermochemical cycles;
- Fast kinetics.

It is possible to analyze two different kinds of reduction reactions when we talk about ceria.

The first one is based on the stoichiometry of the compound under investigation. In this case, the reaction looks like this:

$$\mathbf{2CeO_{2(s)} \rightarrow\ Ce_2O_{3(s)} + \frac{1}{2}O_{2(g)}} \qquad 2.23$$

Thanks to a solar reactor, at temperatures higher than 2220 K and pressure of 100 - 200 mbar, $CeO_2$ is converted into $Ce_2O_3$ [24]. In this case, ceria will be found in a molten state.

In addition, a different cycle can be proposed, based on the non-stoichiometry of $CeO_2$, not involving melting due to lower temperatures. In this context, the rate of the extent of the reaction (δ) must be introduced. Its value can vary from 0 to 0.5 ($0 <\delta< 0.5$) [45]. The reduction reaction is written below:

$$\mathbf{CeO_{2(s)} \rightarrow\ CeO_{2-\delta(s)} + \frac{\delta}{2}O_{2(g)}} \qquad 2.24$$

After both types of thermal reduction, follow WS (2.25) and CDS (2.26) reactions, as for all the other OCs already seen:

$$\mathbf{CeO_{2-\delta(s)} + \delta H_2O_{(g)} \rightarrow\ CeO_{2(s)} + \delta H_{2(g)}} \qquad 2.25$$

$$\mathbf{CeO_{2-\delta(s)} + \delta CO_{2(g)} \rightarrow\ CeO_{2(s)} + \delta CO_{(g)}} \qquad 2.26$$

The activation energy obtained during CDS seems to be higher than that one of the WS step [46].

Alonso et al. [45] have investigated different non-volatile oxygen carriers collocated in a packed bed reactor. In the case of ceria (as for the other OCs under investigation) the maximum $O_2$ production occurs right after the radiation started. For the evaluation of the sample temperature, three different thermocouples were located at different depths. They have revealed a ΔT higher than 500 °C in a very small length. This is a synonym for low thermal conductivity. Because of that, the evaluation of the temperature in every sample point cannot be provided without uncertainty.

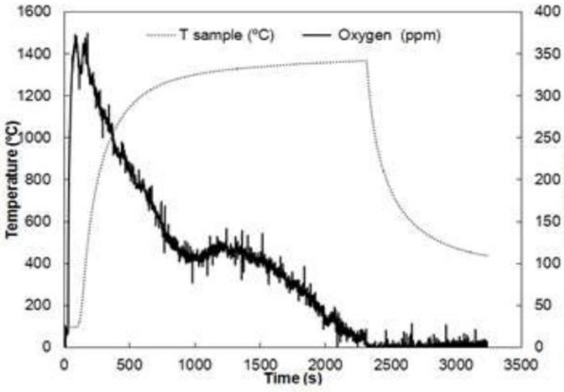

*Figure 13 | Oxygen evolution and sample temperature for the TR of ceria [45].*

Moreover, only a portion of the sample is reduced, corresponding to that one directly irradiated by the higher flux. Some modifications have been performed to increase the amount of surface exposed to the radiation but with poor results.

"Ceria ($CeO_2$) is one of the most efficient oxygen carriers with excellent oxygen ion mobility and redox kinetics. It shows high and stable fuel production rates via a nonstoichiometric oxygen exchange process". This is what Riaz et al. [47] say in their research article.

Nevertheless, in addition to good properties, the ceria-based cycle has high thermal stability loss and low solar-to-fuel efficiency. In this contest, doping cerium oxide-based materials is the main route to be adopted to improve their characteristics [48]. As dopant concentration increases, the reaction of ceria with $CO_2$ and $H_2O$ becomes more efficient (above 1200 K) [24].

Portarapillo et al. [48] have analyzed the partial substitution of Ce with Zr. The oxygen diffusion increases and it helps the splitting properties of $CeO_2$. Through the analysis was found that for the $CeO_2$-$ZrO_2$ system, a Ce/Zr molar ratio equal to 3 seems to be the best compromise for the highest $H_2$ production. Both co-precipitation and hydrothermal synthesis are used for the preparation of $Ce_{0.75}Zr_{0.25}O_2$. A thermogravimetric analysis (TGA) is used to study the activity of the material for CDS and WS. In conclusion, the $Ce_{0.75}Zr_{0.25}O_2$ prepared with the hydrothermal synthesis shows higher redox performance and stability, with higher syngas production.

Even Agrafiotis et al. [24] have found that the addition of Zr in ceria structure "improves the reduction yield and reduces sublimation of the solid-oxide solution", even if a reduction of the cycling performances is confirmed. In addition to Zr, also the YSZ introduction, among all the cationic elements $M^{y+}$ proved, increases the oxygen ions mobility in the TR step.

Always in the doping contest, Riaz et al. [47] proposed a vanadia-ceria multiphase metal oxide system. The performances of the system were analyzed for a sample with $\frac{\mathrm{V}}{\mathrm{Ce}}$ = 25%. Different concentrations of the single elements in the vanadia-ceria system have not been studied. Pure $CeO_2$ and pure $V_2O_5$ are far from the structural stability reached with the doped system. Moreover, mixing $CeO_2$ with $CeVO_4$ allows for obtaining higher syngas yields.

The reduction temperatures needed for a useful reduction extent in the case of ceria systems are high. To overcome this problem the perovskites materials have been introduced because they show "high oxygen exchange capacity at a lower temperature than ceria" as Haeussler et al. [4] wrote. In this frame, dual-phase composites of LSMMg-$CeO_2$ (reticulated foam) have been proposed.

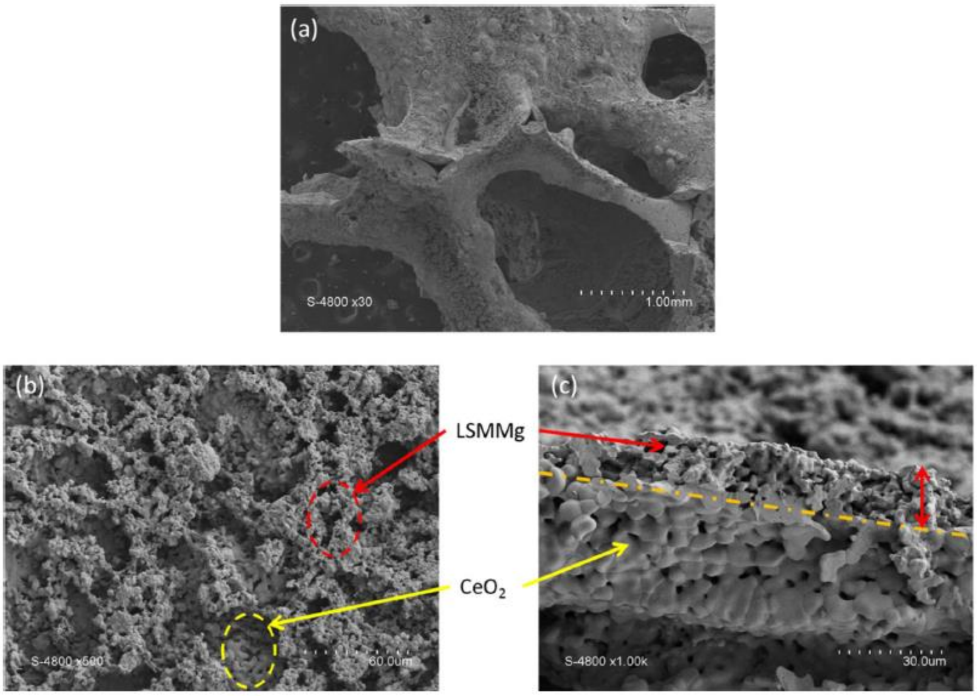

*Figure 14 | Micrographs of LSMMg-coated $CeO_2$ foam: (a) general view, (b) surface view and (c) cross-section view [4].*

The reduction extent was enhanced, while the oxidation yield seems to be lower than that one of the uncoated foams. This last reduction maybe is due to the diffusional barrier effect of the coating. However, a general increase in the performance is obtained with a higher fuel-producing yield despite the fuel production rate remains low.

## 2.5 Solar concentration systems

As Agrafiotis et al. [24] explain, after having chosen the OC for the redox system, what remains to be done is the coupling of the system with the solar energy. A concentrated solar power (CSP) system is used to concentrate the solar energy towards a receiver through collectors/mirrors (from a large area of sunlight to a small one). Nowadays the CSP system is already used for electricity production: after having concentrated the solar energy in a focal point (medium-high temperature heat), the heat is transferred to a heat transfer fluid (HTF). This fluid will drive a conventional power cycle, transferring heat to water which undergoes a phase-change: it evaporates and superheats running a steam turbine, producing electricity. For the solar thermochemical process, the configuration of the CSP system is the same as that one used for electricity production. The main relevant difference is that this time the concentrated solar energy is used to heat a reactor where CL reactions occur.

The main CSP systems are:

- *Parabolic Trough (PT) collectors;*
- *Linear Fresnel (LF) reflectors;*
- *Dish-Engine (DE) systems;*
- *Central Receivers (CR);*

A brief explanation of these systems is reported from Chuayboon and Abanades [7].

As can be easily thought, PT collectors are characterized by a parabolic-shaped mirror. The receiver is a tubular one (linear concentration) and, because of that, the concentration ratio is not high. With this configuration, the temperature of the HTF can reach 550 °C.

The LF system has still a linear receiver but this time the collectors are flat. Moreover, there are secondary reflectors to improve the quantity of solar energy absorbed.

If we need a higher concentration ratio and so higher temperature achievable, we have to move to point focusing systems, as DE systems and CR.

In the first case, the concentrator is a parabolic dish and the punctual receiver is positioned on its focal point. In this case temperatures above 1000 °C can be reached. The limiting aspect of this technology is the size of the dish that defines the amount of solar thermal energy to the receiver.

The last CSP system to be analyzed is the solar tower system (or also central receivers, CR). The receiver is located on the top of a tall tower. A heliostat field is used to focus solar energy on the receiver. This kind of solar collection system is more expensive compared to the other analyzed so far: each heliostat (mirror) follows the sun independently. The concentration ratio is high and allows to reach temperatures in the range of 800 – 1000 °C.

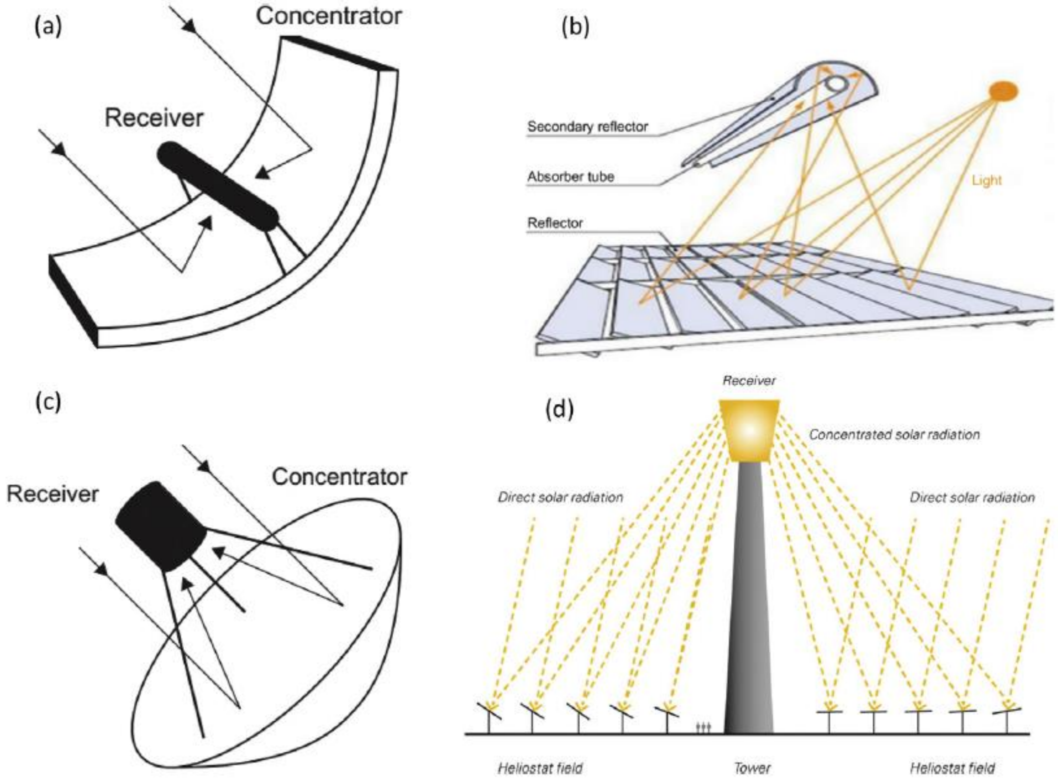

*Figure 15 | (a) Parabolic Trough collectors, (b) Linear Fresnel reflectors, (c) Dish-Engine systems, (d) Central Receivers [7].*

The beam-down is a variant of the CR. It includes a secondary hyperbolic reflector located on the top of the tower (where, in the classic CR, there is the receiver) [24]. This reflector aims to direct the sunlight to the receiver which this time will be located at the ground level. A schematic of this system can be seen in Figure 16:

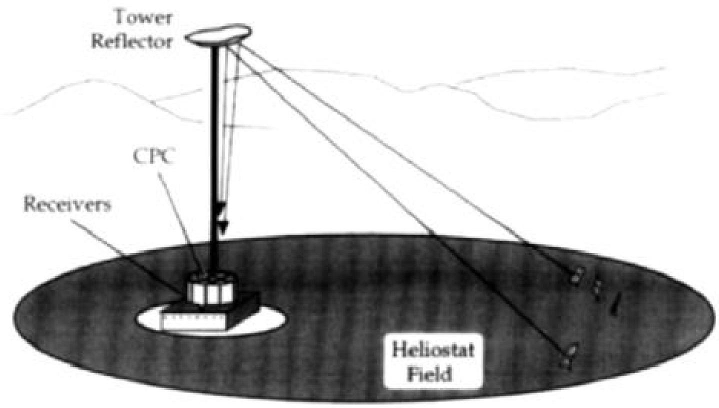

*Figure 16 | Beam-down solar tower configuration [24].*

## 2.6 Reactors for solar thermochemical process

Agrafiotis et al. [24] reported a detailed description of different reactors types, dividing them into classes according to their properties. In this section, we are going to see the main contents of their analysis.

The reactors are the core elements for the redox chemical reactions. The optimal design of a solar reactor is one of the most important parameters to be considered for improved process efficiency.

There are lots of possible classifications for solar reactors based on different characteristics, but our analysis will be concentrated on three main parameters:

- Directly/indirectly-irradiated reactors;
- Structured/non-structured reactors;
- Volatile and non-volatile oxygen carriers.

In the directly-irradiated receivers (DIRs), the chemical reactants (metal oxides) are directly exposed to the sunlight. The positive aspect is the high heat transferred to the site of reaction. On the other hand, we must consider the need for a transparent window that is considered as a critical component [7]. Moreover, the catalyst particles could melt and adhere to the optical components breaking them [49]. In this case, all the volume of the absorber is involved and because of that, this kind of receivers are also known as “volumetric” ones.

Considering the indirectly-irradiated receivers (IIRs), the problem of the transparent window is overcome with the introduction of an opaque absorbing wall. What is directly exposed to the concentrated solar energy is an absorbing surface that uses an HTF to conducts heat through its wall. In this case, the operation of the reactor could be more flexible and the manufacture of the receivers could be simplified [49].

The principle of the black body must be respected for all different types of receivers. In this framework cavities, black-painted tube panels or volumetric porous absorbers are used to approach their capability to capture the incident radiation. External and cavity receivers are the two main geometrical configurations used. The cavity receiver simulates a black body thanks to multiple reflections. The aperture of the cavity must be large enough to allow the inlet of a sufficient amount of solar energy but at the same time not too large to avoid, or at least reduce, losses linked to re-radiation.

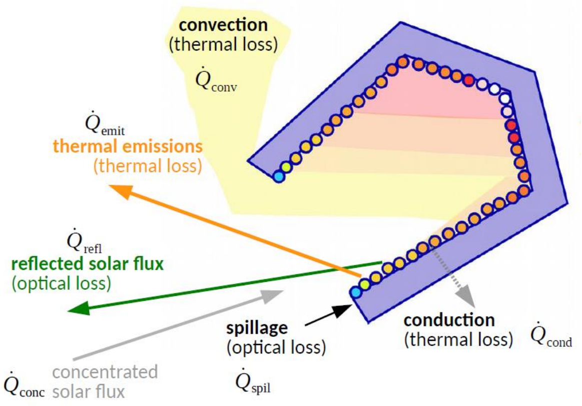

*Figure 17 | Losses associated with cavity receiver [50].*

Analyzing the second classification, the difference between structured and non-structured receivers is based on the disposition of catalyst particles. In the first case, they are arranged in space while in the second they are randomly distributed. Honey-comb, foam and membrane catalytic reactors belong to the first category while packed and fluidized catalytic beds to the second.

Based on the redox chemistry, another distinction can be applied to reactors used for volatile and non-volatile OCs. It is important to highlight that in the case of volatile oxygen carriers, as we have seen in the dedicated section, there is the problem of possible recombination between oxygen and the gaseous form of the reduced metal oxide and so a special quenching is needed to avoid it. This problem avoids the direct combination of the reduction and oxidation steps, so two different reactors are needed. In this contest the two reactors can operate at different times, being not dependent on one from the other: TR occurs during the day when there is the sun while syngas can be produced during the night.

In the table below Agrafiotis et al. [24] reported a detailed subdivision of the reactors for the solar thermochemical process. The same subdivision is maintained in the following sections which have the same main reference.

| **Heat transfer concept** | **Redox cycle** | | | | | | | |
|---|---|---|---|---|---|---|---|---|
| | **Volatile cycles (only TR cycle step)** | | | | **Non-volatile cycles (both cycle steps)** | | | |
| | **Reactor concept** | | | | | | | |
| | **Non-structured reactors** | | **Structured reactors** | | **Non-structured reactors** | | **Structured reactors** | |
| | **Movement** | | | | | | | |
| | **Non-moving particles** | **Moving particles** | **Non-moving structures** | **Moving structures** | **Non-moving particles** | **Moving particles** | **Non-moving structures** | **Moving structures** |
| **Directly-irradiated** | | Rotating cavities<br>Entrained beds | | Moving fronts | Packed beds | Spouted beds<br>Moving beds | Honeycombs<br>Foams | Rotary cylinders<br>Rotating fins |
| **Indirectly-irradiated** | | Aerosols | Sintered plates | | Packed beds | | | |

*Table 2 | Reactors classification considering the solar thermochemical process [24].*

## 2.6.1 Volatile cycles

### 2.6.1.1 Directly-irradiated reactors

#### *2.6.1.1.1 Solar rotary reactor*

This reactor belongs to the non-structured category. In Figure 18 and Figure 19 are reported two different schematics, 3D and 2D respectively, of the rotating cavity reactor proposed by Louzenhiser et al. [9]. Thanks to a screw feeder, ZnO particles enter the system continuously and are maintained against the wall through the centrifugal force creating a packed-bed layer. The particles are directly exposed to the sunlight. Increasing the tube diameter seems to reduce the overall temperatures with consequent slower kinetics and lower ZnO reduction.

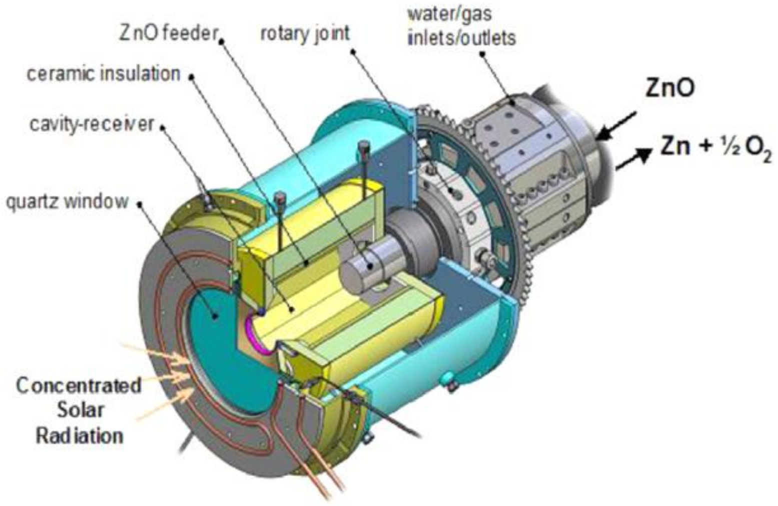

*Figure 18 | Solar rotary reactor 3D schematic [9].*

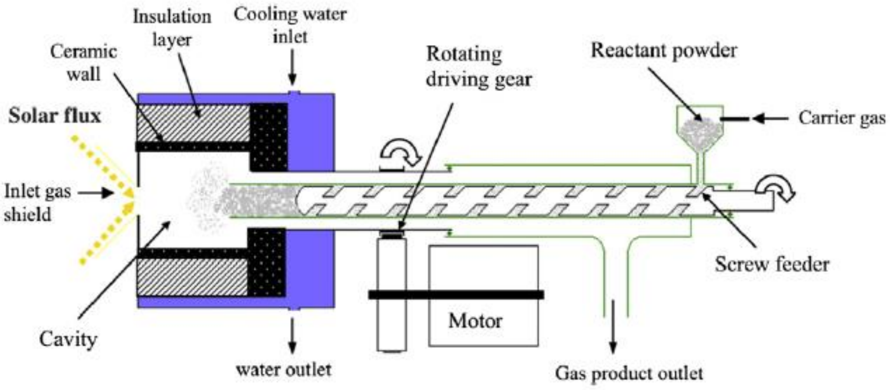

*Figure 19 | Solar rotary reactor 2D schematic [7].*

Agrafiotis et al. [24] reported the achievement of a dissociation yield up to 87% in the same reactor for the ZnO TR at reduced pressure applied by a vacuum pump.

### 2.6.1.1.2 *Entrained-bed, gravity-fed reactor*

Even in this case, we are talking about a non-structured reactor but with the difference to be a static one (no moving parts). The ETH/PSI group in collaboration with the University of Delaware introduced this reactor concept. Since ZnO needs high temperatures for the dissociation, the cavity model is still used.

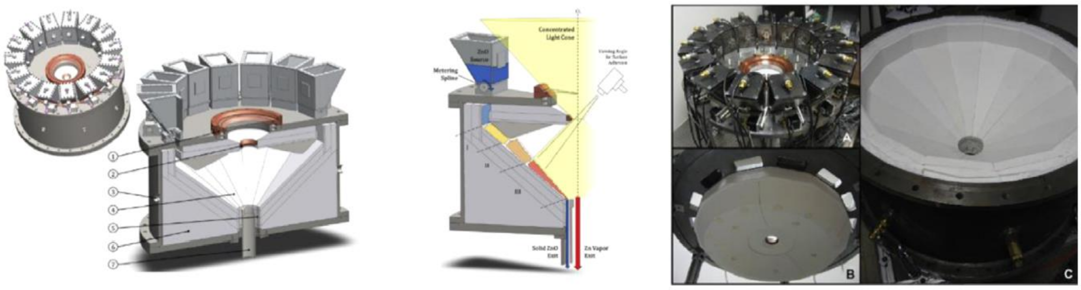

*Figure 20 | Entrained-bed reactor schematic [24].*

A series of fifteen vibrating hoppers, collocated in the upper circular perimeter of the reactor, allow the feeding of the ZnO powders together with the gravity force, without which the powders will not fall into the reactor.

Precisely because is a gravity-fed reactor, it must be collocated in a vertical direction and so it must be coupled with a beam-down configuration.

### 2.6.1.1.3 *Moving front reactor*

Now we move to a structured reactor. This kind of configuration was introduced by the group of PROMES to overcome problems related to cavity rotation. Both $SnO_2$/SnO and ZnO/Zn can be used. To better understand the structure, it is illustrated in Figure 21.

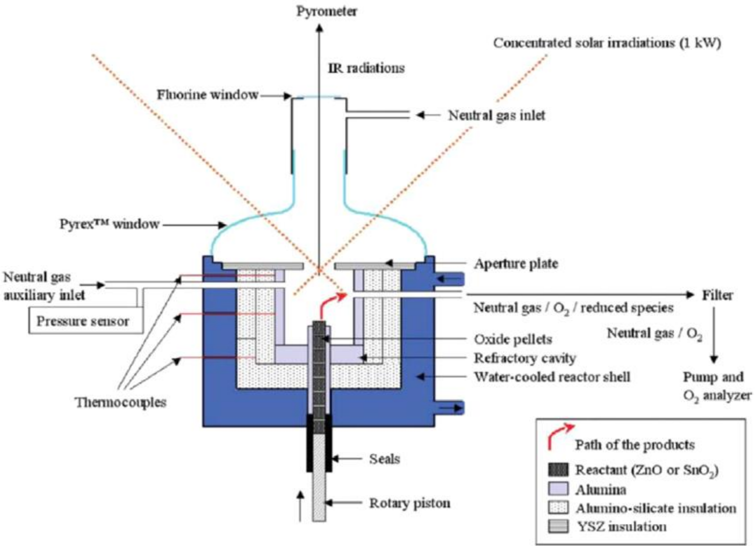

*Figure 21 | Moving front reactor schematic [24].*

It is still a vertical-cavity reactor, but this time the reactant (metal oxide) is collocated into 8 mm-diameter pellets (structured reactor).

1900 K was found to be the perfect temperature at which ZnO and $SnO_2$ dissociations happen successfully. Moreover, at this temperature, the cavity material did not undergo significant degradation even after repeated solar tests.

### 2.6.1.2 Indirectly-irradiated reactors

#### *2.6.1.2.1 Aerosol reactor*

The aerosol reactor consists of "a reactor where the solid reactant is in the form of very fine particles suspended in a gaseous stream" [24]. This reactor has been introduced by the research group of the University in Colorado. The wall of the reactor is made of graphite, which can reach very high temperatures. The need for a cavity window is eliminated by the fact that the fine particles can be easily "indirectly" heated by the radiative heat flux coming from the graphite wall. The reactor is shown in Figure 22.

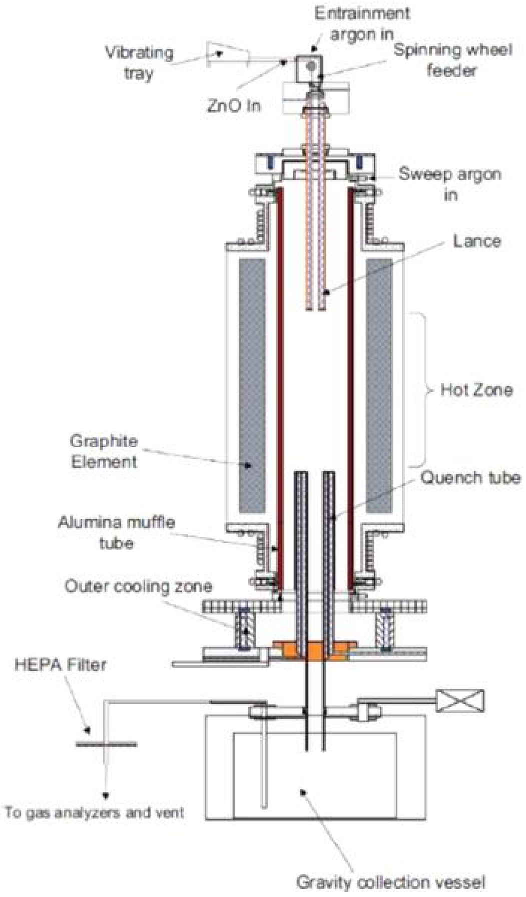

*Figure 22 | Aerosol reactor schematic [24].*

At around 1900-1973 K and with the maximum residence time of around 1.8 s is obtained the highest ZnO reduction.

#### *2.6.1.2.2 Sintered plates reactor*

The ETH/PSI have collaborated on the test performed on such a reactor. Sintered reactant plates are placed inside the absorber tube instead of powders. Since the reactor is indirectly-irradiated, the heating rate is slow (around 40 K/min) compared with the directly-irradiated ones, where the direct exposure of the reactants to the solar radiation allows to reach a heating rate above 1000 K/s.

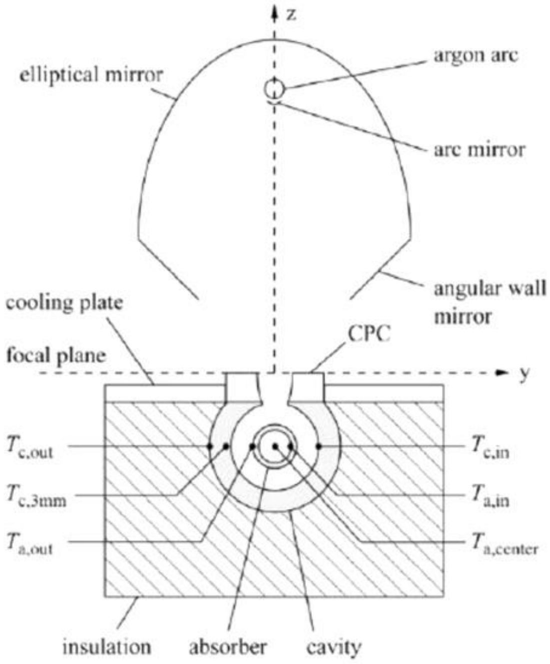

*Figure 23 | Sintered plates reactor schematic [24].*

## 2.6.2 Non-volatile cycles

In the case of non-volatile cycles, one single reactor used for both reduction and oxidation steps is sufficient, since there is not the problem of fast quench linked to the phase-change of the reactant. In this way, there is not any solid transportation.

The design must consider the fact that the cycle is composed of two different steps with different temperature levels and heat demands. In this context, the solar flux is diverted periodically to satisfy the different requirements of the subsequent steps.

### 2.6.2.1 Directly-irradiated reactors

#### *2.6.2.1.1 Packed bed reactor*

The first test was performed in a solar furnace of PSI. In the focus of the same furnace is placed a quartz tube of 2 cm diameter (the packed bed reactor itself). Behind it, a secondary concentrator helps to distribute uniformly the radiation to the tube. In this specific test have been used $Ni_{0.5}Mn_{0.5}Fe_2O_4$ powders as reactants together with $Al_2O_3$ grains.

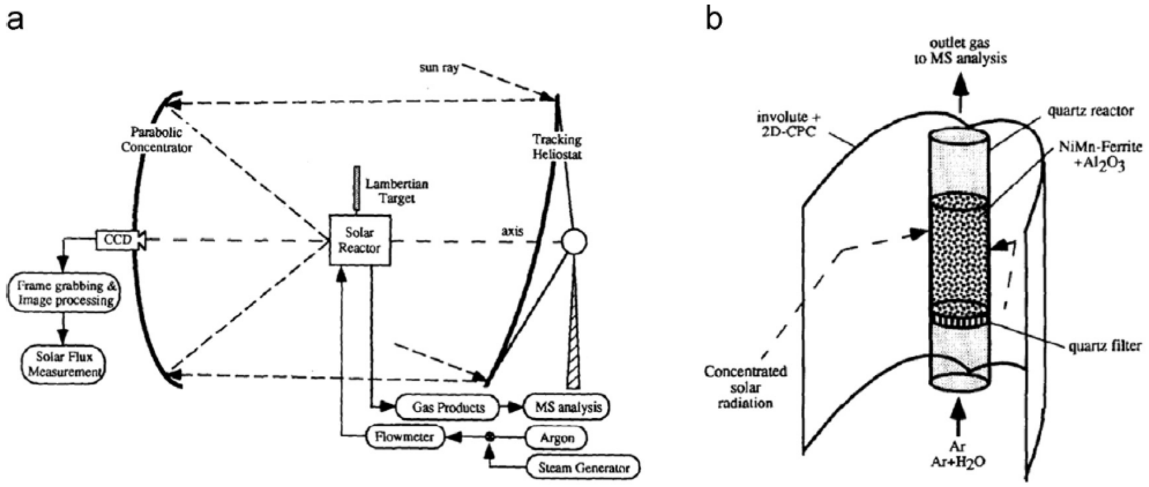

*Figure 24 | (a) Sketch of the experiment in a solar furnace, (b) Packed bed reactor schematic [24].*

The packed bed reactor has a high extent of reaction thanks to long residence time and the large reactant area exposed to sunlight. On the other side, it shows problems connected to temperature gradient [7].

Another type of packed bed has been tested by Alonso et al. [45] with $Mn_2O_3$, $Mn_3O_4$ and $CeO_2$.

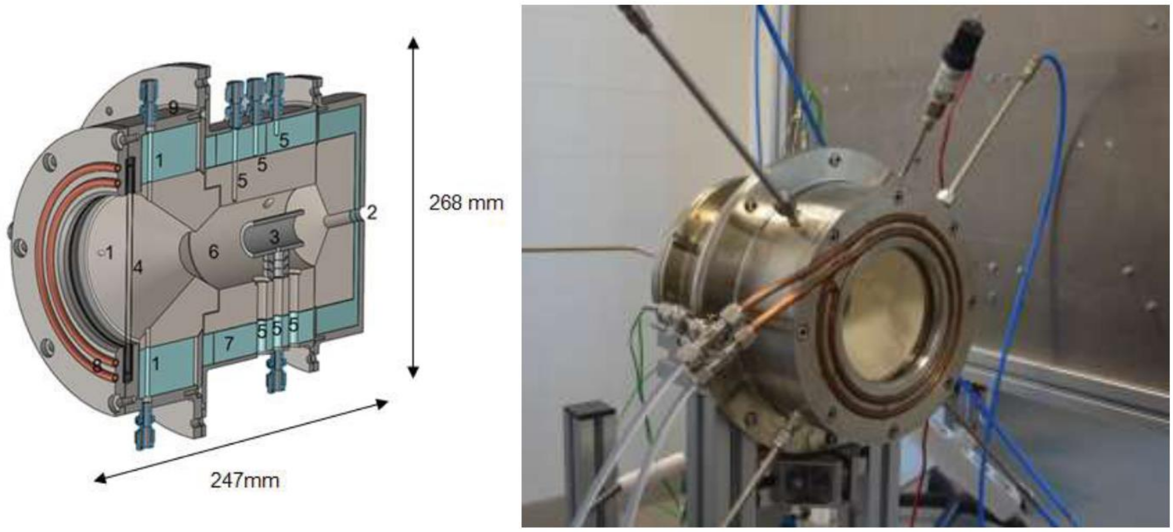

*Figure 25 | Cross-section and photograph of the packed-bed reactor [45].*

This reactor has an alumina cavity surrounded by an insulation layer. Since it is directly-irradiated, a transparent window cooled by water is needed. The aperture is around 30 mm in diameter. The OC samples are in the middle. To evaluate constantly the temperature in the reactor, K-type thermocouples are used.

#### 2.6.2.1.2 *Spouted (fluidized) bed reactor*

A Japanese university group largely analyzes the internally circulating spouted bed reactor (also known as a fluidized bed) coupled with a beam-down solar concentrator configuration (Figure 26). The solar radiation enters through a transparent window located on the top of the reactor. At this point, the OC (in form of particles) coming from the bottom is heated up and then returns down imposing a real circulation. The realization of the two steps of the CL process in a unique reactor is possible thanks to the alternation of the feed gas: $N_2$ for the reducing step and $CO_2$/steam for the re-oxidation step.

$NiFe_2O_4$ and supported $NiFe_2O_4/ZrO_2$ are reactants used during tests for the thermal reduction step, where the sunlight was simulated by Xe-beam radiation. As a result, the temperature reached in the draft tube region was 1773-1873 K while in the annulus region it is around 1373-1523 K.

Among the negative aspects of the fluidized bed reactor, there are attrition and abrasion as well as the particle size limitation [7].

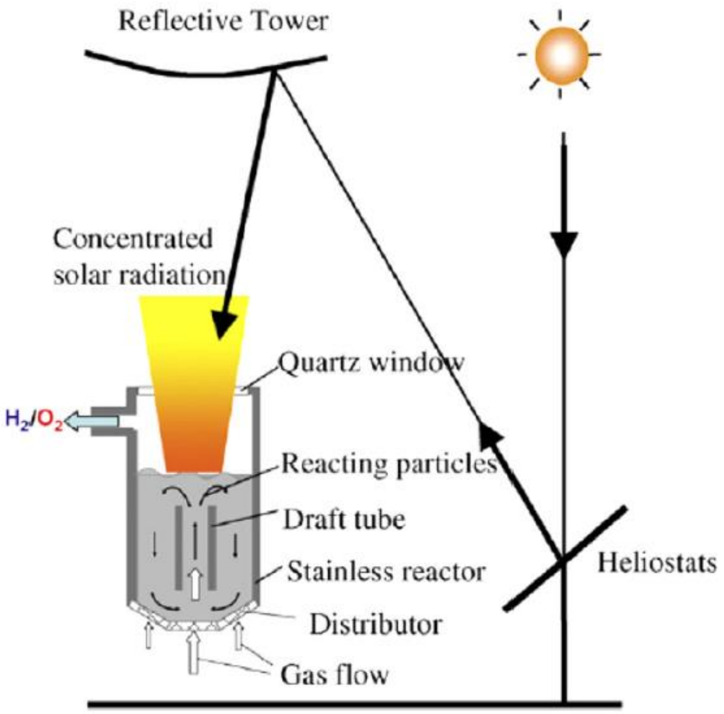

*Figure 26 | Spouted bed reactor schematic [24].*

### 2.6.2.1.3 Moving packed bed reactor

A consortium with the researchers from SNL proposed the moving packed bed reactor showed in the figure below.

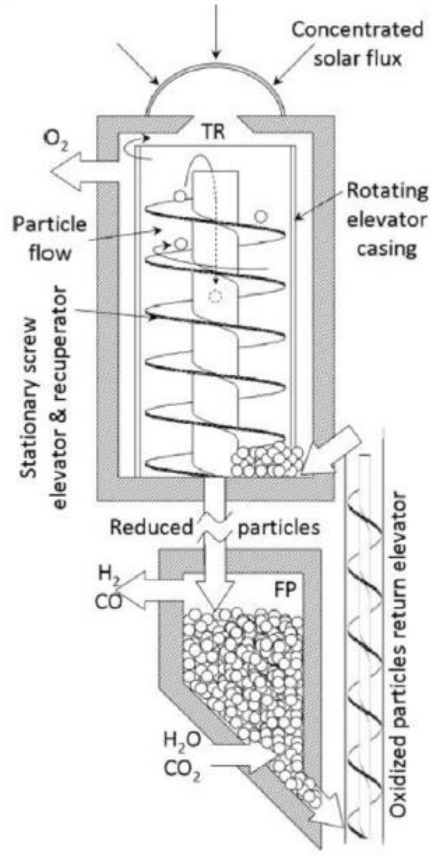

*Figure 27 | Moving packed bed reactor schematic [24].*

The metal oxide particles move towards the top of the reactor thanks to a screw elevator. Once on the top, the thermal reduction occurs. Here the solar radiation enters through a transparent window and directly heat the particles. During this first step, both $O_2$ and the reduced form of the metal oxide are produced: oxygen is expelled from the reactor while the reduced particles move in counterflow concerning the oxidized ones, pre-heating them (recuperation zone). In the end, reduced particles arrive at the bottom of the reactor, where react with $CO_2$ and $H_2O$ producing syngas.

From different simulations with ceria, the solar-to-fuel efficiency results above 30%.

### 2.6.2.1.4 Honeycomb reactor

The reactor concept is based on the collocation of catalyst powders as coatings of channels of the honeycomb reactor. The basic principle of reactor operation is shown below.

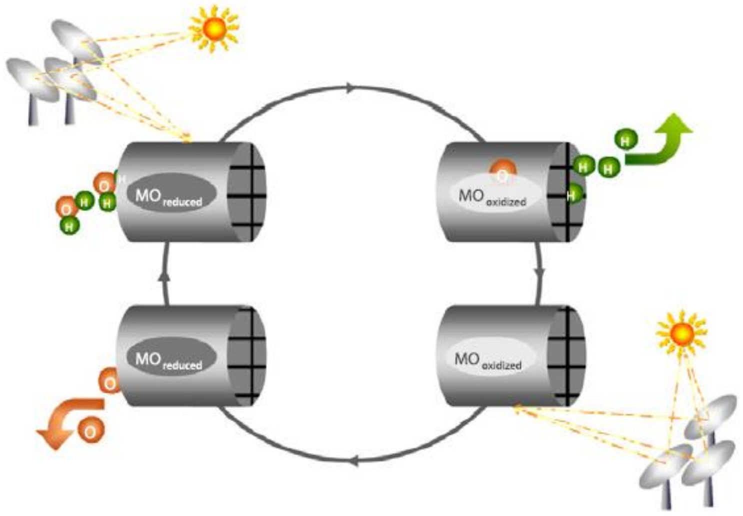

*Figure 28 | Operation sequence of the honeycomb reactor [24].*

An optimized version of this kind of reactor shows a hemispherical form with secondary reflectors. Two different areas can be distinguished:

1. "flat" area behind the transparent window. This part is square-shaped and it is made of non-redox material;
2. "domed" area just behind the first one that includes the redox-coated modules. The modules can be hexagonal, pentagonal or half-hexagonal.

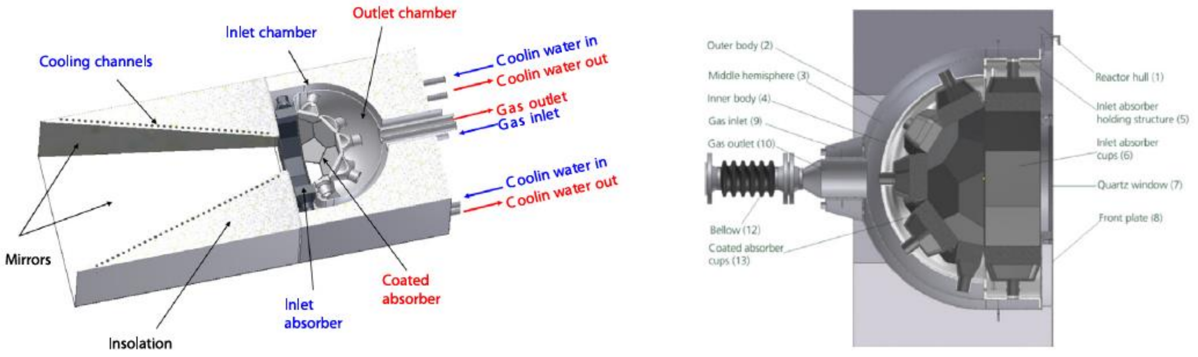

*Figure 29 | Optimized version of the honeycomb reactor [24].*

This configuration has different positive aspects. First, a homogeneous solar flux is guaranteed with a consequent better temperature distribution. Moreover, the re-radiation losses are reduced (most of the radiation is absorbed) thanks to the fact that different parts of the absorber look the others instead of the external area, simulating the "cavity" concept.

### 2.6.2.1.5 Ceramic foams reactor

A University group in Japan first study the ceramic foams reactor. The ceramic foam was made of Magnesia-Partially-Stabilized Zirconia (MPSZ) subsequently coated with the redox material, specifically $Fe_3O_4$, and c-YSZ particles. The TR step and the WS step were performed separately: TR at 1373 K in an electrically-heated furnace (Figure 30 b); WS at 1073 K thanks to a Xe lamp (Figure 30 a). The TR was performed using different $Fe_3O_4$ loading amounts (4.0 wt%, 6.9 wt%, 10.5 wt%). As a result of experiments, after 32 cycles, the $H_2$ production was successful but the YSZ/MPSZ foam was destroyed (Figure 31).

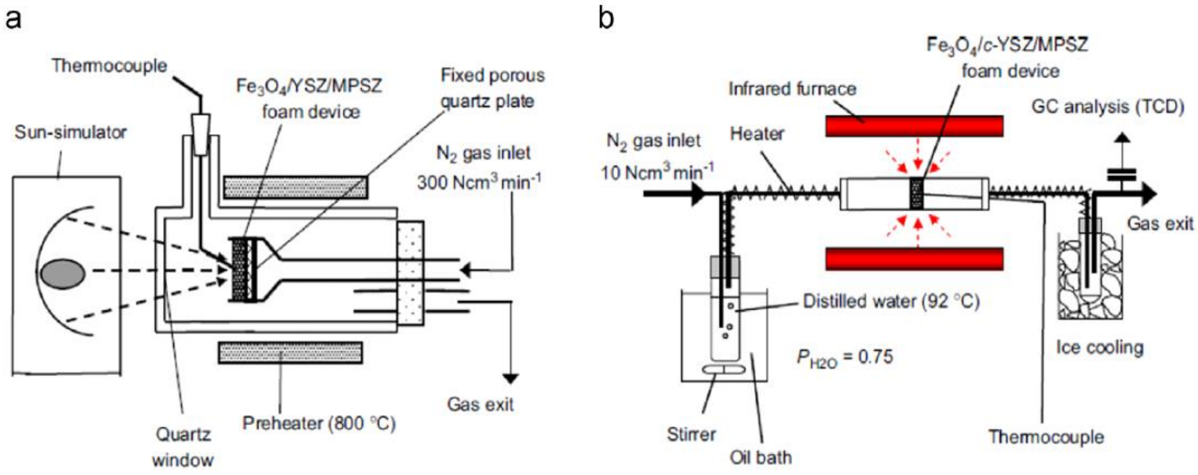

Figure 30 | (a) WS step; (b) TR step [24].

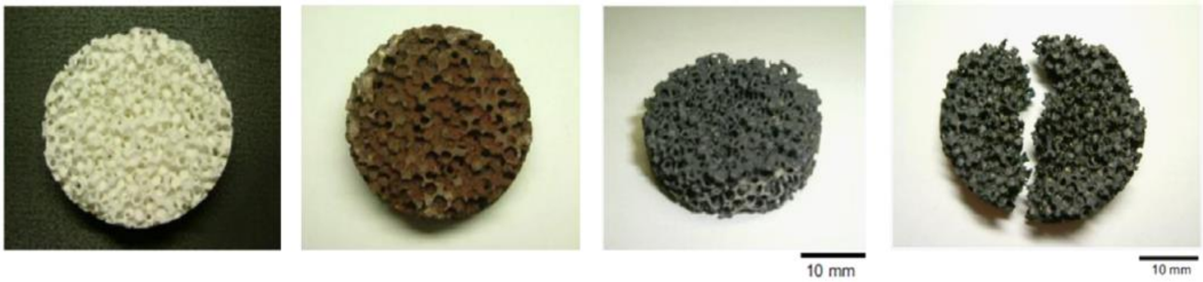

Figure 31 | YSZ/MPSZ foam at the end of tests [24].

A different analysis was performed by the ETH/PSI group that used a cavity receiver with porous monolithic ceria directly-exposed to the solar radiation. TR occurs at around 1873 K while CDS at around 1173 K. WS and CDS are performed in two separated steps. Inlet gases enter radially through the porous structure while outlet gases produced exit axially through an aperture collocated at the bottom of the reactor.

In a different study, but with a similar system, the maximum $CO_2$ conversion of 83% and a solar-to-fuel efficiency of 5.25% were achieved [7].

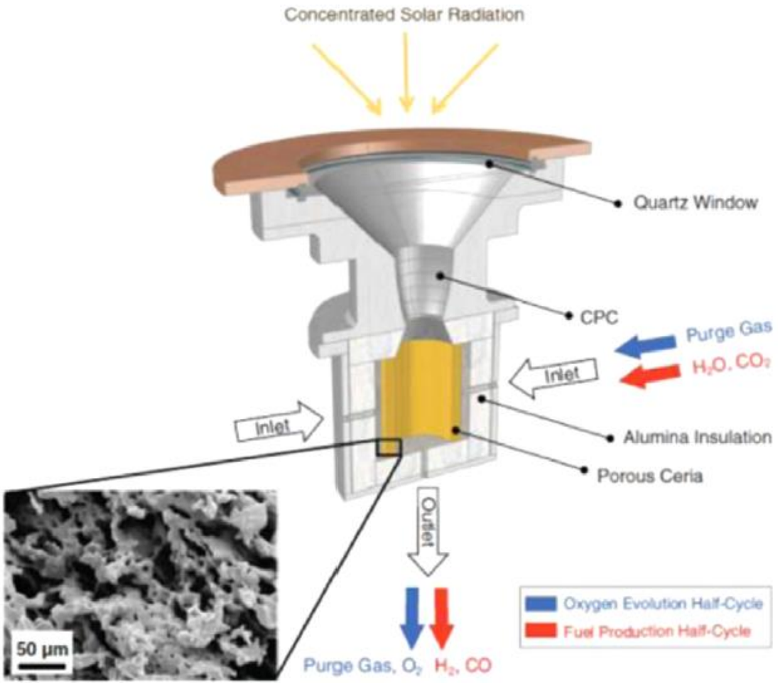

*Figure 32 | Porous monolithic ceria containing reactor schematic [24].*

Figure 33 shows an "optimization of the solar reactor for the combination of the two thermochemical splitting cycles for solar syngas synthesis" [24].

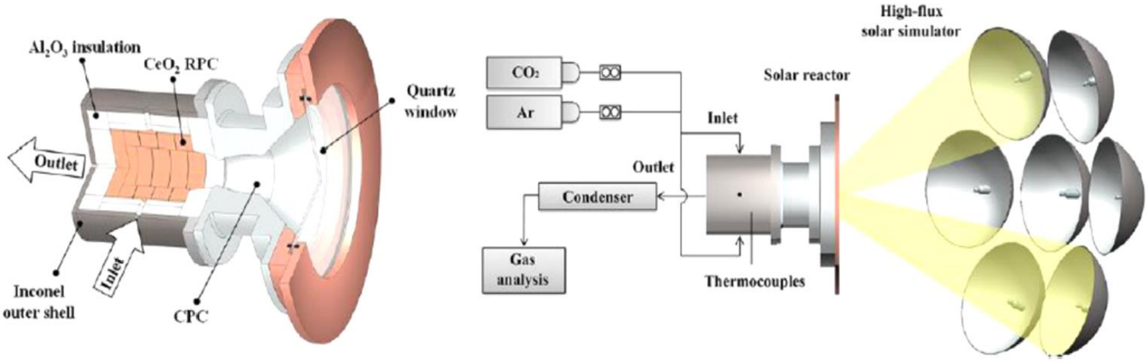

*Figure 33 | Optimized version of the ceramic foam reactor [24].*

Another reactor of this type was recently reported by Haeussler et al. [4] (Figure 34). The outer shell is composed of stainless-steel with a water-cooled system sealed with the quartz window. The reactive material is reticulated ceria foams in the form of 4 piled rings and one disk in the bottom part, forming a cavity that is insulated using alumina.

Three B-type thermocouples (T1, T2 and T3 in the figure below) and a pyrometer are used to detect temperatures in different points.

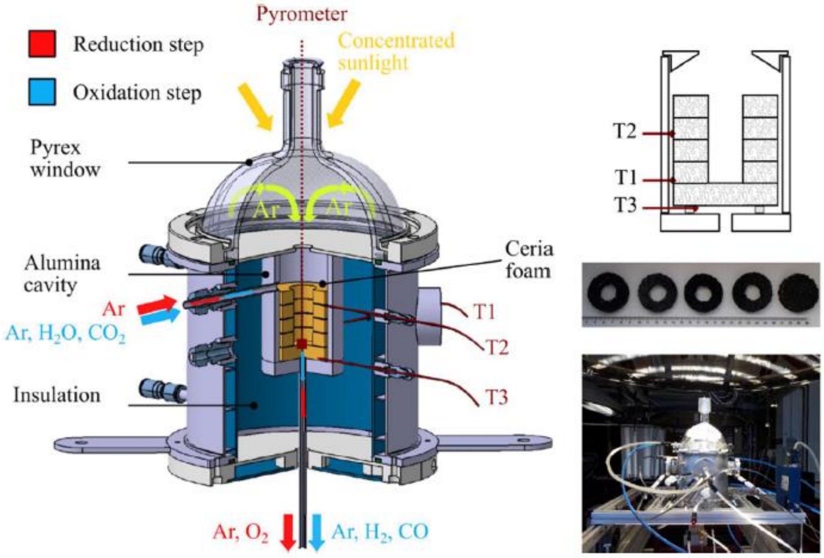

Figure 34 | Ceria foam reactor schematic [4].

### 2.6.2.1.6 Rotary-type reactor

This reactor was introduced by a research group in Tokyo. The redox pair material is the coating of the cylindrical rotor (it is highlighted by the blue arrow in Figure 35) of 40 mm diameter. The rotation is between two different chambers in which TR and WS are performed separately: looking at the figure below, the TR occurs on the right side while WS on the left one. The cylindrical rotor is coated separately with ceria and mixed ferrites ($Ni_{0.5}Mn_{0.5}Fe_2O_4$).

The test is not performed in real sun conditions but with a solar simulator.

The optimal temperatures founded when using the mixed ferrites were 1473 K and 1173 K respectively for the thermal reduction ($O_2$ production) and the WS ($H_2$ production) steps.

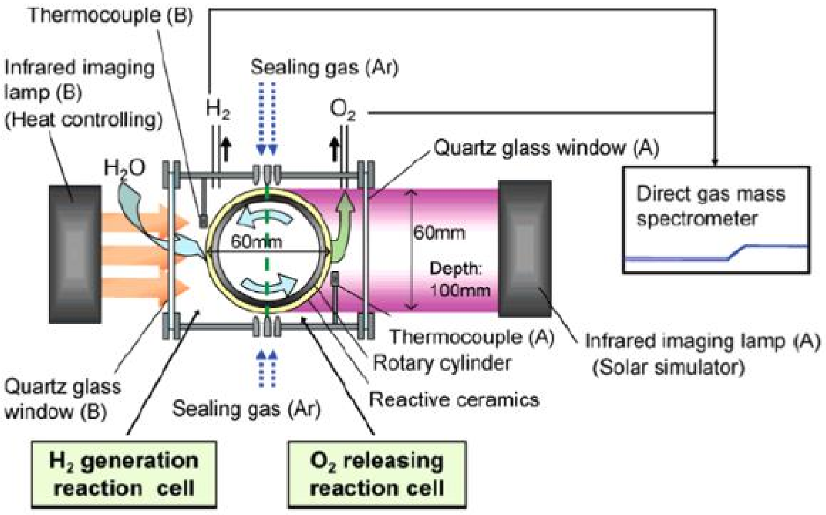

Figure 35 | Rotary-type reactor schematic [24].

Another improved version of such a reactor was proposed by an American group (Figure 36). The basic principle adopted is heat recuperation using two counter-rotating concentric cylinders. The outer one is made of porous reactive material rotating between the reduction zone and the oxidation zone. On the other hand, the inner cylinder is made of inert material, having the only rule to pre-heat the redox material before the reduction step.

According to some predictions, using thin cylinder walls and a long rotation period, over 50% of heat recovery can be reached.

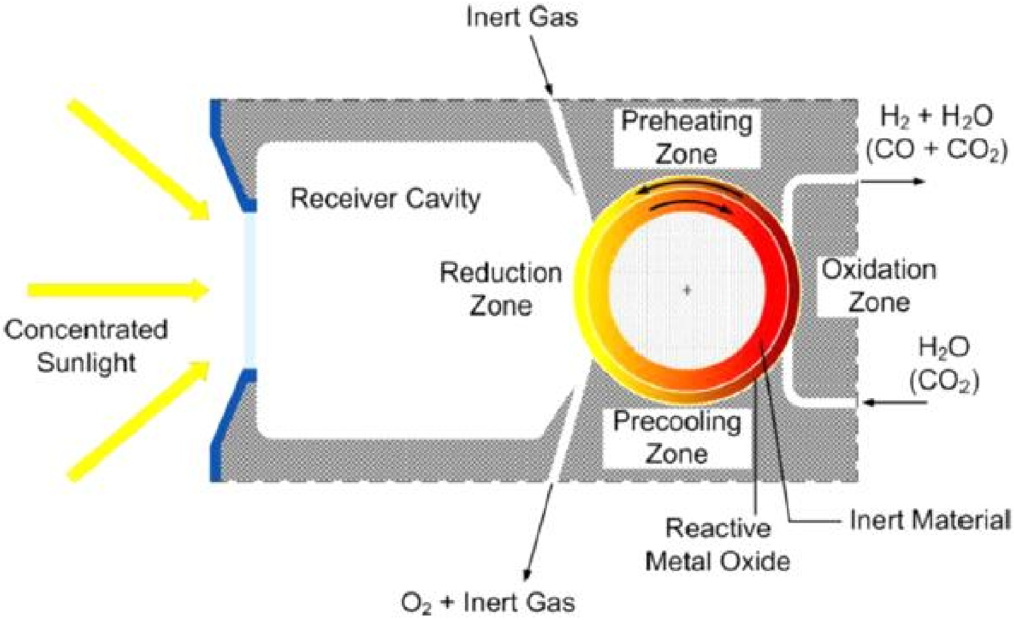

*Figure 36 | Improved rotary-type reactor with heat recuperation schematic [24].*

### *2.6.2.1.7 CR5 reactor*

CR5 is the abbreviation for Counter-Rotating-Ring Receiver-Reactor-Recuperator. The SNL group first proposed the concept only for the water-splitting process (Figure 37). The reactor is composed of a stack of counter-rotating rings made both of insulation material in the inner part and of reactive material on the external part. The counter-rotating rings have been ideated with the purpose of heat recuperation. Each ring rotates between two different zones at two different temperatures. The different rings rotation direction allows the pre-heat of the ring that has to pass through the reduction zone and the reduction of the temperature of that one that has to return in the re-oxidation zone (at a lower temperature). The rotation speed is on the order of one RPM or less.

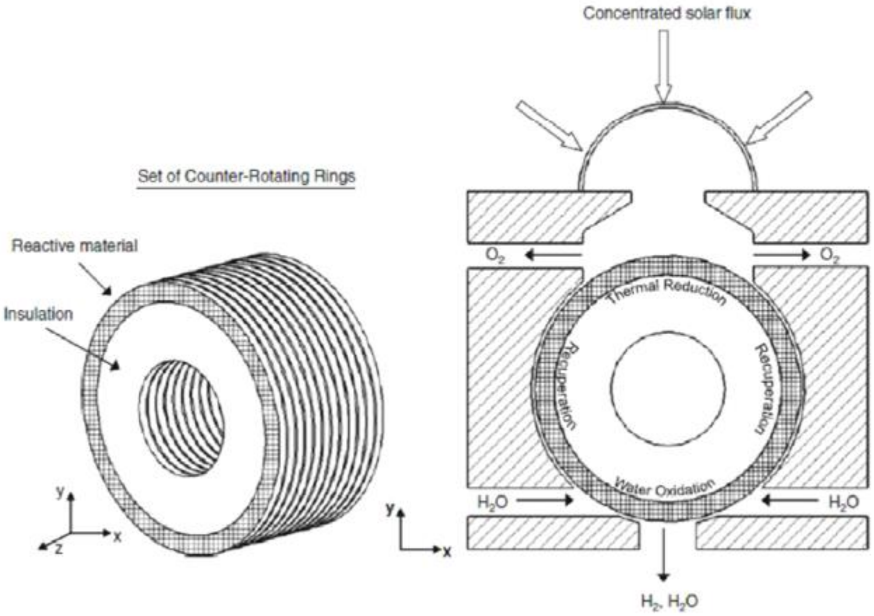

*Figure 37 | CR5: operating principle for WS schematic [24].*

The same group has also proposed to combine the splitting of water and carbon dioxide (Figure 38).

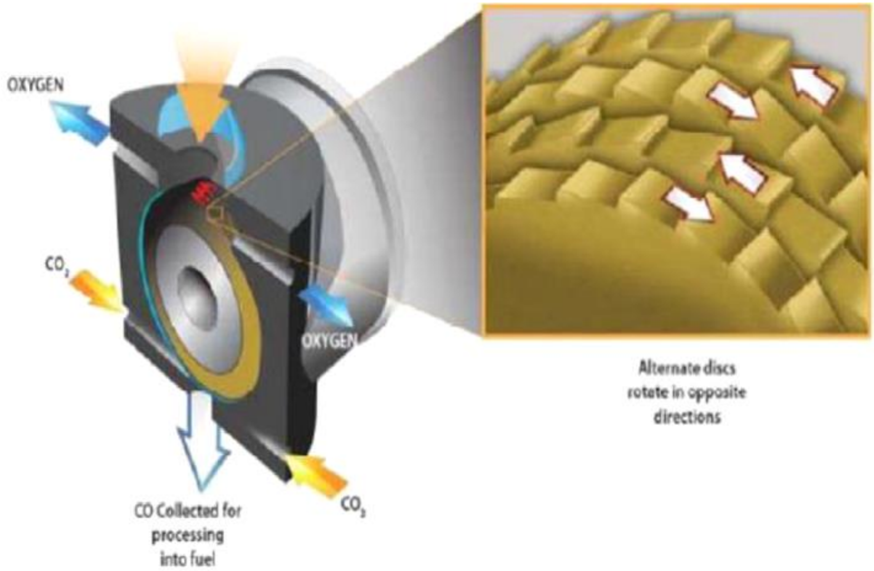

*Figure 38 | CR5: operating principle for CDS schematic [24].*

### 2.6.2.2 Indirectly-irradiated reactors

#### *2.6.2.2.1 Packed bed reactor*

A research group in Colorado has tested such an indirectly-irradiated reactor. It is composed of different tubes of which the central one is a packed bed filled with $Al_2O_3$ particles, $Fe_2O_3$-coated. For comparison, it was also filled with commercial $Fe_2O_3$ powder. The reduction occurs at around 1623 K while both WS and CDS are performed at 1373 K. The solar-to-hydrogen efficiency of the system composed of $Al_2O_3$

particles coated with $Fe_2O_3$ results in an order of magnitude higher concerning the one associated with commercial $Fe_2O_3$ powder. In Figure 39 a schematic of the described reactor helps to understand its structure.

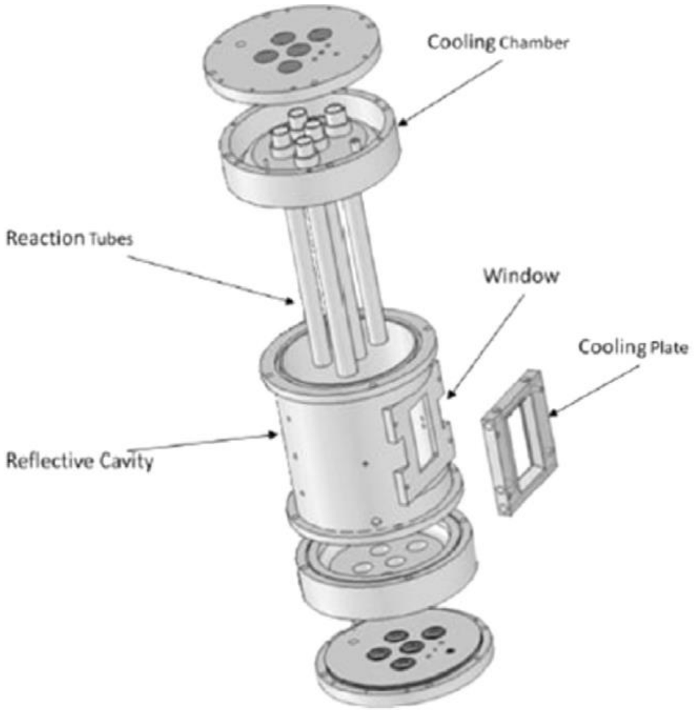

*Figure 39 | Packed bed solar cavity reactor schematic [24].*

# 3 TESTING METHODS

The experimental activities, which descriptions and results are reported in the next chapters, were conducted in two different laboratories:

- EC-Lab (Energy Center Lab);
- CCL ($CO_2$ Circle Lab).

This third chapter is dedicated to a detailed overview of the two laboratory configurations.

## 3.1 EC-Lab

The first part of the experimental activity was performed at the Energy Center Lab, which is a 2016 initiative of the Polytechnic of Turin. It is a research center focused on the study of technologies and integrated systems for the transition to a more sustainable society towards the use of energy and the environment [51].

### 3.1.1 Laboratory test bench

The laboratory test bench is located on the rooftop of the Energy Center. It is composed of a parabolic dish as a solar concentration system that directs the solar rays towards the receiver/reactor located on its focus (we are talking about a DIR). The reactor is simple alumina ($Al_2O_3$) hollow cylinder of around 20 cm length and 1.4 cm inner diameter and 1.8 cm outer diameter. As additional elements to the main players of the system, we can find all the accessories as electric connections, the electrical panel, thermocouples for temperature measurements, Ar and biomethane fuelling tanks with the associated mass flow controllers (MFC). All of them are needed for system functionality. The outputs of the system will be analyzed thanks to a paramagnetic $O_2$ analyzer from Emerson.

A photograph of the concentrator-receiver with the tracking system is reported below.

*Figure 40 |Concentrator-receiver with the tracking system.*

#### 3.1.1.1 Parabolic dish

As can be read in the operation and maintenance manual of El.Ma.srl (Riva del Garda (TN), IT) [52], the parabolic dish is composed of an aluminium paraboloid internally lined with a polymer film with high reflectivity and optical efficiency (80%).

*Figure 41 | Photograph of the parabolic dish before the installation [52].*

The solar tracking system is automatic and can be performed on two independent axes (azimuth and elevation) simultaneously or taking one axis fixed varying the other. In this way, the parabolic dish will receive at every instant the solar radiation with the best angle of incidence thanks to the calculation of the solar coordinates that are a function of the hour, day of the year, latitude and longitude. The input parameters for the calculation are added manually through a keyboard and a display, shown in Figure 42. Two different alarms can interrupt the solar tracking system. These are:

- *Wind alarm*: above a defined wind threshold (wind direction and intensity are obtained through the use of an anemometer) the concentrator will be positioned in a "safe position" to minimize the effects on the surface;
- *Temperature alarm*: above a defined temperature threshold (measured through a PT100 thermocouple) the system will be put in safety using a delay of the trajectory.

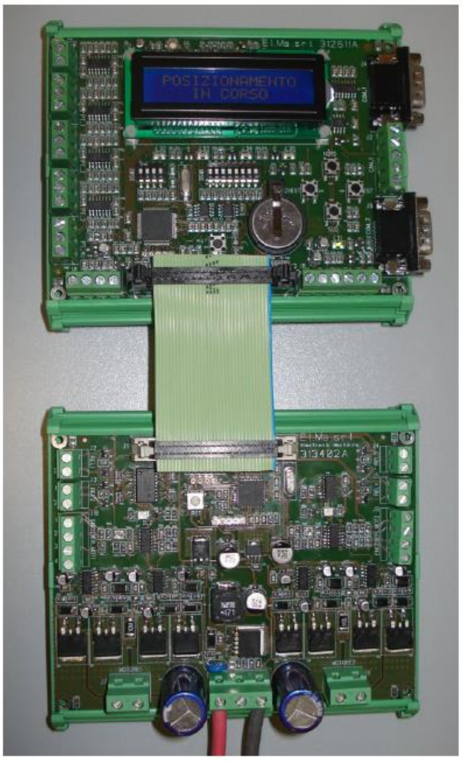

*Figure 42 | Keyboard and display for the input data for the solar tracking system [52].*

In Table 3 are reported some features of the concentrator.

| GENERAL TECHNICAL FEATURES | |
|---|---|
| Minimum operating atmospheric temperature | 0 °C |
| Maximum operating atmospheric temperature | + 35 °C |
| Relative humidity | 95% |
| Maximum overall dimensions | 3200 x 2800 x H3500 mm |
| Absorbing surface | 4.5 $m^2$ |
| Optical efficiency | 80% |
| **ELECTRICAL SYSTEM** | |
| Supply voltage | 220 V |
| Frequency | 50 Hz |

*Table 3 | Features of the parabolic dish.*

Considering the absorbing surface of 4.5 $m^2$ and the optical efficiency of 80% ($\alpha$=0.2, the 20% of the radiation is absorbed by the concentrator), in the optimal condition of 800 $W/m^2$ (solar irradiance achievable during summer), the focus can achieve theoretically a temperature above 1800 °C.

#### 3.1.1.2 Alumina reactor

The reactor is a hollow cylinder composed of alumina which is a refractory ceramic material and an insulator. It is the core element of the chemical looping reactions involving the oxygen carrier.

*Figure 43 | Alumina reactor on the rooftop of the EC-LAB.*

To constantly monitor the temperature in the reactor zone, four thermocouples are used:

- Three type N (Nicrosil, Ni-Cr-Si) thermocouples are located perpendicularly to the reactor axis in correspondence of three different reactor points (near the ends and one in the middle);
- One type B (platinum-based) thermocouple is placed inside the reactor cylinder, parallel to the reactor axis.

The location of the thermocouples can be better understood by looking at Figure 44 where are also reported the distances in cm.

*Figure 44 | Configuration of the thermocouples in the reactor zone.*

## 3.2 CCL

The $CO_2$ Circle Laboratory infrastructure promotes an articulated variety of innovative technologies for capture, storage and use of carbon dioxide emissions of anthropogenic origin. It focuses on the development of biotechnological, electrochemical and thermochemical processes, based on Renewable Energy Sources (RES), for the formation of products with high added value from $CO_2$, with sustainable process management. CCL has several locations, but that of our interest is in the A1 building of Environment Park in Turin.

### 3.2.1 Laboratory test bench

The first part of the experimental tests is executed in an oven heated alumina ($Al_2O_3$) tubular microreactor: 1 m in length and 8 mm inner diameter. Chemical looping reactions occur inside the microreactor (Figure 45). It is a continuous flow reactor: chemical reactions take place in a continuously flowing stream rather than in batch production.

*Figure 45 | Alumina tubular microreactors.*

The oxygen carrier used for all tests is iron oxides powder which is collocated manually in the middle of the alumina microreactor at the beginning of the experiment (furnace and the gas supply turned off) under a chemical hood (Figure 46). The weight of the powder is measured with a digital analytical balance (precision 0.1 mg), shown in Figure 47.

*Figure 46 | Chemical Hood.*

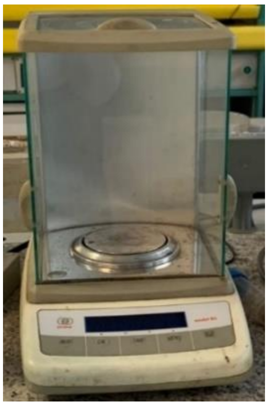

*Figure 47 | Digital analytical balance used for powder weight measurement.*

To constrain the powder to stay in the middle of the reactor we put quartz wool on both its sides. This is also useful to avoid the entrainment of the oxygen carrier in the continuous flow of reactants during experiments. In this regard, inside the microreactor is also located another alumina half tube (less than 0.5 m in length) of 6.4 mm inner diameter at the gas outlet to avoid the possible entrainment of the quartz wool together with the iron oxide powder. When the charging is ready, the alumina microreactor is placed into a tubular support called working tube (tube-in-tube configuration) inside an electrical furnace (that extends for all its length) and it is connected to the gas feeding and evacuation system, forcing the gases to pass inside the same reactor. The furnace, provided by Carbolite Gero (Figure 48), could work in the temperature range of 30-1700 °C, at atmospheric pressure.

*Figure 48 | Furnace from Carbolite Gero.*

The second part of the experimental tests is executed in an $Al_2O_3$ boat (Figure 49). Even in this case, it is filled with iron oxides powder. The procedure is more facilitate: after the weighing of the sample, this is simply located in the boat cavity under the chemical hood (nor quartz wool, nor alumina half tube are needed because the cavity itself prevents the entrainment of the oxygen carrier in the continuous flow of reactants).

*Figure 49 | Alumina Boat.*

When the charging is ready, the alumina boat is placed in the middle of the tubular support inside the electrical furnace (it is pushed with the help of a small alumina rod). At this point, it is connected to the gas feeding system: in this case, the gases will pass through the entire volume of the support. The gas inlet and outlet are attached to the edges of the working tube using flanges. To preserve them from high temperatures, small thermal shields made by cylinders of refractory material are interposed.

What follows is valid for both kinds of reactor configurations used.

Before starting the experiment, a leakage test is performed connecting the gas outlet to a flowmeter and verifying that the mass flow sent as input is nearly equal to that one at the output.

The reactor in the furnace is heated through resistances in which circulate current. This amount of current is regulated by an external power supply (Figure 50). Thanks to the software “Euroterm iTools” is possible to control the furnace by setting ramps (with the relative speed in °C/min) and periods of stasis based on what we need.

*Figure 50 | Furnace power supply.*

The test-bench pipelines are characterized by a gas supply system of 7 gas lines and by a vapour generation system connected with a demineralized water tank. Among the 7 lines, 5 of them are directly connected to the laboratory gas lines ($N_2$, $CH_4$, CO, $CO_2$, $H_2$) through pressure reducers installed on the wall, while the remaining 2 are connected to gas tanks (Ar mixtures) located under the hood with built-in pressure reducers on them.

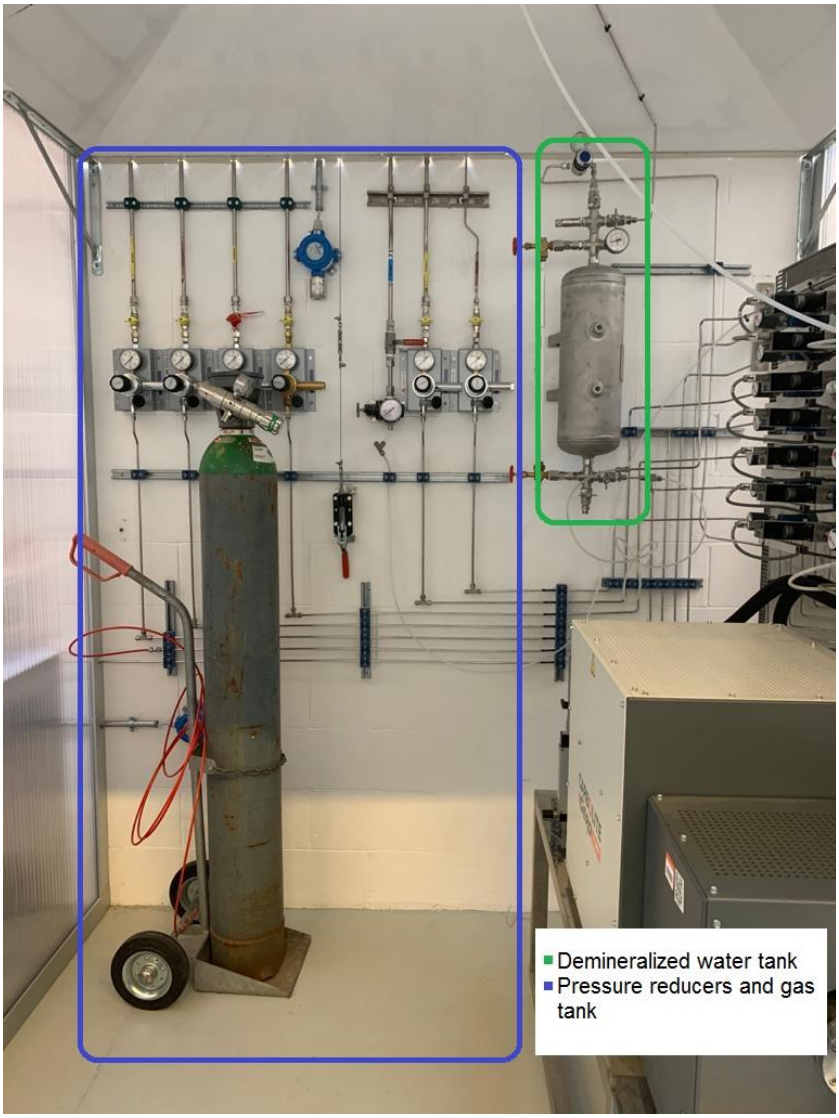

*Figure 51 | Pressure reducers, gas tank and demineralized water tank.*

The pressure of the gas lines is 2.5 bar, despite the $N_2$ line which is at 5 bar because this gas is also connected to the water tank to maintain it under-pressure. Each line has its mass-flow controller (MFC) that can regulate and measure the mass-flow. The pressure downstream of the MFCs is near the ambient one. Here all the gases converge in one single line (dry mixture line). Along the $N_2$ line, before the MFC, there is a deviation that connects the nitrogen with the water tank. The tank is connected to a water flow regulator and the meter connected in turn to a vapour generator. At the outlet of the vapour generator, there is a heated pipe to avoid condensation. The dry mixture line can be directly connected to the furnace or can be deviated towards the vapour generator for humidification thanks to the first three ways valve. At this point, the mixture (dry or wet) can be directly sent to the furnace or the bypass with the action of the second three ways valve. The furnace and the bypass lines converge at the outlet in one single line. Here is possible to choose if the mixture will be sent to the condenser or directly to the exit line. Both the possibilities can be then connected to the discharge into the hood or to the gas analyzer. Naturally, at the outlet of the gas analyzer, there is again the connection to the discharge into the hood.

A SCADA-based software controls the MFCs, the vapour generator and the pneumatic three-ways valves located in the pipelines connected to the reactor.

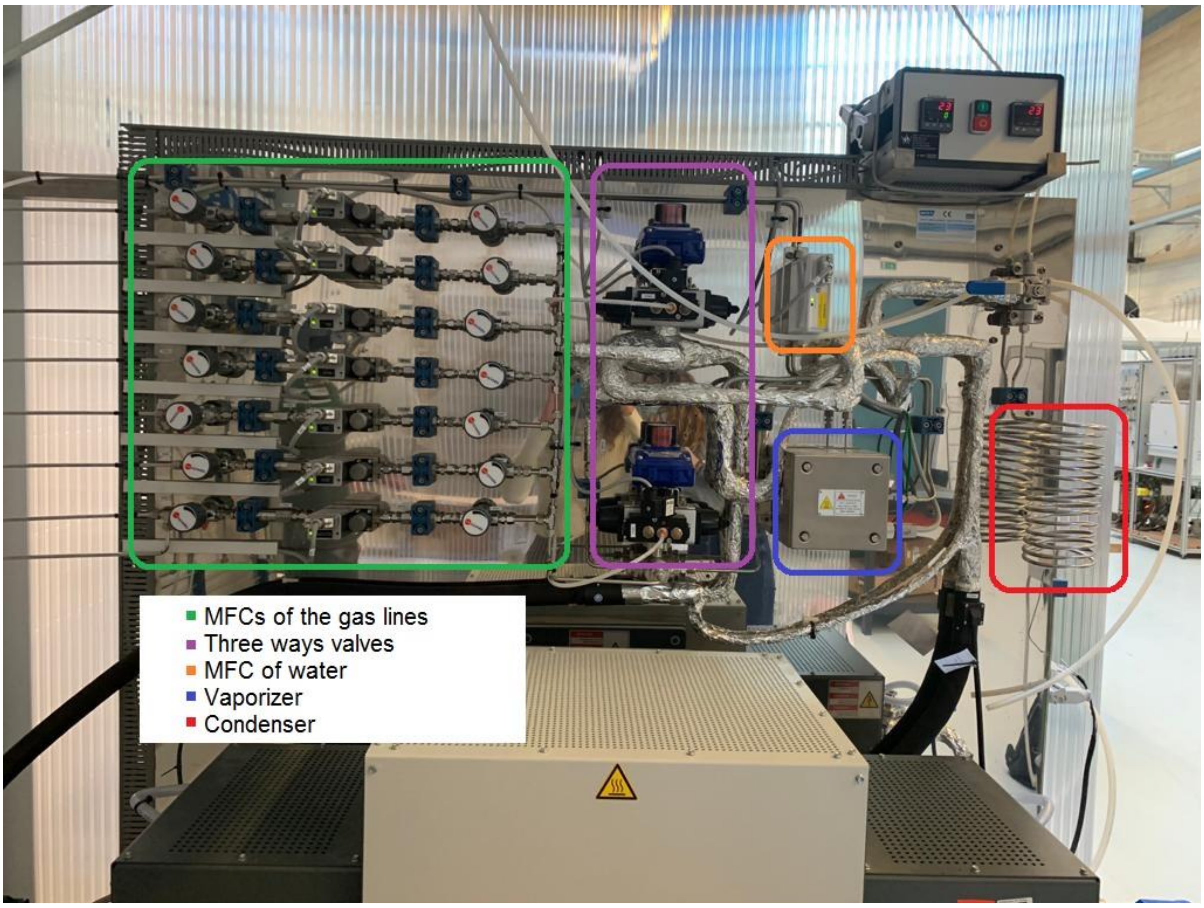

*Figure 52 | Pipelines of streams connected to the microreactor.*

The gas analyzer used to analyze the gas mixture at the outlet of the system is produced by Emerson (Figure 53). The analyzer is based on TCD and IR detectors for the measure of the following gases: $H_2$, CO, $CH_4$ and $CO_2$. Before entering the analyzer, the mixture passes through a stainless-steel and water droplets filter to protect the instrument from impurities and liquid water. At each time step (which is chosen by the user), the measured values in ppm of the different gases constituting the mixture are given as output. It has a user interface (software “XStream") that displays measured values, status and error messages and menus for the input parameters. Before every test is performed the calibration of the instrument following the concentration values of the input gases and on those that we expect for the produced gases.

*Figure 53 | Emerson gas analyzer.*

A more schematic representation of this system is given in Figure 54.

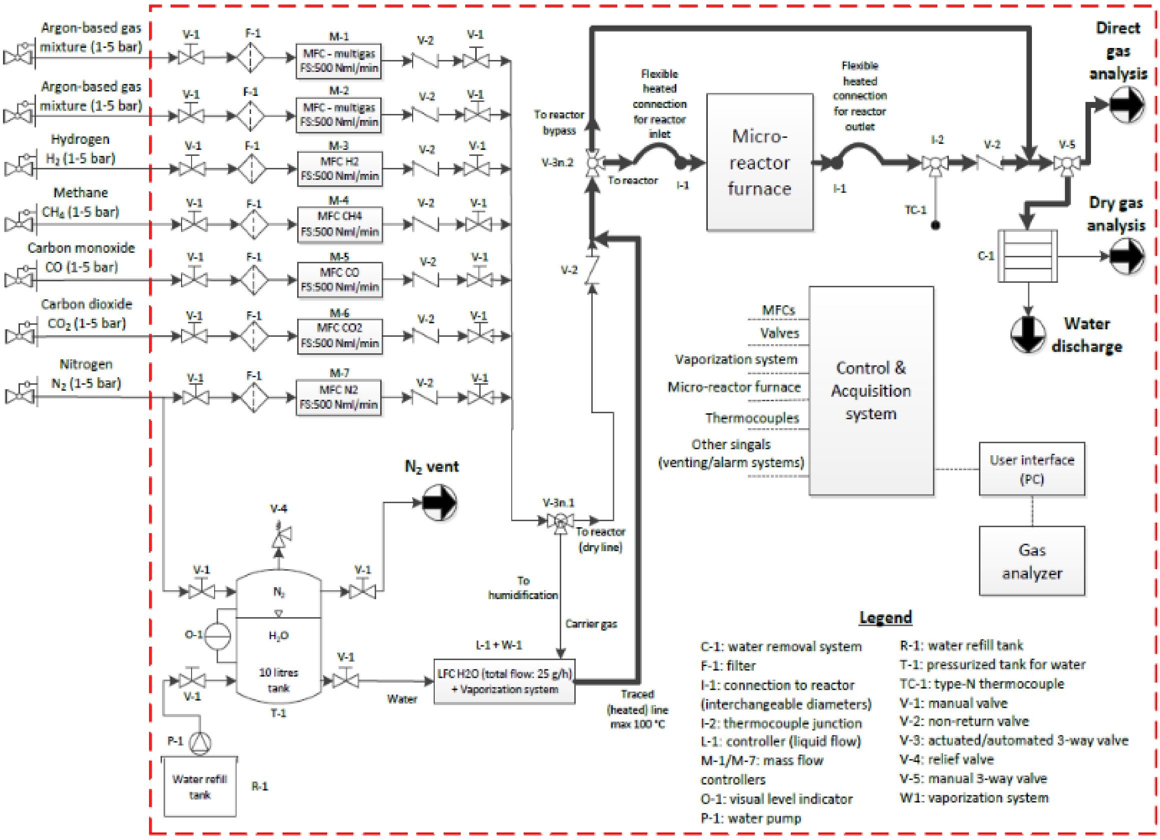

*Figure 54 | Schematic of the complete test bench.*

# 4 CONCENTRATOR-RECEIVER SYSTEM MODELLING

## 4.1 Reactor temperature analysis

Before going into the details of the chemical looping process, an introductive study for the analysis of the Energy Center reactor temperature variation over time was performed. A detailed description of the system layout and its characteristics is reported in section 3.1. In this context, the reactant is not needed yet and so the productive system is not active. In other words, we will focus our attention on the energy absorbed from the reactor, as a result of the concentration system, and on its consequent temperature variation.

The objective of the analysis is to evaluate the feasibility to perform chemical looping processes, with the relative production of syngas, using a solar concentration system. The evaluation of the operative temperature is also fundamental for the choice of materials to be used for all the accessories of the system.

A geometrical optics model and an interconnected heat transfer model for the reactor are needed for its temperature evolution prediction, giving the global radiation data as input. The calculation of the reactor temperature must consider all the effects that tend to reduce its value, as convective, radiative and conductive losses. The system is equipped with four thermocouples that record the temperatures around and inside the reactor at each time step. The values stored during the winter experimental activity are used for the validation of the model together with the condition declared by the manufacturer [52] under which with 800 W/m$^2$ the receiver can reach around 1800 °C.

To obtain reasonable results, we have chosen to produce a comparison of temperature trends for each meteorological season. What we expected to see is higher temperatures (associated with higher radiation) during summer when the system producibility would be optimal due to the higher energy received by the concentrator.

### 4.1.1 Theoretical review

Two are the main phenomena that can occur when solar radiation interacts with a medium [53]:

1. *Refraction*: deviation of a propagation wave that passes from one medium to another with a different refractive index where its propagation velocity changes. This phenomenon can be explained by Snell's law below:

$$\mathbf{n_1 sin\theta_1 = n_2 sin\theta_2} \qquad 4.1$$

Where:

- $n_1$: refractive index of medium 1;
- $n_2$: refractive index of medium 2;
- $\theta_1$: incidence angle between the incident ray and the normal to the interface;
- $\theta_2$: refractive angle between the refracted ray and the normal to the interface;

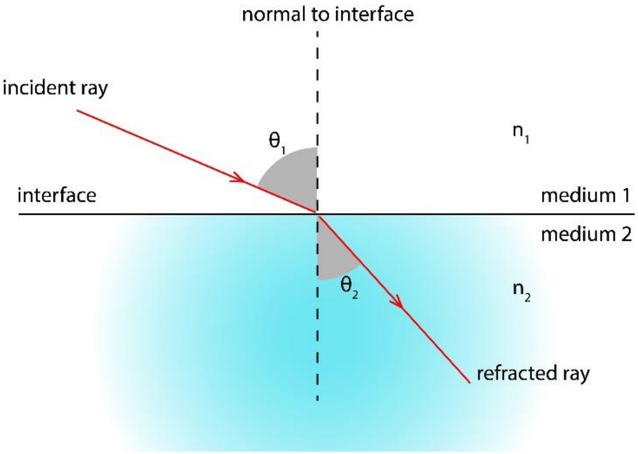

*Figure 55 | Refraction phenomenon.*

2. *Reflection*: when the propagation wave impacts with a reflective surface, it is reflected keeping the same angle with the normal to the surface.

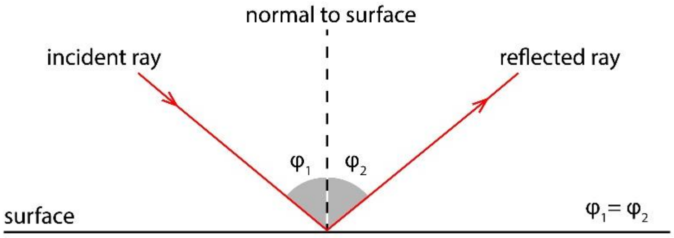

*Figure 56 | Reflection phenomenon.*

In an ideal theoretical condition, the parabolic concentrator can concentrate the rays (after having reflected them) in an infinitesimal point located on its focus. In reality, this cannot happen due to different perturbations that affect the system. Among the perturbations we can find [53]:

- *Absorption*: as was already reported in section 3.1.1.1, the optical efficiency of the parabolic dish is 80%. This means that the remaining 20% of the radiation is absorbed and not reflected.

The absorbed fraction is indicated with the Greek letter alpha (α). So, in the specific case of the following analysis, α will be equal to 0.20.

- *Specularity error*: the mirror that reflects the radiation can show very local roughness effects linked to the production process. This defect of the surface implies a deviation of the reflected ray that will not follow the ideal direction. This means that it is impossible to concentrate the radiation in an infinitesimal point on the focal plane with a consequent much more large area of the reactor involved.
- *Sun shape*: this term refers to angle variation in solar irradiance. If the Sun is considered as a point-like source, the sun rays will be emitted all parallel to the others. In reality, the Sun is big enough, even if it is far away from the earth, and the emitted rays, that are generated from different parts of it, create significant angles between them (cannot be considered parallel). In other words, the incident rays on the Earth trace a cone with an aperture half-angle of $\theta_s$=4.65 mrad.

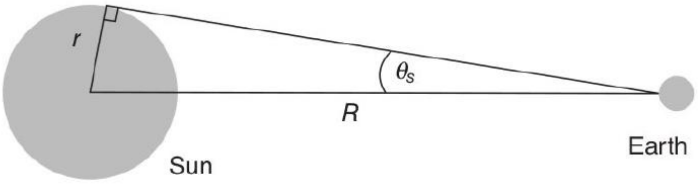

*Figure 57 | Sampling cone of rays from the solar disk [53].*

The *limb darkening* is the second effect connected to the sun shape. The radiation emission from the sun is a volumetric effect and the optical thickness which energy must pass through is larger at the edges of the sun rather than at the center. Because of that, the radiation emitted from the center is much more intense than that one from the edges.

### 4.1.2 Modelling tools

A 3D modelling of the parabolic dish and the receiver will be constructed to subsequently obtain the flux and temperature distribution in the reactor surface. The efficiency of the chemical looping process will be largely affected by the uniformity of the flux on the reactor surface.

COMSOL Multiphysics is the tool used for the study. It is a multiphysics simulation software based on the FEM (finite element method) which consists of discretizing the continuum with a set of finite size allocations.

The geometrical optics simulation is performed with the Ray Optics Module. It allows modelling the electromagnetic wave propagation with a ray-tracing approach. The propagating waves are treated as rays that can be reflected, refracted or absorbed at boundaries in the model geometry. The Ray Optics

Module seems to be the best choice for the determination of the trajectory of the reflected rays even if this treatment of electromagnetic radiation uses approximations that are appropriate when the geometry is large compared to the wavelength.

### 4.1.3 COMSOL model

#### 4.1.3.1 Geometry design and mesh

The system is composed of a parabolic reflector and a cylindrical receiver. The parabolic reflector is chosen using the Ray Optics Module library under the 3D mirrors category.

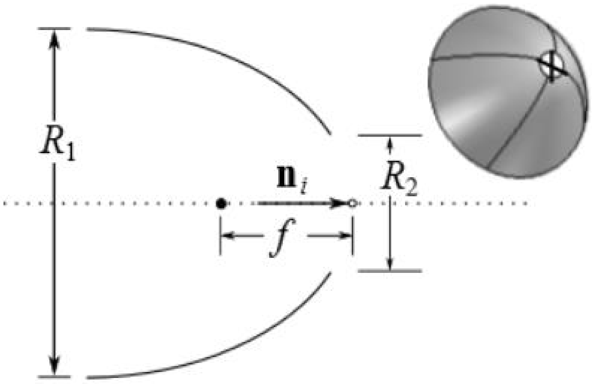

*Figure 58 | Paraboloidal Reflector Shell 3D.*

After the selection, some input parameters must be defined as the rim angle and the focal length. A representation of the two quantities is shown in the figure below.

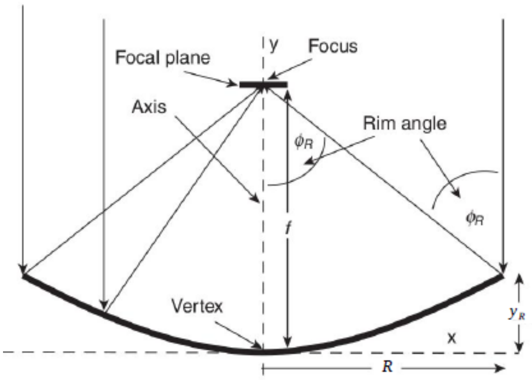

*Figure 59 | Representation of the rim angle and the focal length [53].*

The dish diameter will be then automatically evaluated by the program, which can display the geometrical configuration with the correct dimensions. The formula that correlates the three above-mentioned quantities is reported below:

$$\mathbf{D_{dish} = 4 \cdot f \cdot (csc(\phi_R) - ctg(\phi_R))} \tag{4.2}$$

Where:

- f: Focal length;
- $\phi_R$: Rim angle.

The dish diameter will be then used to calculate the relative surface area that is needed in the ray-tracing simulation that follows.

After having constructed the dish geometry it is possible to move on the receiver. It is a hollow alumina cylinder with the following dimensions:

- $D_{in}$ = 1.4 cm;
- $D_{out}$ = 1.8 cm;
- L = 20 cm.

It has to be located in the center of the parabolic dish at a distance equal to the focal length.

The complete geometry of the system is obtained after having introduced all the correct dimensions. Moreover, on the parabolic dish and the absorbing surface of the receiver, is generated an extremely fine mesh that will allow the calculation of all the quantities of our interest.

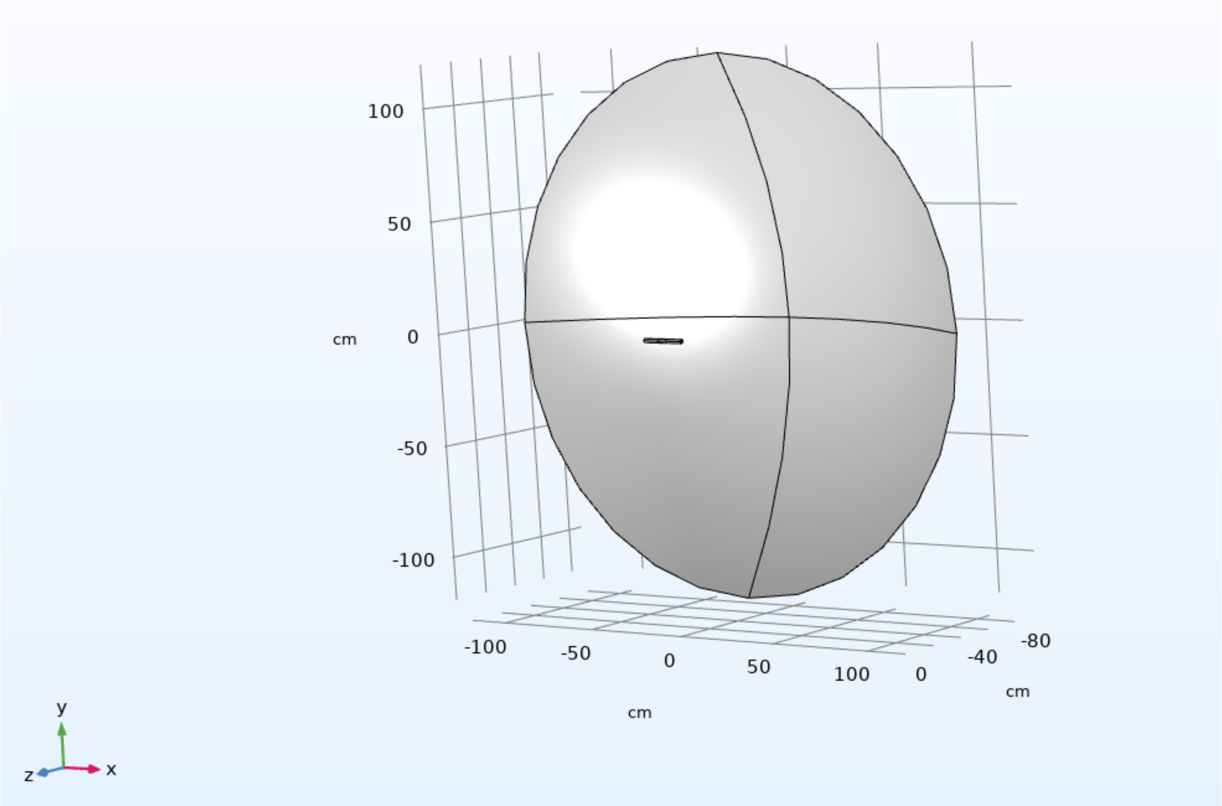

*Figure 60 | Geometrical design of the system composed of the parabolic dish and the receiver.*

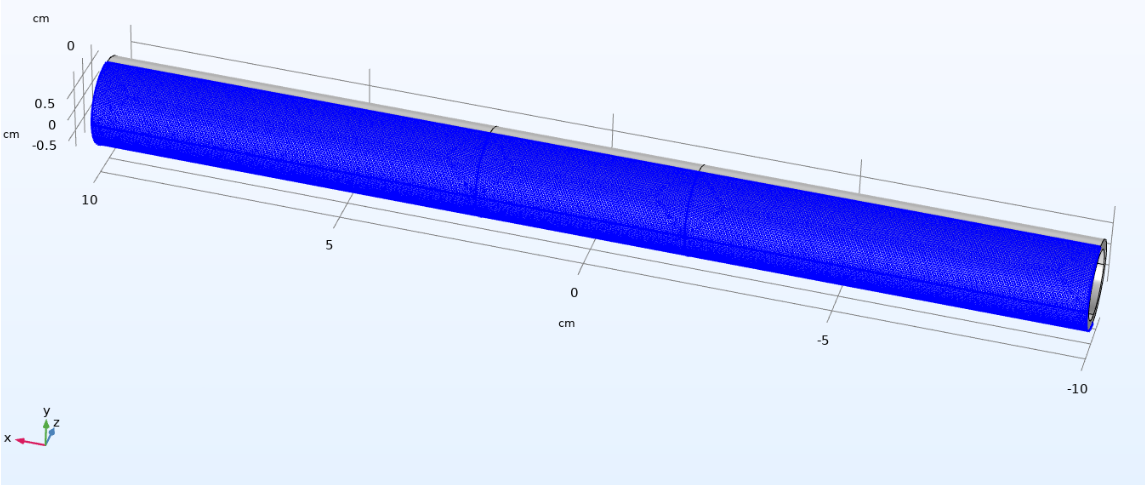

*Figure 61 | Mesh for the absorbing surface of the receiver.*

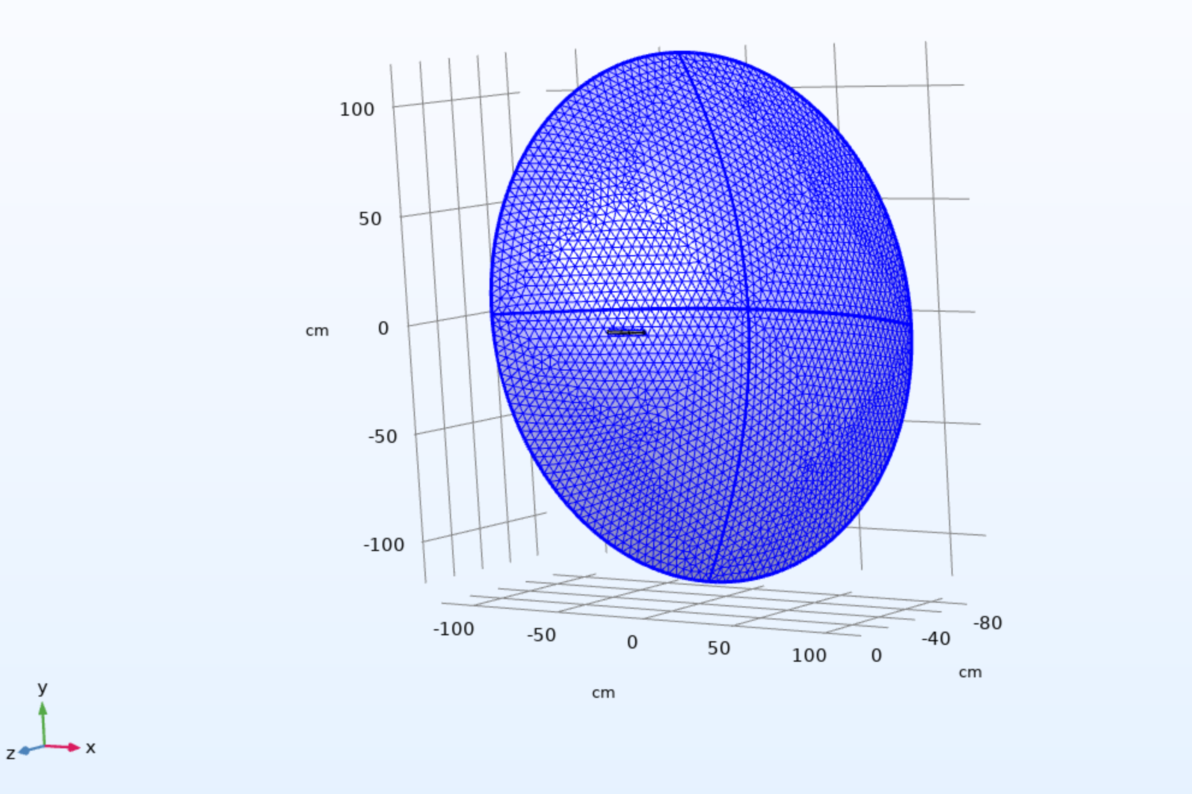

*Figure 62 | Mesh for the parabolic dish.*

#### 4.1.3.2 Ray-tracing simulation

A numerical calculation strategy is used for the evaluation of temperature and heat flux distribution on the focal plane of the Energy Center concentrator. The reflected and released solar radiation is evaluated with the Ray Optics Module in COMSOL, characterizing the parabolic surface with the “Illuminated Surface” function. The direction of the released rays extremely depends on the direction of the vector of the incoming beam and the normal to the surface. After being reflected, the solar radiation reaches the focal plane surface and is subsequently arrested from the "Wall" function which models the absorbing receiver surface.

The ray-tracing simulation performed in this way allows taking into consideration the angle variation in solar irradiance, the limb darkening, the local surface roughness and the absorption from the parabolic dish. All these phenomena will reduce the solar radiation intensity on the receiver concerning the ideal condition. If the parabolic dish was a perfect reflector, without local roughness, and if the solar rays were emitted from a punctual source as flat wavefronts, the incoming radiation will be concentrated in an infinitesimal little point in the focal plane of the parabolic dish, increasing the efficiency of the system.

The sampled rays are released from 100,000 distinct points. Consistent with the conical distribution, they take account of the maximum opening angle of the solar disk $\psi_m$ = 4.65 rad. The limb darkening model, assigned in the “Illuminated surface” section, follows an exponential trend consistent with an empirical power law. The surface of the concentrator has a superficial roughness which implies that the reflected rays will deviate in random directions. To be noticed that not all the solar radiation is reflected from the parabolic dish, a fraction of this radiation will be absorbed from the same. The value of the absorption coefficient is given by the manufacturer [52]: α = 0.2. From this value is then calculated the reflection coefficient: 80% of the radiation will be reflected.

The considered intensity for the incident rays is 800 W/m$^2$ (I0) while the total source power is calculated as:

$$\mathbf{P_{src} = A \cdot I0} \tag{4.3}$$

Where A identifies the area of the front surface of the dish.

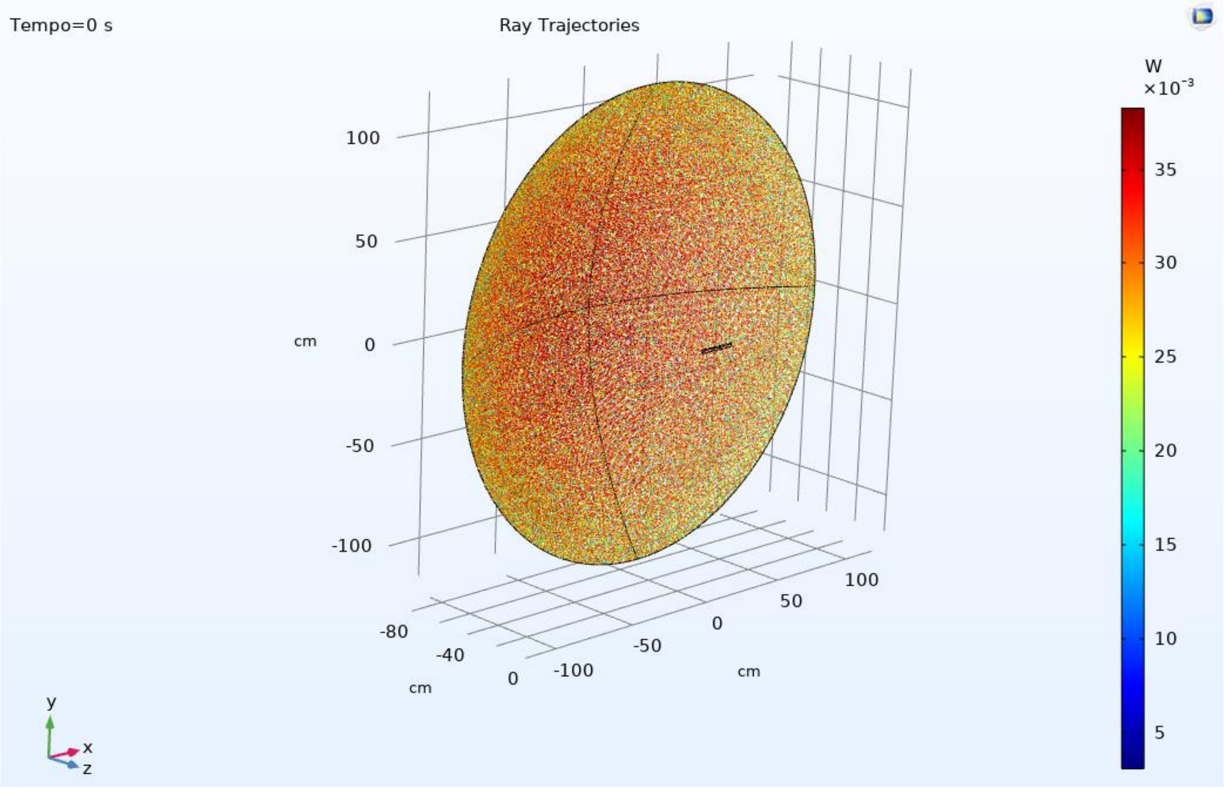

*Figure 63 | Distribution of incident rays on the reflector in terms of power density [W].*

The spatial distribution of the deposited power is heterogeneous because the rays randomly reach the surface of the concentrator, as a consequence of the darkening phenomenon at the edge of the solar disc. Therefore, the central and the peripheral zones of the parabolic dish equally contribute to rays reflection towards the focal plane.

The trajectories of the reflected rays from the parabolic dish surface are shown in Figure 64. It is visible that a huge number of rays are not able to reach the center of the receiver, reflecting on the walls of the horizontal cylinder, being re-emitted. In this way the efficiency of the receiver will be reduced concerning the ideal case.

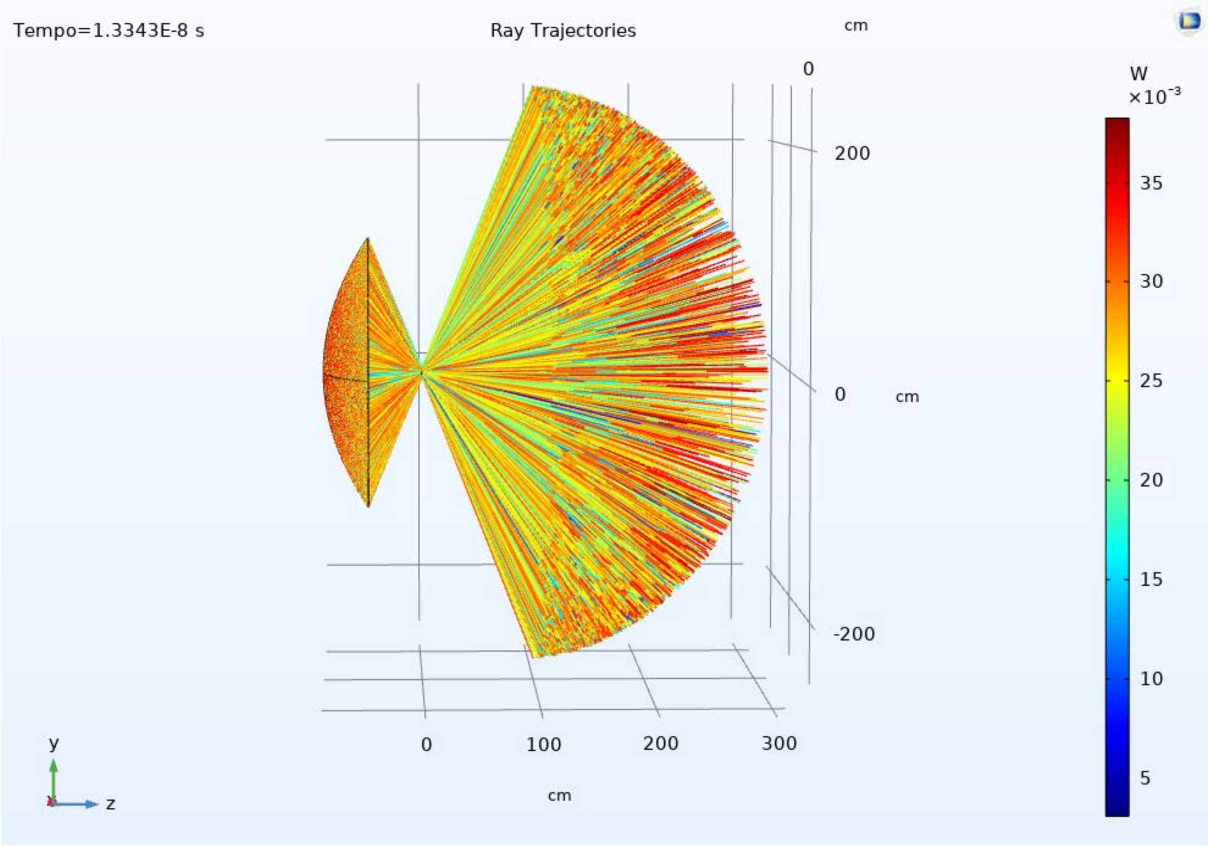

*Figure 64 | Trajectories of the reflected rays towards the receiver.*

#### 4.1.3.3 Input data summary

For an easier comprehension of the concentrator/receiver system model developed in COMSOL Multiphysics, a summary of the principal input instruction is outlined below.

MODEL CREATION:

Model geometry → 3D geometry

Physics → Optics > Ray Optics > Geometrical Optics (GOP)

Study → Ray-tracing simulation

GEOMETRICAL AND PHYSICAL PARAMETERS:

| Name | Expression | Value | Description |
|---|---|---|---|
| *f* | 0.885[m] | 0.885 m | Focal length |
| *phi* | 68[deg] | 1.1868 rad | Rim angle |
| *d* | 4*f*(csc(phi)-cot(phi)) | 2.3878 m | Dish diameter |
| *A* | pi*d^2/4 | 4.4779 $m^2$ | Dish projected surface area |
| *psim* | 4.65[mrad] | 0.00465 rad | Maximum solar disc angle |
| *sig* | 1.75[mrad] | 0.00175 rad | Surface slope error |
| *I0* | 0.800[kW/m^2] | 800 $W/m^2$ | Solar irradiance |

GEOMETRY AND MESH:

Receiver → Horizontal cylinder

Parabolic dish → Ray Optics Module > 3D > Mirrors > Paraboloidal Reflector Shell 3D

GEOMETRICAL OPTICS (GOP):

Parabolic dish → Illuminated Surface ($\alpha = 0.2$)

Receiver absorbing surface → Wall

#### 4.1.3.4 Results

The results of the simulation model, in terms of heat flux and temperatures associated with the reactor absorbing surface, are obtained considering the ideal solar irradiance of 800 W/m$^2$. This value is reported in the parabolic dish manufacturer manual [52] as the maximum radiative flux. Moreover, is specified that with this value of ideal solar irradiance, also considering an optical yield of 80% and a surface of 4.5 m$^2$, in the focal point is possible to achieve theoretically a temperature above 1800 °C. This value of temperature will be used for the first validation of the model.

The objective of the analysis is to evaluate the feasibility of a chemical looping process developed in the reactor of the Energy Center Lab. In this context is fundamental to evaluate temperature and deposited power in the receiver to understand if these values are sufficient to sustain the thermochemical reaction associated with the process.

Starting with the focal plan deposited power (Figure 65) is visible that the concentration surface is characterized by an elliptical shape. This is the consequence of the dispersion of the reflected rays liked to the superficial roughness of the parabolic dish as well as to the effects of sun shape that tend to spread the thermal flux over a wider region in the focal plane concerning the ideal case for which the ray concentration is much more precise. For what concerns the intensity of the deposited power, it is reduced as a direct effect of the limb darkening phenomenon. Even the parabolic dish absorption of the radiation contributes to reducing the power intensity. The maximum value achieved in the focal plan center is $1.18 \cdot 10^7$ W/m$^2$.

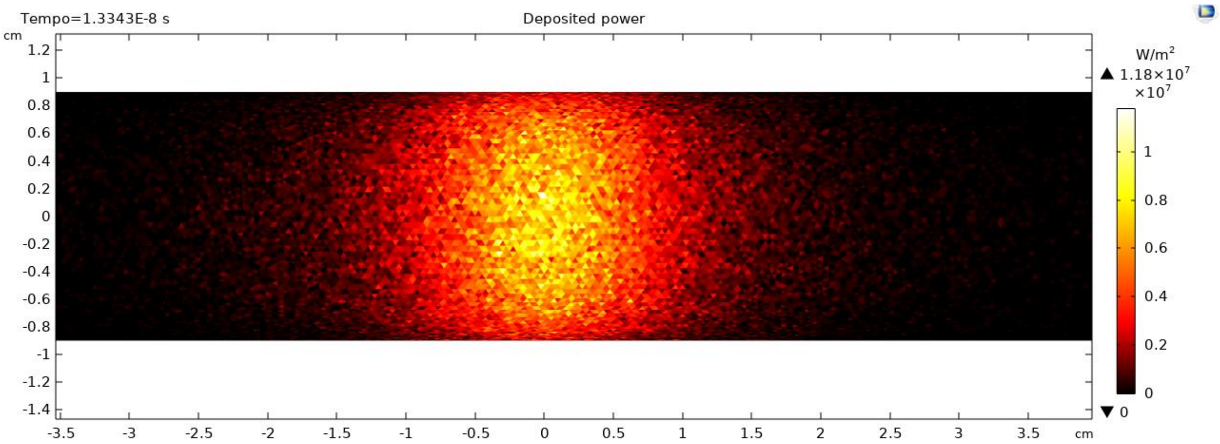

*Figure 65 | Deposited power in the focal plane of the parabolic dish.*

The 3D distribution of the deposited flux is reported below for better visualization of the entire geometry.

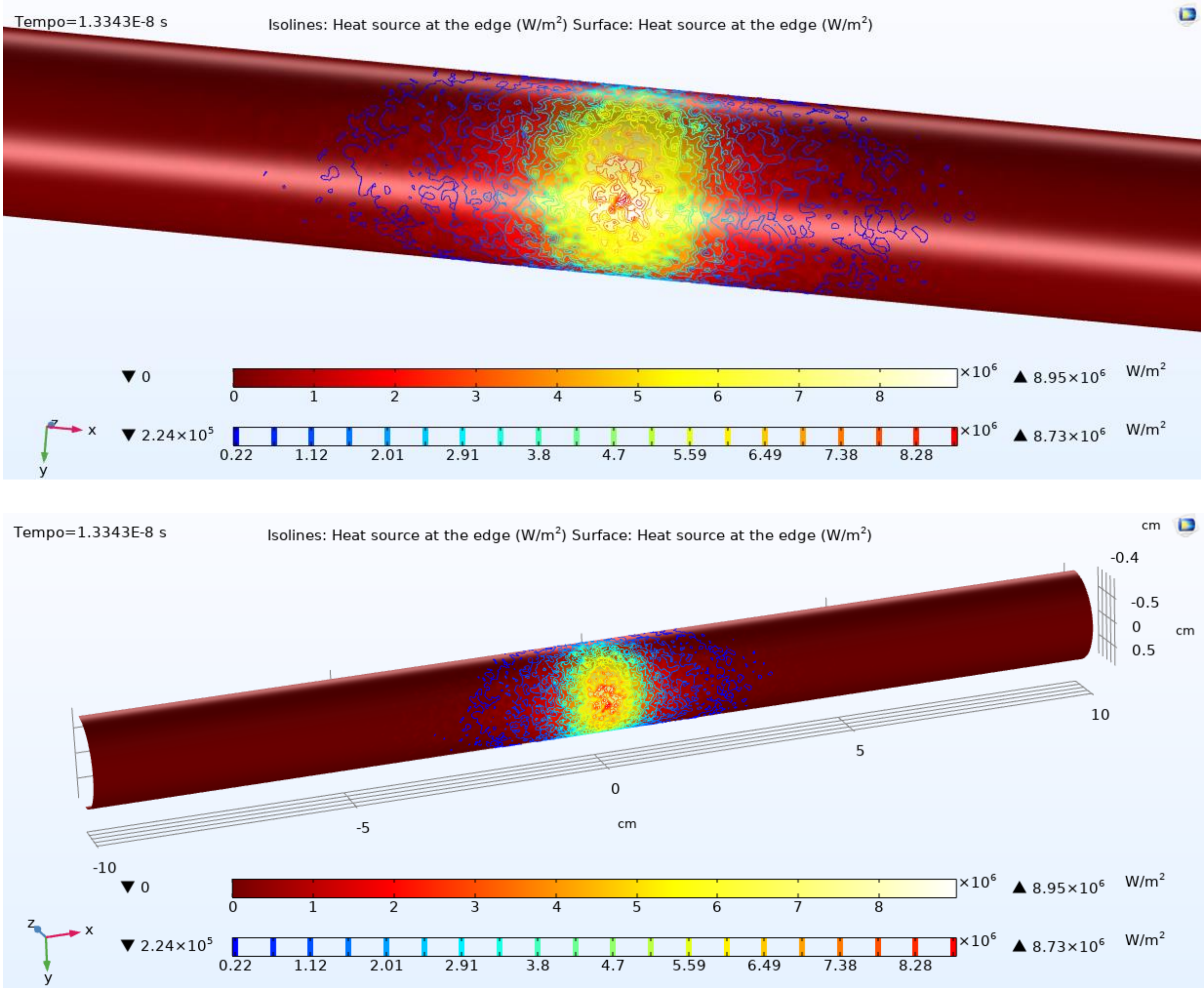

*Figure 66 | 3D distribution of the heat flux in the focal plane of the parabolic dish.*

The temperature distribution in the focal plane is equivalent to that one of the thermal flux. In this discussion is reported an analysis of the bidimensional and tridimensional temperature maps to better understand the thermal response of the receiver as the target of the solar radiation reflected from the parabolic dish. As for the power distribution, even in this case the focal plan temperature distribution is heterogeneous and characterized by a large dispersion of the points. The explanation is always the same: the concentrator is not a perfect reflector and it is affected by the limb darkening phenomenon. The maximum temperature value achieved in the center of the focal plane is around 3800 K (Figure 67).

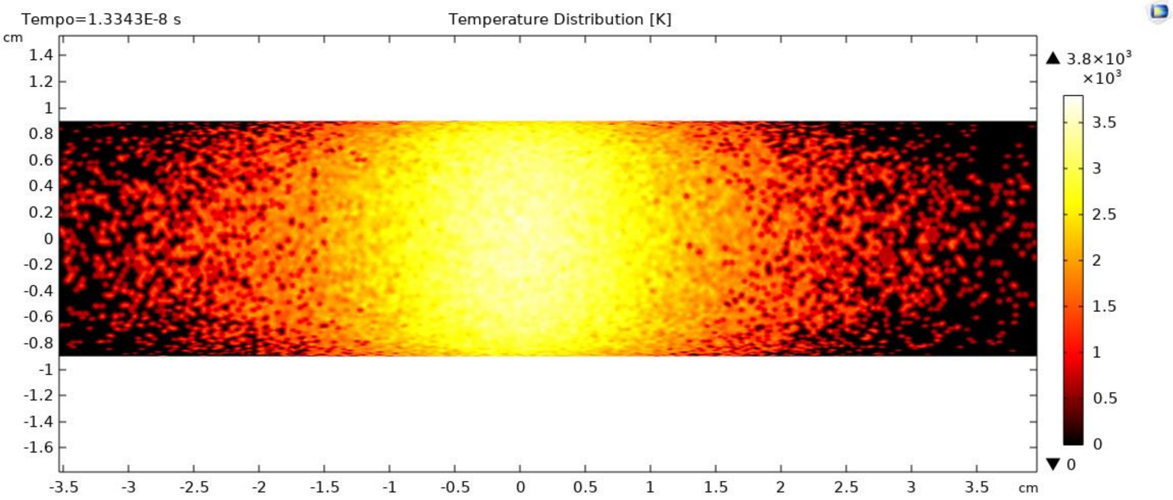

*Figure 67 | 2D temperature distribution in the focal plane.*

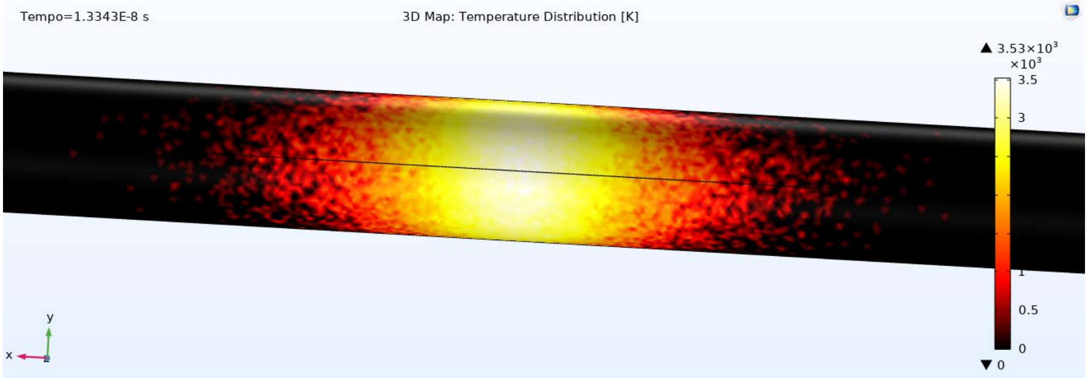

*Figure 68 | 3D temperature distribution in the focal plane.*

The results seen in this section were obtained through the ray-tracing simulation. They allow us to understand in broad terms all the effects of the optical phenomena that affect the concentration of solar radiation. At the same time, the simulation has some limitations. First, the evaluation of the principal parameters is performed in a limited area of the receiver (the central part). For the rest of the receiver, both temperature and heat flux are evaluated as equal to zero. Moreover, with the ray-tracing simulation, a lot of effects that will reduce the reactor temperature are not taken into consideration. In this context is necessary to implement another study that will better simulate the thermal field of the receiver.

Here are reported the logical steps performed for the realization of the bidimensional model that will more realistically predict the temperature in all the receiver surface:

1) The ray-tracing model is used for the evaluation of the average heat flux:

   Results > Derived Values > Average on surface

   The considered surface is not all the receiver absorbing surface but only a little portion of that, precisely the central one.

2) 2D geometrical modelling of the receiver: the concentration surface is approximated with a circular form of diameter $d_{fp} = 0.01\ m$.

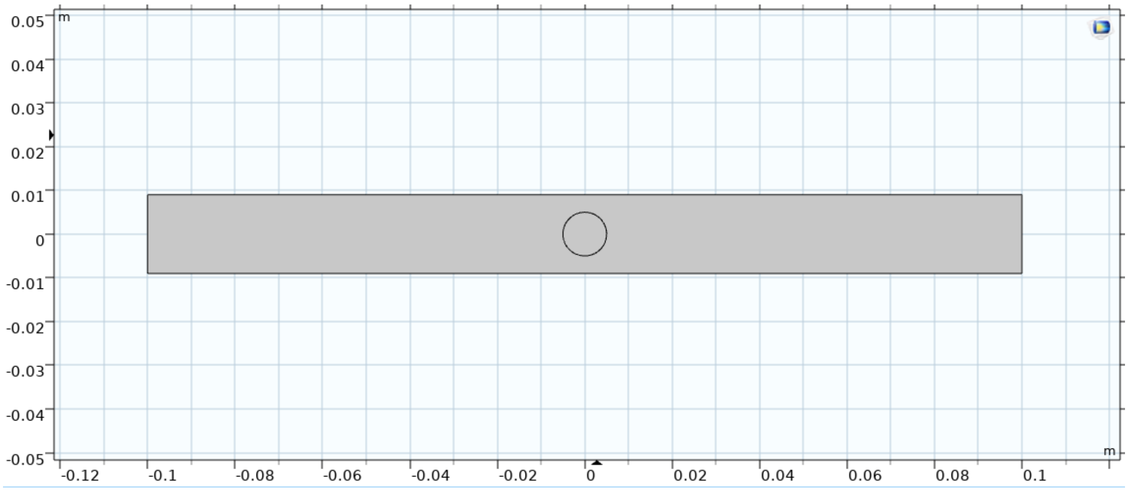

*Figure 69 | 2D geometrical modelling of the receiver.*

3) Simulation of a stationary study for the physics "Heat transfer in solid" with the following conditions:
    1. Receiver initial temperature: T=293.15 K
    2. The average heat flux calculated in 1) is imposed for the concentration surface calculated in 2). The heat source applied in the concentration surface is evaluated as:

$$\mathbf{P[W] = \phi_{avg} \cdot A_{concentration}} \tag{4.4}$$

    3. Convective thermal flux coming out from the receiver external edges.

The result of the heat transfer simulation is shown in Figure 70. Considering an input solar radiation of 800 W/m$^2$, the maximum obtained temperature in the focus is near 1800 °C, which is the value declared by the manufacturer [52] in the case of maximum irradiance available. Having this information is possible to use as a first validation of the model. The temperature values obtained with the ray-tracing simulation (Figure 67) are higher because the model neglect the reactor interaction with the external atmosphere: in a real context, the natural convection with external air and the consequent heat dissipation cause a considerable reduction of the reactor temperature.

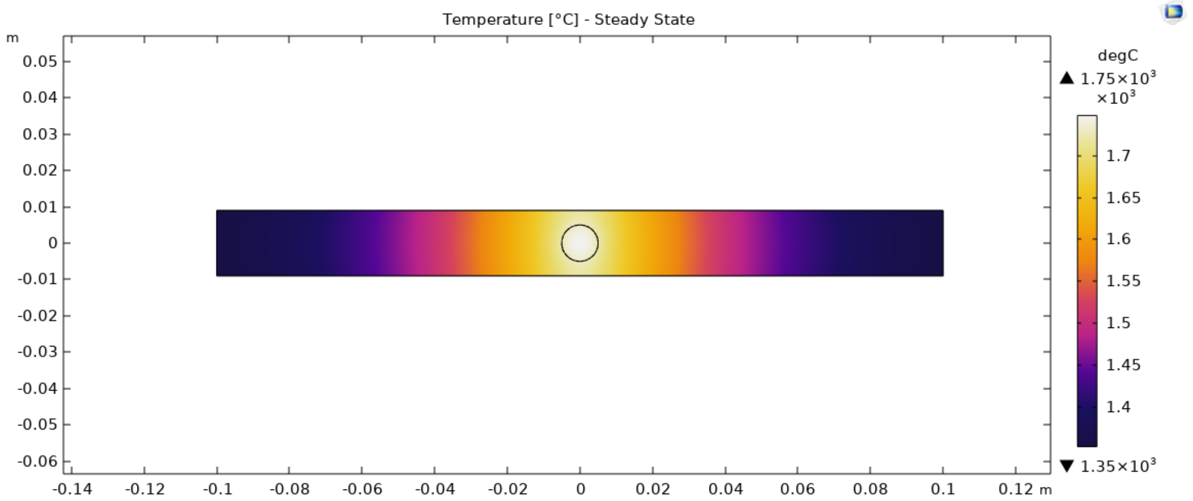

*Figure 70 | 2D temperature map of the receiver considering the exposure to the external atmosphere and the consequent heat dissipation through convection.*

Being that the experimental activity started in December 2020, we have available the reactor temperature values recorded from the thermocouples during the winter period in addition to the global radiation values recorded from the pyranometer located on the rooftop of the Energy Center. In this context, we can use them for a second validation of the model developed so far. For a value of global radiation of around 300 W/m$^2$, the reactor temperature value recorded is around 200 - 250 °C. However, if we give 300 W/m$^2$ as an input of the ray-tracing model and then we proceed with the 2D heat transfer model as we have explained before, we get as result the 2D reactor temperature distribution shown in Figure 71.

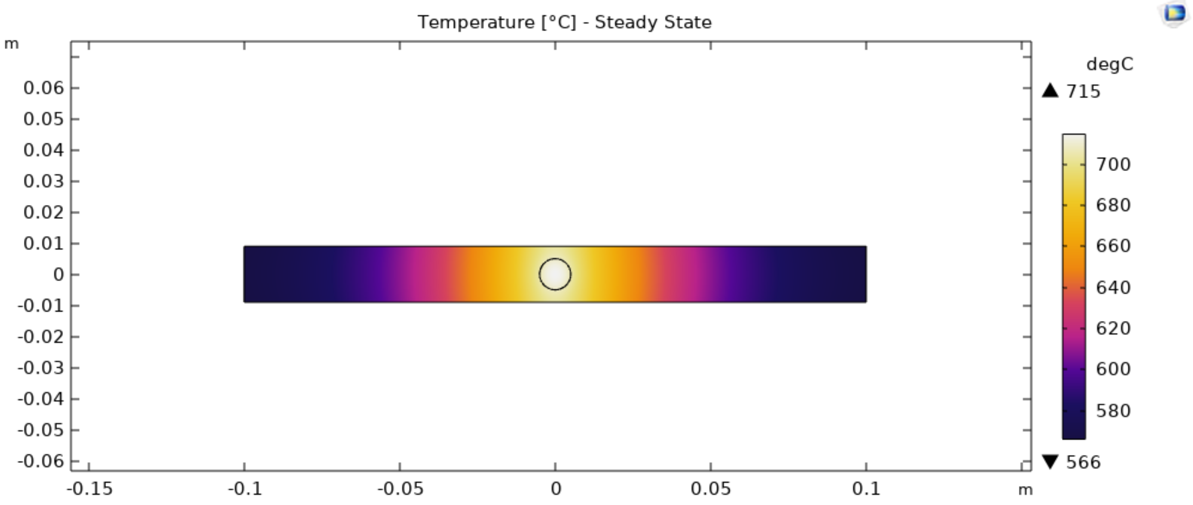

*Figure 71 | 2D reactor temperature distribution in the case of 300 W/m$^2$ of global radiation.*

700 °C is not even close to the temperature recorded from the thermocouples. This means that the model, as it was developed, is not realistic. The main reason can be the fact that the alumina reactor of the Energy Center is surrounded by an iron alloy structure, as can be seen in Figure 43. The iron alloy will certainly contribute to dissipating more heat, reducing the reactor temperature. If we modify the

geometry of the 2D model considering the additional structure, we obtain what is shown in the figure below.

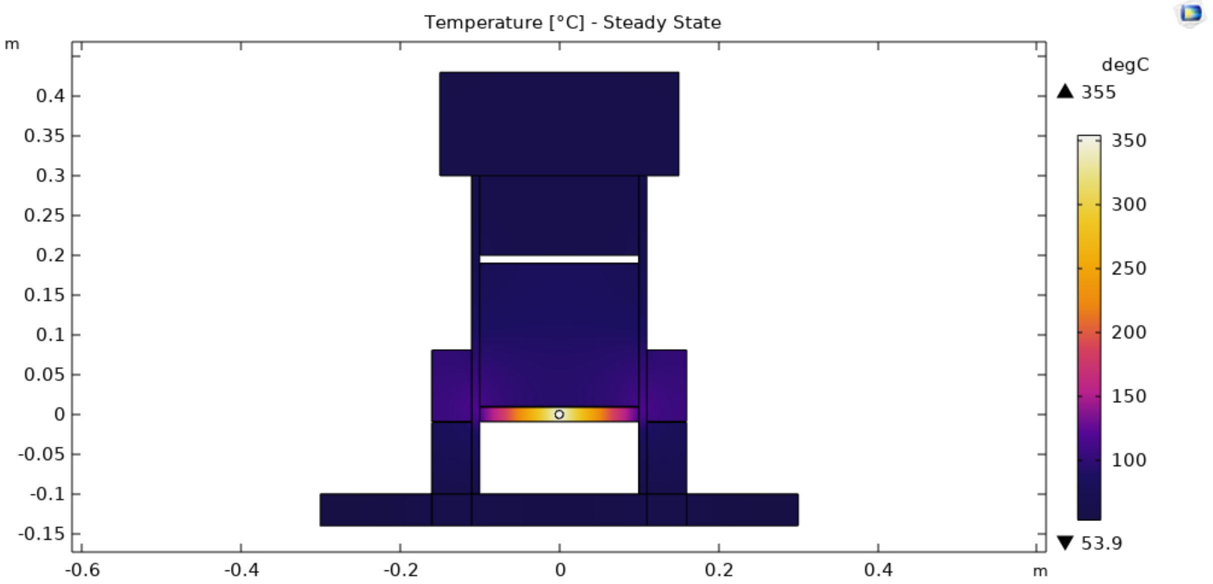

*Figure 72 | Reactor temperature distribution for the 2D model considering the iron alloy structure.*

The temperature decreased and now is closer to the recorded value obtained from the experimental analysis (even if it is still a bit higher). For that reason, we can consider this modified model as more realistic. In this context, if we perform a simulation considering the ideal radiative flux of 800 W/m$^2$, the model gives as output a maximum temperature in the focal point of around 850 °C (obviously 1800 °C are no longer reachable). Moreover, it has to be considered that in reality, this value can be even lower, considering that the temperature obtained with the model is a bit higher than that one obtained from the experimental analysis (referring to 300 W/m$^2$). If the objective is to perform chemical looping processes in the plant of the EC-Lab, the reactor thus structured cannot be good because of the low temperatures achievable. Under 1000 °C would never be possible to perform a thermal reduction. Moreover, an assisted reduction can be performed, but only during summer periods when is possible to reach high values of global radiation. In this framework, the realization of such a process during an entire solar year would be limited and with a low associated yield.

We can conclude that the iron alloy structure must be removed shortly if we want to achieve reasonable temperatures. At this point, the objective is to evaluate the feasibility to perform chemical looping processes in the new hypothetical system without the surrounding complex. Because of that in the following simulation we are going to use the ray-tracing model associated with the first 2D heat transfer model validated with the condition of 800 W/m$^2$→ 1800 °C.

### 4.1.4 Discussion

Having defined the simulation model for the concentrator-receiver system under investigation at the Energy Center Lab, it is possible to focus on the study of the behaviour of the system when it is forced to work under real conditions of variable global radiation both on days and seasons. In this context, a new simulation was implemented to evaluate the possibility to perform chemical looping processes for the different meteorological seasons, by exploiting the temperature distributions obtained as output. The seasonal results comparison seems to be reasonable thanks to the seasons' repeatability over years for the different locations of the globe.

First, we proceed with the evaluation of the global radiation trend over daily time for every weather season. The values of the global radiation for every single day of the year are recorded from the pyranometer located on the rooftop of the Energy Center. In this specific analysis are used the values recorded during the year 2019. For each curve, the radiation punctual values are obtained as results of the average between values associated with the central day of each month of the season under investigation in case of a sunny day. If the central day does not offer the best values in terms of global radiations, we move to near days until we found the best values possible. Chosen the three days for each season, we proceed with the evaluation of the average value, obtaining the seasonal global radiation distributions shown in Figure 73.

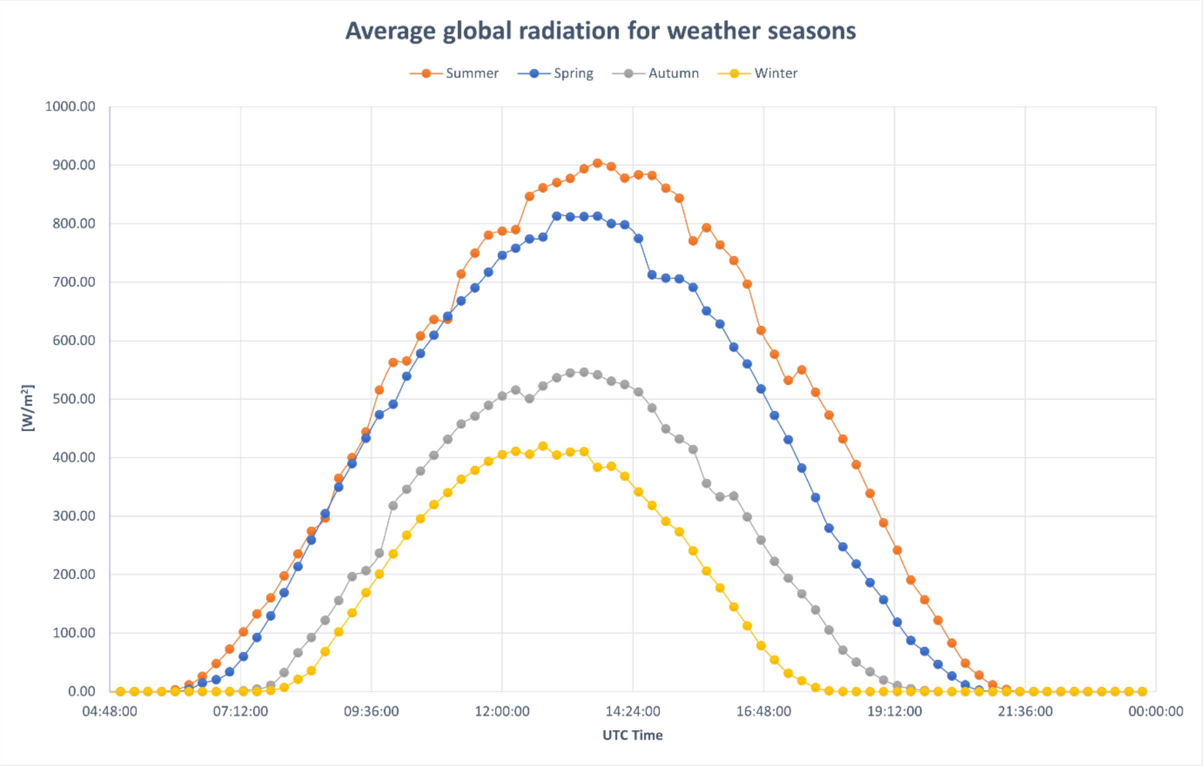

*Figure 73 | Average global radiation for weather seasons.*

It is visible that during the spring and summer seasons the radiation can reach very high values. Moreover, is also important to consider that the period for which we have consistent radiation is much more extended concerning colder seasons. It easy to deduce that in this framework the energy absorbed from the concentrator can be high, resulting in a higher yield of the plant.

The global radiation trends obtained above are now given as input to the simulation model for the assessment of the reactor temperature. Since we are considering the "future" reactor not surrounded by the steel structure, we do not have experimental temperature data not even for the winter case. Because of that, there is a need for the model to be applied for all the meteorological seasons. The average global radiation values are imported in COMSOL for the ray-tracing simulation thanks to the "parametric sweep" function. For each radiation, the value is then calculated the average heat flux on the central part of the receiver surface, which is then given as input of the 2D heat transfer model of the reactor without the steel complex around it. The temperature trends obtained for each weather season are reported in Figure 74.

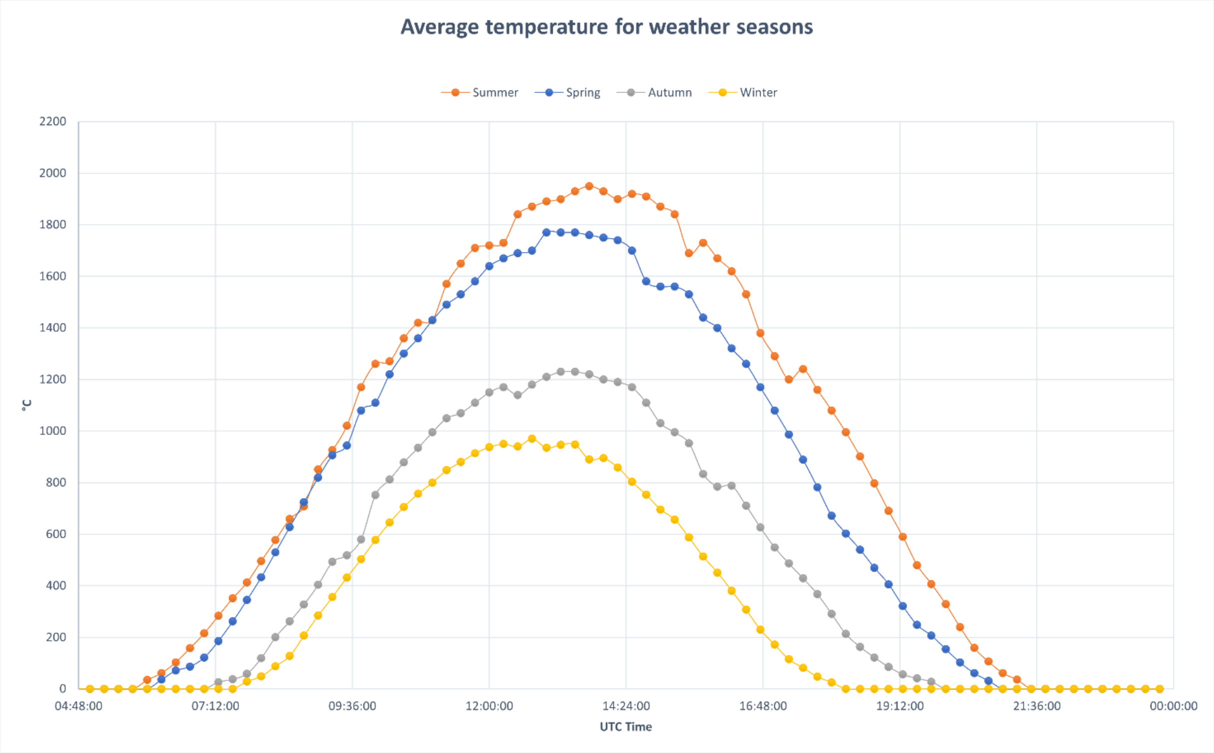

*Figure 74 | Average temperature for weather seasons.*

These are the temperature trends over daily time for every single season that we are expecting to have in the Energy Center reactor if we remove the construction around it. The values are much higher compared to what we can achieve with the actual reactor. In these conditions, the system is better suited to the implementation of chemical looping processes. Now a thermal reduction can be surely performed during both summer and spring and maybe also during autumn in some cases. In contrast, the lower temperatures make the winter season not suitable for this kind of chemical reaction. As an alternative is possible to perform an assisted reduction, with $CH_4$ or $H_2$ as reducing gases, which does not require very high temperatures due to the reducing power of the reactants. The latter can be implemented also during all the other seasons.

# 5 EXPERIMENTAL RESULTS

This chapter is dedicated to experimental results obtained from tests performed at the $CO_2$ Circle Lab in Environment Park. These tests are based on chemical looping processes for $CO_2$ conversion.

The objective is to find the optimal one for each group of tests in terms of yield, after having studied the response of the process at different oxidation temperatures, $CO_2$ concentrations and reduction conditions. Is possible then to consider the opportunity to translate these ideal tests in real-world condition, such as the CSP system on the rooftop of the Energy Center, modelled as explained in chapter 4.

## 5.1 Experimental sessions

An electrically heated tubular furnace is utilized to simulate a real solar thermochemical reactor. It is equipped with a temperature control system, a gas feed-in system integrated with MFCs and a gas analyzer. The system layout and the procedure applied for the preparation and control of tests are explained in detail in section 3.2.

Two different test groups are executed, each of them with a different reactor configuration:

1. CL with the $H_2$ assisted reduction in the alumina boat;
2. CL with the thermal reduction in the alumina tube.

The total flow rate into the reactor during the reduction and oxidation is kept constant at 200 Nml/min. A 200 mg amount of iron oxides powder is used for all the experiments as OC. This is the same as that one used by Azharuddin E Farooqui et al. [36] in their study. For the oxygen carrier synthesis refer to the above paper. For the filling process of both reactors instead refer again to section 3.2.

Considering a CL with $CO_2$ splitting, the $Fe_3O_4$/FeO redox state is the only possible: for the slow kinetic is not possible to reach the highest state of oxidation ($Fe_2O_3$) [36]. The selection of the correct inert OC support is important since FeO could react with this, leading to a deactivation of the sample: $Al_2O_3$ is one of the best supports, with a high melting point and chemical stability. However, it is important to highlight that at high temperatures, wüstite and alumina support may still react, forming $FeAl_2O_4$, deactivating the OC. The addition of magnesium (Mg) to alumina, which forms $MgAl_2O_4$-spinel, avoids the formation of Fe-Al spinel.

### 5.1.1 Session 1

The first test group, performed in the alumina boat, is based on the execution of five subsequent cycles. For each cycle, initially, the test sample is reduced with 5% $H_2$ with $N_2$ for 30 min to ensure complete reduction. The reduction and oxidation temperature will be the same: an isothermal test with no temperature ramps between the two steps. After the reduction, there is the purging of nitrogen for 10 min to ensure that there is no $H_2$ in the test environment. At this point is performed the oxidation reaction of the sample with 20 and 40% $CO_2$ with $N_2$ for 15 min. Four different temperatures are analyzed, included 700, 800, 900 and 1000 °C. Lastly, there is another purging of nitrogen for 10 min to prepare the sample to face another cycle.

### 5.1.2 Session 2

The second test group is instead performed in the alumina tube. In this case, the CL process is composed of four subsequent cycles. For each cycle, initially, the test sample is thermally reduced at 1350 °C with 100% $N_2$ for 30 min to ensure complete reduction. Then a ramp down is performed to reach the oxidation temperature and here the sample stays in isothermal condition for 10 min (always with 100% $N_2$). At this point is performed the oxidation reaction of the sample with 20, 25 and 30% $CO_2$ with $N_2$ for 15 min. Three different oxidation temperatures are analyzed, included 800, 850 and 900 °C. Finally, there is a ramp-up again until 1350 °C with 100% $N_2$ to prepare the sample to face another cycle.

| | SESSION 1 | SESSION 2 |
|---|---|---|
| *Reactor* | Alumina Boat | Alumina Tube |
| *Reduction type* | Assisted reduction | Thermal reduction |
| *Gases used during reduction* | 5% $H_2$ with $N_2$ | 100% $N_2$ |
| *Reduction temperature* | 700, 800, 900 and 1000 °C | 1350 °C |
| *Gases used during oxidation* | 20 and 40% $CO_2$ with $N_2$ | 20, 25 and 30% $CO_2$ with $N_2$ |
| *Oxidation temperature* | 700, 800, 900 and 1000 °C | 800, 850 and 900 °C |

*Table 4 | Main test conditions for both experimental sessions.*

The process yield, explicated in CO specific production rates output (μmol/g/s) for both sessions, is determined by the following equation:

$$\mathbf{\dot{\omega}_{CO} = \frac{x_{CO,out} \cdot \dot{n}_{ox,in}}{M_{OC}}} \qquad 5.1$$

Where:

- $\mathbf{x_{CO,out}}$ : CO mole fraction;
- $\mathbf{\dot{n}_{ox,in}}$ : molar inflow rate of the gas mixture during the oxidation step;
- $\mathbf{M_{OC}}$ : sample mass.

Both test groups settings have been decided to take a cue from Azharuddin E Farooqui et al. paper [36] to have a kind of guide as well as a term of comparison.

## 5.2 Results and discussion

The results for both experimental sessions illustrate the $CO_2$ dissociation reactivity in terms of CO production rates (µmol/g/s) and total specific CO production (mol/g) for different $CO_2$ feed concentrations and temperatures.

Moreover, at the end of this chapter, are also reported microstructural results obtained with the X-ray diffraction (XRD) analysis of the fresh sample.

### 5.2.1 Results for session 1

Considering tests in $H_2$ assisted reduction, we show in Figure 75, as a representative example, the CO production rate as a function of oxidation time for five subsequent isothermal cycles. The CO is produced during the $CO_2$ dissociation over the iron oxides powder. The specific case that we are going to analyze is the process at 1000 °C with 40% $CO_2$ during oxidation.

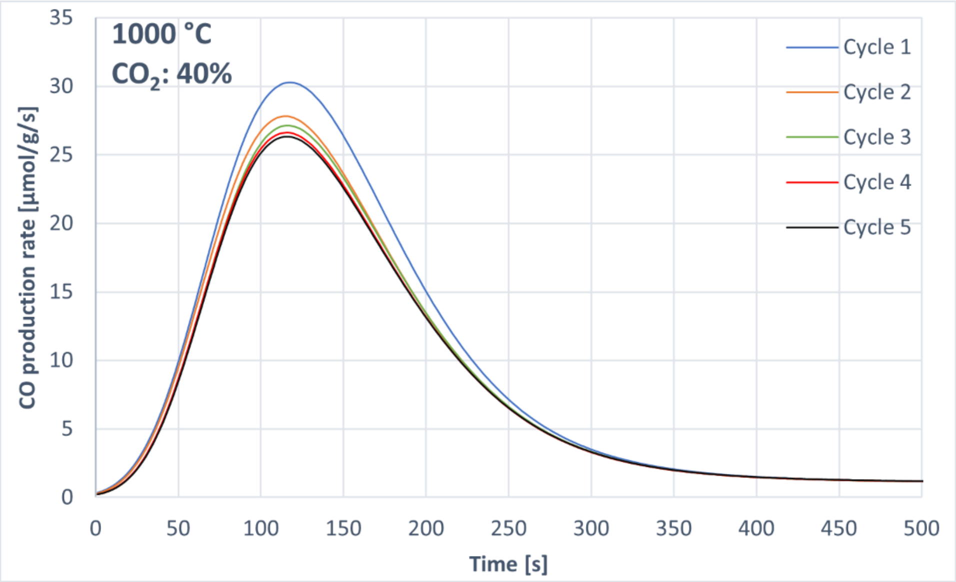

*Figure 75 | CO production rate for 1000 °C and $CO_2$:40% for five cycles.*

Between the first and the second cycle, there is only a 10% decrease in maximum production. This decrease dissipates moving forward with the cycles. As regards the other cases, the trend of CO peak production rates along the cycles is similar. The only difference is that the decrease percentage can be different, but still within 10%.

Besides the CO production rate, we can also analyze the total CO production in mol/g of oxygen carrier for the five cycles. This time we are going to show the plots obtained for every single test developed in the present study: different temperatures and $CO_2$ concentrations are analyzed, as explained in section 5.1.1 (Figure 76).

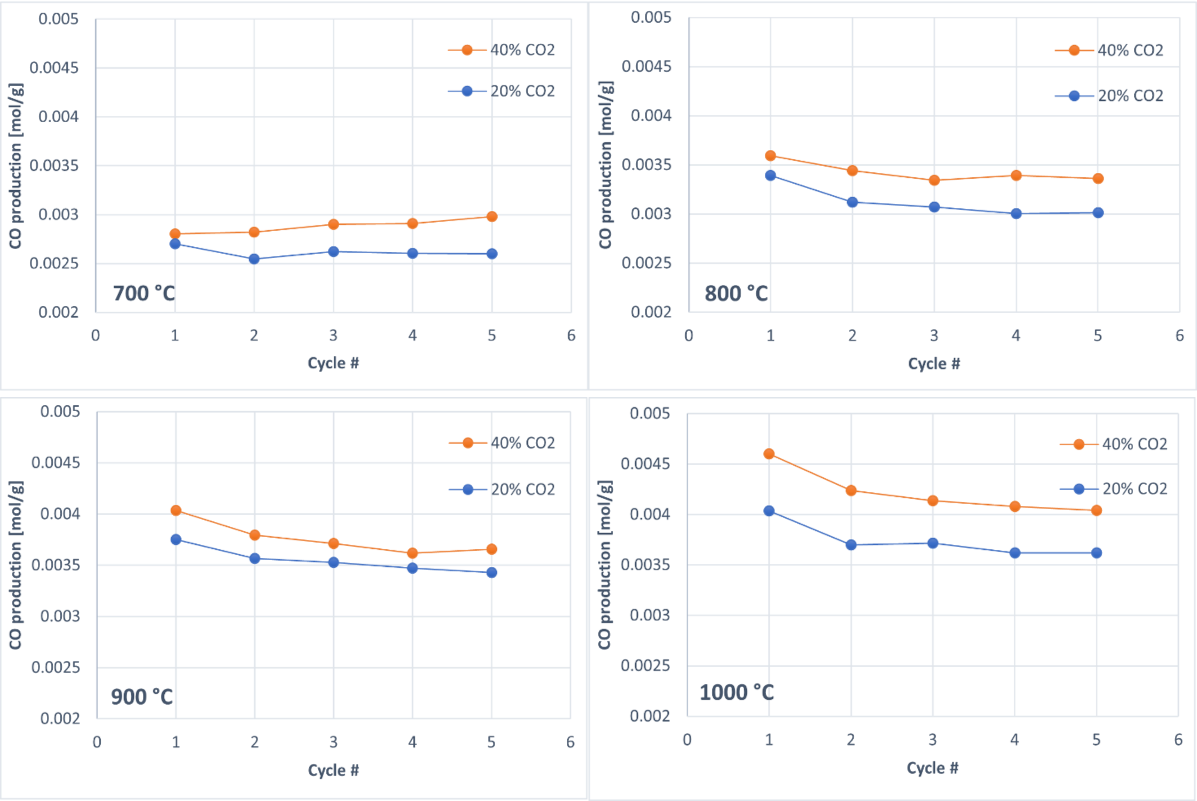

*Figure 76 | Specific CO production for different temperatures and $CO_2$ concentrations over cycles.*

For each temperature and $CO_2$ concentration, the CO production becomes stable after the third cycle. In this context, it makes sense to deduce that, if we extend the number of cycles for each test, we will obtain an almost constant CO production. Keeping the temperature steady and varying the $CO_2$ concentration, and vice versa is noticeable that the produced CO moles per sample gram increase as both $CO_2$ concentration and temperature increase.

From now on, we will no longer analyze quantities associated with different chemical looping cycles. Conversely, the following results have been obtained as an average over the five cycles of the respective quantities for every single test.

Figure 77 shows the CO production rate as a function of oxidation time for the temperature range of 700 - 1000 °C and different $CO_2$ feed concentrations. The oxidation lasts around 400 s and CO production rates peaked between 130 and 150 s: the peak is located within the first half of the oxidation phase. This is connected to the fact that the $CO_2$ splitting rate is fast at the beginning due to the larger number of oxygen vacancies [36]. Later CO production rate decreases after reaching the peak as the remaining oxygen vacancies in the sample are filled. Both temperature and reactants concentration in the oxidation step affect the values of CO peak production rates: the kinetics of the reaction is favoured when both above-mentioned parameters increase and this condition leads to a higher CO peak, together with a narrower curve. Besides the kinetics, also the carbon deposition increases with temperature and $CO_2$ concentration [41], but it passes into the background to the conditions under which we are operating, otherwise this would have been manifested in a collapse of the performances and therefore in a reduction of the peak at a certain temperature and reactants concentration.

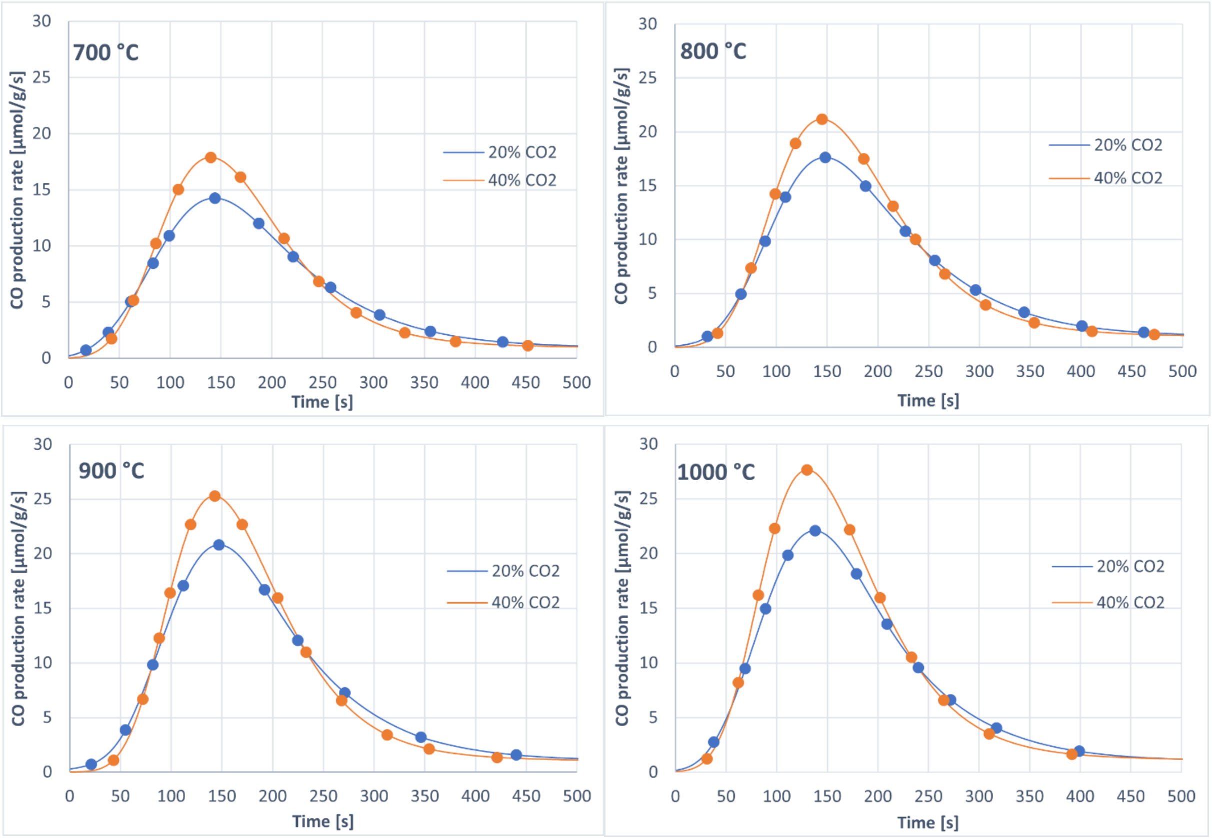

*Figure 77 | CO production rate during the oxidation step at different temperatures and $CO_2$ concentrations.*

The area underneath every single curve in the figure above represents the total CO production obtained from the oxidation phase of one CL cycle in respective conditions of temperature and $CO_2$ concentration. Figure 78 reports the value in mol/g with varying temperatures (a) and (b) $CO_2$ concentrations. Lower the reduction temperature, lower the number of oxygen vacancies created in the sample, lower the CO production during the oxidation step [36]. The CO production shows a gradual increase profile from 700 to 1000 °C and from 20% to 40% $CO_2$. Similar behaviour can be seen in the CO peak production rate: it is illustrated in Figure 78 c) and d). The increase of CO peak production rates is larger for higher $CO_2$ concentrations. From total CO production and CO peak rate, it can be seen that the influence of $CO_2$ concentration and oxidation temperature are equally important almost for all temperatures. The only difference can be seen at high temperatures, where the carbon dioxide concentration influence in CO production barely exceeds that one of temperature. In this context, it makes sense to evaluate the possibility to perform an isothermal CL at 1000 °C only in the specific case of oxidation with 40% $CO_2$. This because, for 20% $CO_2$, the increment in total CO production from 900 to 1000 °C is only 5% while, considering 40% $CO_2$, the percentage rises to 12%.

In conclusion, for this test session with $H_2$ assisted reduction, the best test in terms of process yield is precisely that one developed at 1000 °C with 40% $CO_2$ with $N_2$ during the oxidation step. For this specific case, we reach the maximum of both quantities reported in the figure below:

- Total CO production: 0.00422 mol/g;
- CO peak production rate: 27.6 µmol/g/s.

Remember that these values are obtained as an average over the five cycles for every single test.

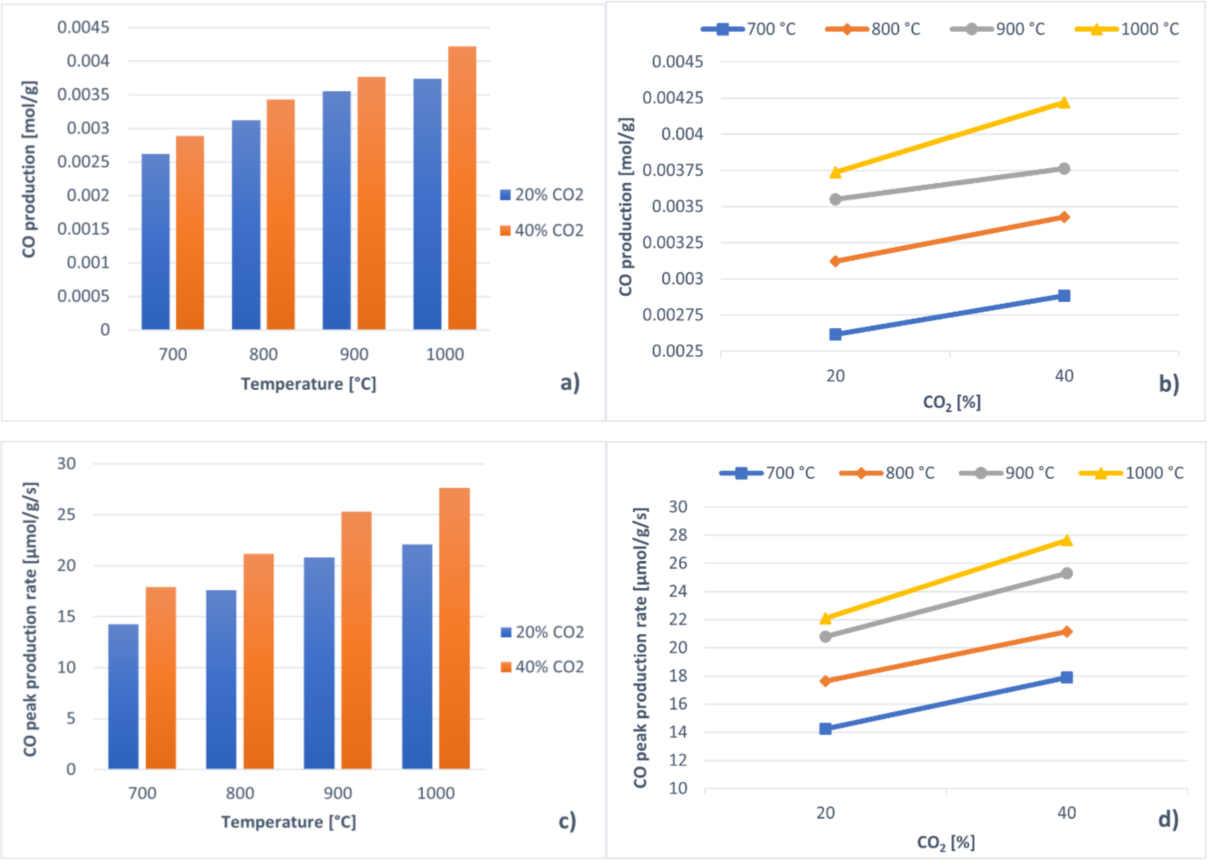

*Figure 78 | Total specific CO production with varying a) temperature and b) $CO_2$ concentration; CO peak production rates with varying c) temperature and d) $CO_2$ concentration.*

### 5.2.2 Results for session 2

Moving to the second group of tests, for which is performed a thermal reduction at a high temperature, we show in Figure 79 CO production rate trends as a function of oxidation time for four successive cycles for the specific case of 30% $CO_2$ and oxidation temperature of 800 °C. This case is representative of all other cases.

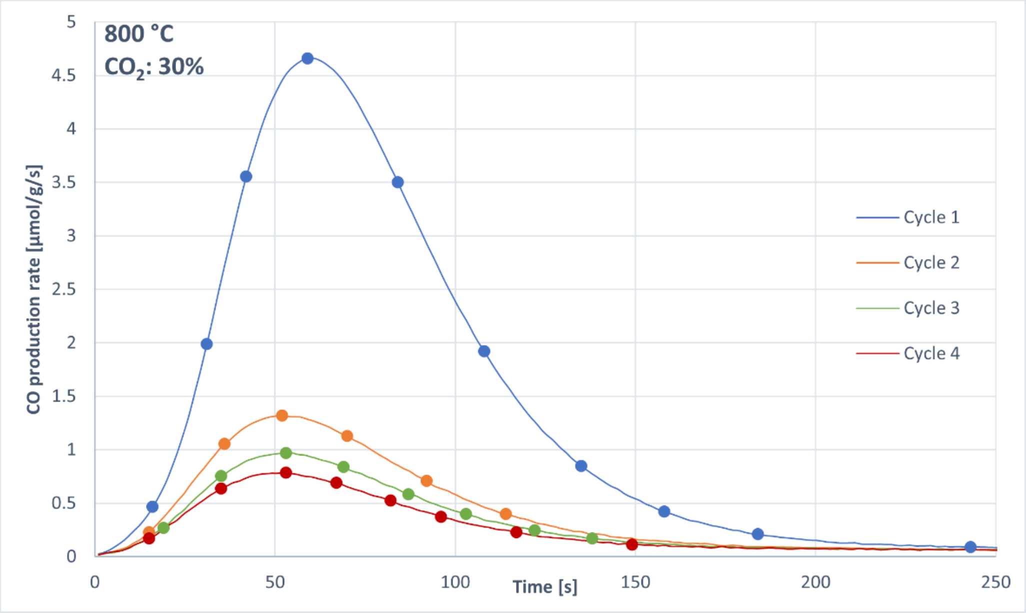

*Figure 79 | Case 30% $CO_2$ and 800 °C: CO production rate trends as a function of oxidation time for four subsequent cycles.*

What is immediately evident is the collapse of the performance after the first cycle. The carbon deposition, linked to the presence of CO and $CO_2$ in the reaction environment, can be considered as the principal cause: C deposition reduces the reduction efficiency and, consequently, the CO production rates as well as the total specific CO production (Figure 80). The possible presence of this phenomenon can be confirmed from the literature [36] and by visual analysis of the sample at the end of the test: the red powder that was at the beginning shows itself as black. In comparison, results obtained during tests of CL with $H_2$ assisted reduction show a CO peak production rate reduction through the cycles less accentuated, if not almost imperceptible. It has to be considered that in this last case the carbon deposition is less impactful being that, reducing with $H_2$, the reduction extent is higher and there are different reactions involving the C conversion ($H_2$ "cleans up" the test environment). In addition, with a thermal reduction, we work at higher temperatures (1350 °C) which certainly contribute to the accentuation of the phenomenon. For what concern precisely the comparison between the values of CO peak production rates and total specific CO productions for the two test groups, is reasonable that, for the same reason explained above, in this case, we obtain lower values. Moreover, for further confirmation of the credibility of the results, performing a TGA test with the same OC and thermal reduction condition, we have obtained, referring only to the first cycle, the same value of mass variation (oxygen released and then regained). This gave us some confidence in the validity of our results.

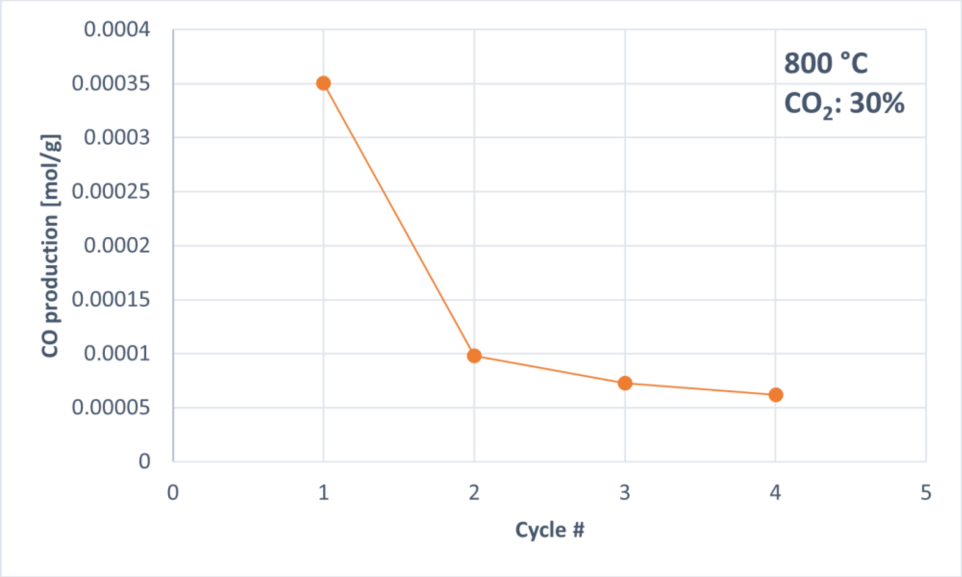

*Figure 80 | Case 30% $CO_2$ and 800 °C: Total specific CO production for four subsequent cycles.*

To further investigate for another possible cause connected to the collapse of the performance after the first cycle, we have replicated the same test but using the alumina boat instead of the tube. The objective was to see if the quartz wool used in the alumina tube might be responsible for the accentuation of the consequences associated with C deposition: at the end of the test, the sample and the quartz wool appear as a single charred compact block and this might have reduced the availability of free vacancies for the oxidation of the sample. What we obtain with the alumina boat (for which no quartz wool is needed) is still a drastic reduction of the CO peak rate production after the first cycle and this can therefore exonerate the quartz wool as one possible cause of the phenomenon.

We understand that, if we want reasonable results, we must seek only the first cycle. In the figure below are reported CO production rates, as a function of oxidation time, associated with the first cycle of the set of tests imposed at the beginning. It is visible that most of the test data are missing: we have considered valid only a few of them.

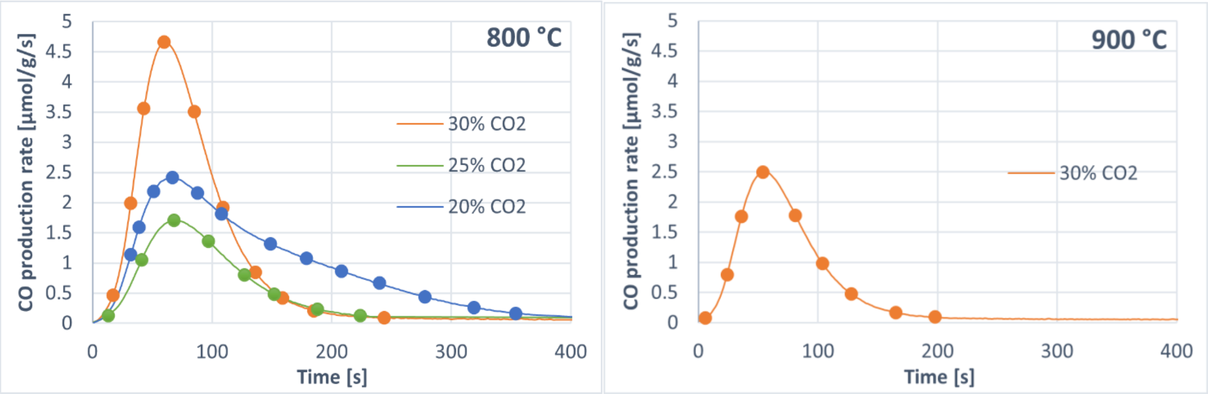

*Figure 81 | CO production rate trends as a function of oxidation time obtained during the first cycle.*

At the beginning of the experimental activity, the set of temperatures and $CO_2$ concentrations should have been the same for both test groups. During the work with thermal reduction CL, we have decided to exchange 1000 °C with 850 °C and 40% with 25% $CO_2$. For what concerns the temperature, would not make sense to analyze 1000 °C, since already at 900 °C there is a reduction in terms of performances. The oxidation with 40% $CO_2$ has been tested for the case at 800 °C at least two occasions, but both times we obtain drastic CO peak production rate collapse. Since both temperature and $CO_2$ concentration increase would increase carbon deposition and considering that with this group of tests we have a less efficient reduction, makes sense that we reach a gradual deactivation of the sample, associated with a lower peak and total CO production, at a lower temperature and $CO_2$ concentration concerning the case with $H_2$ assisted reduction.

Now we are going to analyze the tests for which we have encountered problems and which we do not consider valid:

- 30% $CO_2$ at 850 °C: the obtained CO peak production rate was lower than those corresponding to tests with 30% $CO_2$ at 900 °C and 800 °C. What we expect is a cycle yield higher than that one of the case with 30% $CO_2$ at 800 °C or at least between that one of the two above-mentioned tests. After every test, the reactor is emptied and cleaned with compressed air and then is reloaded for a new one. Nevertheless, in the middle of the reactor remains blackish incrustation. We have come to think that this dirty residue may be the cause of the unexpected collapse of the performance. In this framework we have decided to repeat the same test, but this time in a factory-new alumina boat. Before the test, it is heat-treated to remove any factory residue. Nevertheless, we obtained the same result.
- 25% $CO_2$ at 800 °C: as can be seen in Figure 81, the obtained performances are lower than those associated with the oxidation with 20% $CO_2$ at the same temperature. This is not what we expected: the reactant concentration positively affects the kinetics of the reaction and because of that, at higher $CO_2$ concentration, we expected higher CO peak rate production. Moreover, to prevent doubts about reactor cleaning, before the test, in addition to the ordinary cleaning procedure, the reactor was heat-treated for 1 hour at 500 °C with 10% $H_2$ with $N_2$ to remove carbon incrustation.
- 20% $CO_2$ at 900 °C: obtained values for the CO production rate could also be considered meaningful if it wasn’t for the fact that the peak of the first cycle was lower than that one of all subsequent (opposite phenomenon to what we have achieved so far). Even in this case, the reactor was heat-treated, but this time for 1 hour at 800 °C with 50% $H_2$ with $N_2$.

Having regard to the succession of negative results, we decided not to analyze the other missing tests.

Concerning tests considered good, is noticeable that the oxidation time is about half of that one of the CL with $H_2$ assisted reduction. This can make sense considering the reduced number of vacancies available because of the worst type of reduction: fewer vacancies will certainly be filled before. CO peak production rates are again located within the first half of the oxidation phase for the same reason explained in section 5.2.1.

We can surely conclude that "wrong" tests are not a consequence of the dirty residue that remains inside the reactor between one test and another. Probably the responsible is to be sought in the set-up of the CL process itself associated with the OC chosen. To better understand the cause of the instability of materials could use post-mortem analysis, as XRD and SEM. Neither will be performed during the experimental activity, but we leave the starting point for future studies.

In conclusion, we can say that is impossible to find the optimal test among the others because this test group, as a whole, is not good to be replicated under real solar radiation conditions:

1. Only the first cycle would give modest results in terms of CO production: we should replace the sample after each cycle. In this way, the sample would not be better exploited.
2. There is no certainty about the replicability of tests, which show themselves as unpredictable and irregular.

### 5.2.3 Microstructural results

The XRD is the tool used for material characterization in terms of microstructural analysis considering the fresh sample. For the detailed technical explanation refer to Azharuddin E Farooqui et al. [36] study. In Figure 82 is shown the XRD pattern of the fresh OC: it is composed of both $MgAl_2O_4$ spinel and hematite ($Fe_2O_3$). For similar diffraction angles, the width of the peaks corresponding to $MgAl_2O_4$ is slightly lower than that of $Fe_2O_3$: this means that the size of $MgAl_2O_4$ is higher.

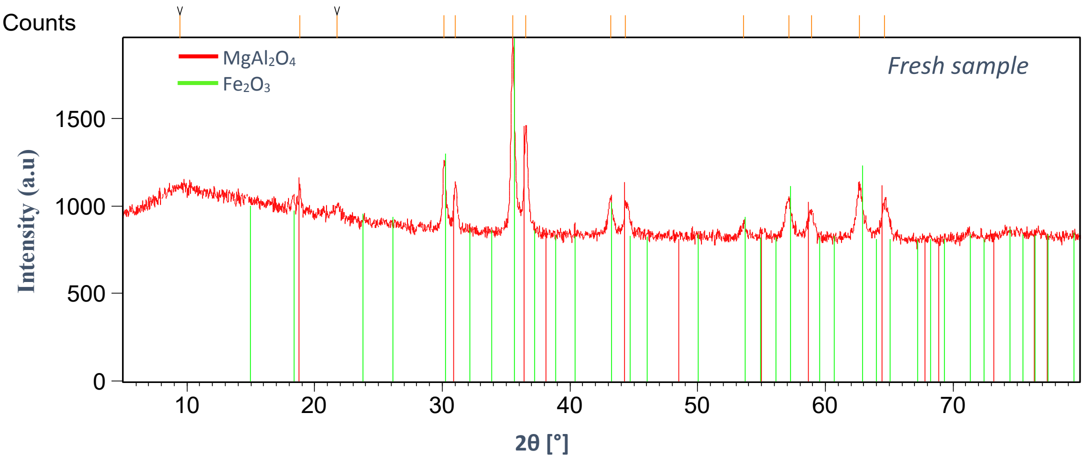

*Figure 82 | XRD pattern of the fresh sample.*

# CONCLUSIONS

As we have already explicated in section 1.1, the objective of this dissertation is to investigate the feasibility to perform chemical looping processes for syngas production in the CSP system located on the rooftop of the Energy Center building. For this purpose, first, has been developed a COMSOL model to predict the temperature evolution of the real reactor for the four seasons (chapter 4). Secondly, different chemical looping processes at different temperatures, $CO_2$ concentrations and reduction conditions were investigated to find the best set-up of the system (chapter 5). These have been carried out at the $CO_2$ Circle Lab in Environment Park using an electrically heated tubular furnace to simulate a real solar thermochemical reactor.

In this last section, we are going to synergically join the two studies, trying to figure out how and when to translate the best test in the reactor of the Energy Center. The objective is to draw reasonable conclusions.

To summarize, from experimental results obtained at the $CO_2$ Circle Lab, we have concluded that:

1. For CL with $H_2$ assisted reduction, the best test in terms of process yield seems to be that one based on the isothermal CL at 1000 °C and oxidation with 40% $CO_2$ with $N_2$;
2. For CL with thermal reduction, is impossible to find the optimal test among the others because this test group is unpredictable and irregular.

Moreover, is important to highlight that during the above-mentioned test is not produced syngas, but only CO. This, in a second moment, can be mixed with $H_2$ with a controlled $H_2$/CO ratio [4].

For what concerns the CSP system, the reactor's inner diameter is 14 mm. On the other hand, that one of the $CO_2$ Circle Lab reactor is just over half (8 mm). This condition leads us to think that 0.2 g of iron oxides powder cannot be sufficient for the EC solar thermochemical reactor. For the estimation of the OC mass quantity, we refer to Francesco Orsini master's degree thesis [54], who has performed his analysis in the same kind of reactor and using hematite as a catalyst:

$$\mathbf{V_{porous} = \pi \cdot \frac{D_{int}^2}{4} \cdot L = 3233\ mm^3} \tag{6.1}$$

$$\mathbf{V_{Fe_2O_3} = (1 - \phi) \cdot\ V_{porous} = 1681\ mm^3} \tag{6.2}$$

$$\mathbf{m_{OC} = \rho_{Fe_2O_3} \cdot V_{Fe_2O_3} = 8.81\ g} \tag{6.3}$$

Where:

- L is the porous medium length, fixed so that to have an $\mathrm{L/D_{int}}$ ratio of 1.5;
- ϕ is the porosity, set equal to 0.48;

- $\rho_{Fe_2O_3}$ is the hematite density, set equal to 5240 kg/m$^3$.

For the best CCL test, for which are used 0.2 g of OC, surely the effective reduction time was less than 30 min set, but we are not able to establish how much it is. Now is necessary to understand if 30 min is still a sufficient time for the reduction of 8.81 g of iron oxides. It is obvious that in the latter case the total flow rate into the reactor during the reduction and oxidation must be higher than 200 Nml/min. To be more precise and detailed, a kinetic model should be developed to define the exact time needed for the reduction. We will not enter into the merits of this analysis, but we leave the starting point for future studies. In this context, we are going to perform a precautionary extrapolation from the study developed by the same Orsini [54]: a banal proportion between OC mass and time of reduction recorded. It is important to highlight that he has analyzed a thermal reduction at 1600 °C. As a result, we obtain that 28 min is the time needed for the thermal reduction of 8.81 g of OC: in our case, we work at a lower temperature (lower kinetics, more time), but in return we use a reducing gas like hydrogen that enhance the reduction of the metal oxide, increasing the reduction extent. In conclusion, we can still impose 30 min to ensure complete reduction of the OC in the EC reactor. The choice is precautionary: the effective time almost certainly will be lower than 30 min.

Consequently, the test can be replicated inside the EC reactor as it was set for the CCL conditions. Since it is based on an isothermal process, we need a system able to maintain the temperature constant on the real reactor. In this context, the solar tracking system needs to be “rigged” to avoid a temperature increase above the desired one. Tracking out-of-focus can be a solution: it is necessary to intervene manually on the software by varying tilt and azimuth parameters for how long is necessary.

The ideal test can be performed during summer, spring and autumn: in these seasons, reactor temperature of 1000 °C is abundantly achieved. During winter is not possible since the maximum temperature reachable for a sunny day is around 950 °C (additionally only for a limited time). In Figure 83 are reported the average temperature profiles for the three seasons in case of a sunny day, considering the tracking out-of-focus active and so the reactor at a constant temperature of 1000 °C for a certain period. It must be noticed that the original curve is displayed transparently in the background. Remember that the last is the temperature profile that has been foretold if the steel structure around the reactor will be removed.

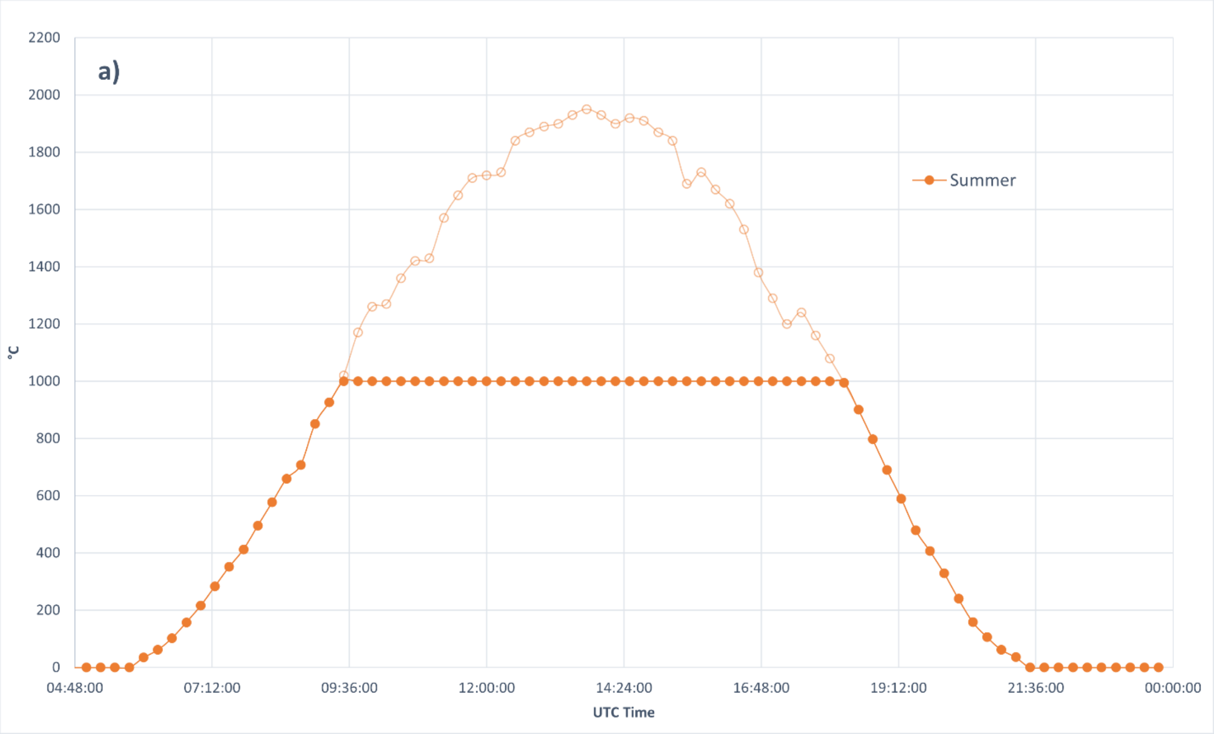
a)
°C
2200
2000
1800
1600
1400
1200
1000
800
600
400
200
0
04:48:00
07:12:00
09:36:00
12:00:00
14:24:00
16:48:00
19:12:00
21:36:00
00:00:00
UTC Time
Summer

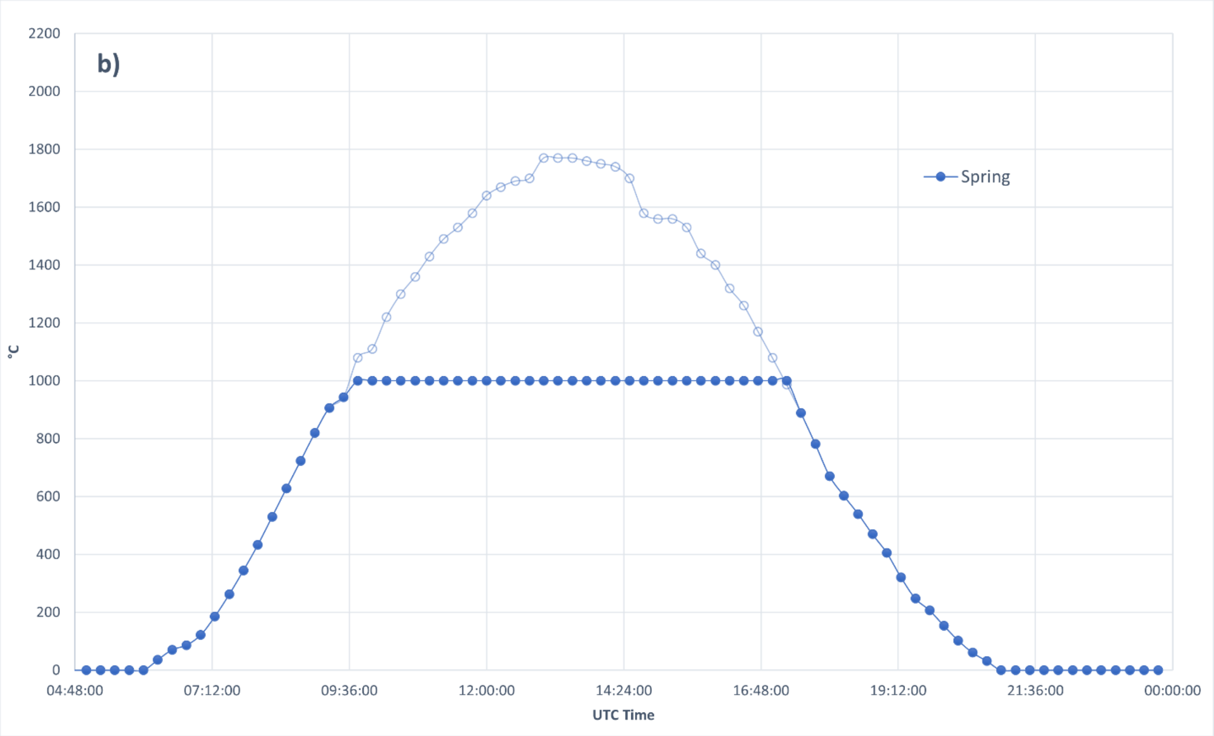
b)
°C
2200
2000
1800
1600
1400
1200
1000
800
600
400
200
0
04:48:00
07:12:00
09:36:00
12:00:00
14:24:00
16:48:00
19:12:00
21:36:00
00:00:00
UTC Time
Spring

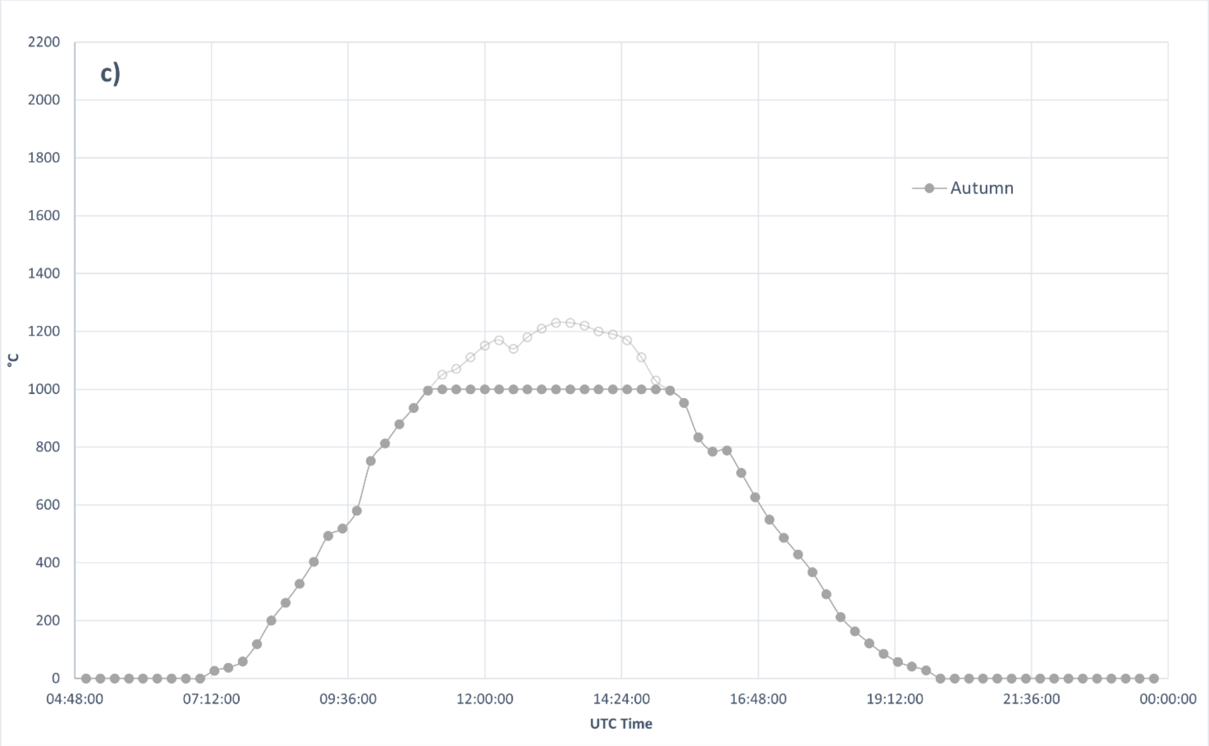

*Figure 83 | Average temperature profiles for a) summer, b) spring and c) autumn considering the tracking out-of-focus active at 1000 °C.*

In Table 5 are summarized some quantitative conclusions derivable from the above graphs. The objective is to evaluate the total CO production in mol/g for a single day for each meteorological season. Is reasonable that higher is the time in isothermal condition, higher will be the number of cycles that can be performed and so the total CO production per day.

| Season | Time in isothermal conditions | Number of complete cycles that can be performed per day | Total CO production per day [mol/g] |
|---|---|---|---|
| *Summer* | 8 h and 45 min | 8 | 0.03376 |
| *Spring* | 7 h and 30 min | 7 | 0.02954 |
| *Autumn* | 4 h and 15 min | 4 | 0.01688 |

*Table 5 | Total CO production per day for summer, spring and autumn.*

As we have already said, the ideal test cannot be replicated for the winter case due to “low” temperature. However, it is possible to consider the idea to translate the best, in terms of process yield considering an entire day, between tests at 700 and 800 °C with 5% $H_2$ in reduction and 40% $CO_2$ in oxidation with $N_2$. For both cases, the process yield will be certainly lower than the ideal test one.

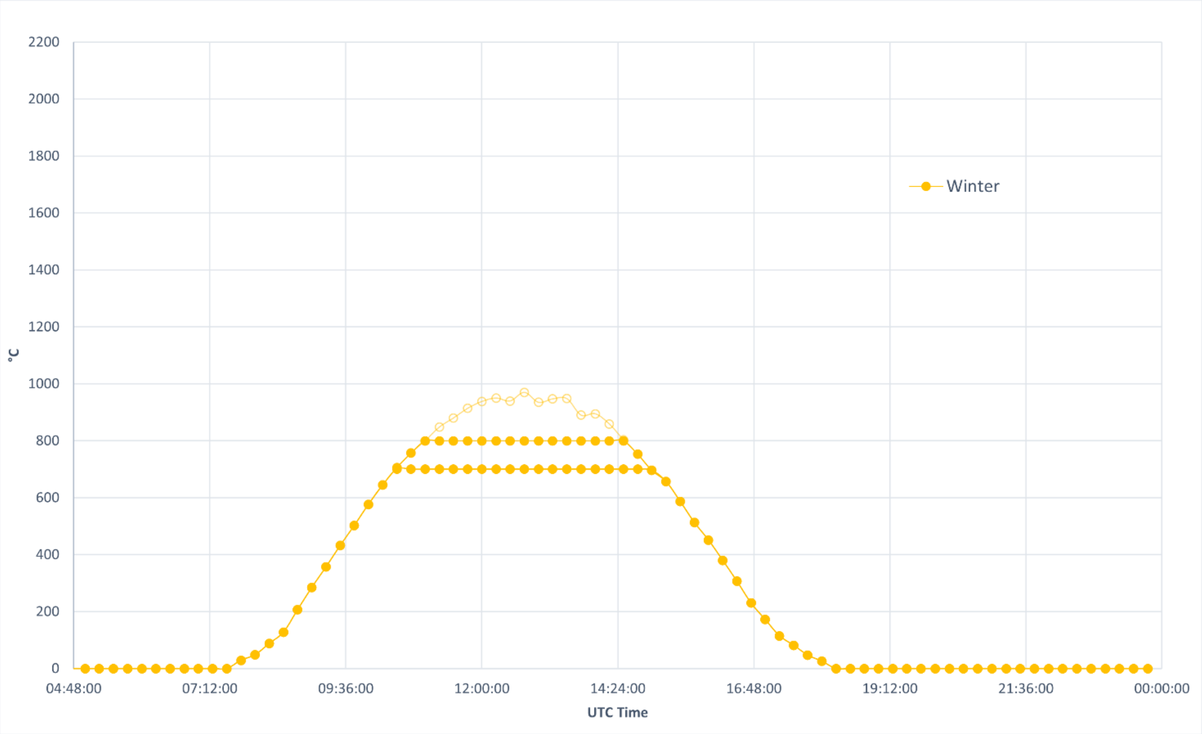

*Figure 84 | Average temperature profile for winter considering the tracking out-of-focus active: two possibilities.*

| Season | Temperature [°C] | Time in isothermal conditions | Number of complete cycles that can be performed per day | Total CO production per day [mol/g] |
|---|---|---|---|---|
| *Winter* | 700 | 4 h and 30 min | 4 | 0.01153 |
| | 800 | 3 h and 30 min | 3 | 0.01028 |

*Table 6 | Total CO production per day for winter.*

Even if the CO produced during a single cycle for the case at 700 °C is lower than that one related to 800 °C, the fact of being able to perform an extra cycle means that the total CO produced at the end of a whole day is greater, making the CL process at 700 °C preferable.

Whether a kinetic model will be developed in future studies, could be obtained the effective time of the reduction, which almost certainly will be lower than 30 min. In this case, a single cycle would last less and consequently in a day a higher number of cycles could be performed, increasing the total CO production (mol/g) per day for all seasons, compared to those reported in Table 5 and Table 6. We will not enter into the merits of this analysis, but we leave the starting point for future studies.

# REFERENCES

[1] U. Nations, "United Nations Sustainable Development Goals," [Online]. Available: https://www.un.org/sustainabledevelopment/climate-change/.

[2] Y. Wang, D. He, H. Chen and D. Wang, "Catalysts in electro-,photo- and photoelectrocataltic CO2 reduction reactions," *Journal of Photochemistry and Photobiology C: Photochemistry Reviews,* vol. 40, pp. 117-149, 2019.

[3] UNFCCC, "The Paris Agreement | UNFCCC," [Online]. Available: https://unfccc.int/process-and-meetings/the-paris-agreement/the-paris-agreement.

[4] A. Haeussler, S. Abanades, A. Julbe, J. Jouannaux and B. Cartoixa, "Two-step CO2 and H2O splitting using perovskite-coated ceria foam for enhanced green fuel production in a porous volumetric solar reactor," *Journal of CO2 Utilization,* vol. 41, pp. 1-9, 2020.

[5] A. E. Farooqui, "Solar fuels via two-step thermochemical redox cycles for power and fuel production," Torino, 2018.

[6] G. L. Bachirou, Y. Shuai, J. Zhang, H. Xing, Y. Yuan and H. Tan, "Syngas production by simultaneous splitting of H2O and CO2 via iron oxide (Fe3O4) redox reactions under high-pressure," *International Journal of Hydrogen Energy,* vol. 41, pp. 19936-19946, 2016.

[7] S. Chuayboon and S. Abanades, "An overview of solar decarbonization processes, reacting oxide materials, and thermochemical reactors for hydrogen and syngas production," *International Journal of Hydrogen Energy,* vol. 45, pp. 25783-25810, 2020.

[8] A. Bayon, A. d. l. Calle, K. K. Ghose, A. Page and R. McNaughton, "Experimental, computational and thermodynamic studies in perovskites metal oxides for thermochemical fuel production: A review," *International Journal of Hydrogen Energy,* vol. 45, pp. 12653-12679, 2020.

[9] P. G. Loutzenhiser, A. Meier and A. Steinfeld, "Review of the Two-Sep H2O/CO2-Splitting Solar Thermochemical Cycle Based on Zn/ZnO Redox Reactions," *Materials,* vol. 3, pp. 4922-4938, 2010.

[10] T. C. Merkel, H. Lin, X. Wei and R. Baker, "Power plant post-combustion carbon dioxide capture: An opportunity for membranes," *Journal of Membrane Science,* vol. 359, pp. 126-139.

[11] D. Y. C. Leung, G. Caramanna and M. M. Maroto-Valer, "An overview of current status of carbon dioxide capture and storage technologies," *Renewable and Sustainable Energy Reviews,* vol. 39, pp. 426-443, 2014.

[12] M. Wang, A. Lawal, P. Stephenson, J. Sidders and C. Ramshaw, "Post-combustion CO2 capture with chemical absorption: A state-of-the-art review," *Chemical Engineering Research and Design,* vol. 89, pp. 1609-1624, 2011.

[13] P. Chiesa, G. Lozza, A. Malandrino, M. Romano and V. Piccolo, "Three-reactors chemical looping process for hydrogen production," *International Journal of Hydrogen Energy,* vol. 33, pp. 2233-2245, 2008.

[14] I. Pfaff and A. Kather, "Comparative thermodynamic analysis and integration issues of CCS steam power plants based on oxy-combustion with cryogenic or membrane based air separation," *Energy Procedia,* vol. 1, pp. 495-502, 2009.

[15] K. Z. House, D. P. Schrag, C. F. Harvey and K. S. Lackner, "Permanent carbon dioxide storage in deep-sea sediments," *Proceedings of the National Academy of Sciences,* vol. 103, pp. 12291-12295, 2006.

[16] Z. Yuan, M. R. Eden and R. Gani, "Toward the Development and Deployment of Large-Scale Carbon Dioxide Capture and Conversion Processes," *Industrial & Engineering Chemistry Research,* vol. 55, pp. 3383-3419, 2016.

[17] B. Wei, "A Novel Solar-Driven System for Two-Step Conversion of CO2 with Ceria-Based Catalyst," Stockholm, 2014.

[18] S. A. Chernyak, A. S. Ivanov, D. N. Stolbov, S. V. Maksimov, K. I. Maslakov, P. A. Chernavskii, Y. A. Pokusaeva, A. E. Koklin, V. I. Bogdan and S. V. Savilov, "Sintered Fe/CNT framework catalysts for CO2 hydrogenation into hydrocarbons," *Carbon,* vol. 168, pp. 475-484, 2020.

[19] C. L. Wang, Z. X. Sun, Y. Zheng and Y. H. Hu, "Recent progress in visible light photocatalytic conversion of carbon dioxide," *Journal of Materials Chemistry A,* vol. 7, pp. 865-887, 2019.

[20] J. Y. Tang, R. T. Guo, W. G. Zhou, C. Y. Huang and W. G. Pan, "Ball-flower like NiO/g-C3N4 heterojunction for efficient visible light photocatalytic CO2 reduction," *Applied Catalyst B: Environmental,* vol. 237, pp. 802-810, 2018.

[21] L. S. Jiang, J. Li, K. Wang, G. K. Zhang, Y. Li and X. Y. Wu, "Low boiling point solvent mediated strategy to synthesize functionalized monolayer carbon nitride for superior photocatalytic hydrogen evolution," *Applied Catalyst B: Environmental,* vol. 260, 2019.

[22] Y. Huang, K. Wang, T. Guo, J. Li, X. Wu and G. Zhang, "Construction of 2D/2D Bi2Se3/g-C3N4 nanocomposite with High interfacial charge separation and photo-heat conversion efficiency for selective photocatalytic CO2 reduction," *Applied Catalysis B: Environmental,* vol. 277, pp. 1-9, 2020.

[23] D. J. Deka, J. Kim, S. Gunduz, M. Ferree, A. C. Co and U. S. Ozkan, "Temperature-induced changes in the synthesis gas composition in a high-temperature H2O and CO2 co-electrolysis system," *Applied Catalysis A: General,* vol. 602, pp. 1-9, 2020.

[24] C. Agrafiotis, M. Roeb and C. Sattler, "A review on solar thermal syngas production via redox pair-based water/carbon dioxide splitting thermochemical cycles," *Renewable and Sustainable Energy Reviews,* vol. 42, pp. 254-285, 2015.

[25] A. J. Traynor and R. J. Jensen, "Direct solar reduction of CO2 to fuel: first prototype results," *Industrial & Engineering Chemistry Research,* vol. 41, no. 8, pp. 1935-1939, 2002.

[26] D. Yadav and R. Banerjee, "A review of solar thermochemical processes," *Renewable and Sustainable Energy Reviews,* vol. 54, pp. 497-532, 2016.

[27] S. Abanades, "Metal Oxides Applied to Thermochemical Water-Splitting for Hydrogen Production Using Concentrated Solar Energy," *ChemEngineering,* pp. 1-28, 2019.

[28] A. Riaz, P. Kreider, F. Kremer, H. Tabassum, J. S. Yeoh, W. Lipiński and A. Lowe, "Electrospun manganese-based perovskites as efficient oxygen exchange redox materials for improved solar thermochemical CO2 splitting," *ACS Applied Energy Materials,* vol. 2, no. 4, pp. 2494-2505, 2019.

[29] Y. Zheng, K. Li, H. Wang, D. Tian, Y. Wang, X. Zhu, Y. Wei, M. Zheng and Y. Luo, "Designed oxygen carriers from macroporous LaFeO3 supported CeO2 for chemical looping reforming of methane," *Applied Catalyst B: Environmental,* vol. 202, pp. 51-63, 2017.

[30] A. Weidenkaff, A. Steinfeld, A. Wokaun, B. Eichler and A. Reller, "The direct solar thermal dissociation of ZnO: Condensation and crystallization of Zn in the presence of oxygen," *Solar Energy,* vol. 65, pp. 59-69, 1999.

[31] M. E. Gàlvez, P. G. Loutzenhiser, I. Hischier and A. Steinfeld, "CO2 splitting via two-step solar thermochemical cycles with Zn/ZnO and FeO/Fe3O4 redox reactions: thermodynamic analysis," *Energy & Fuels,* no. 15, pp. 3544-3550, 2008.

[32] R. Palumbo, J. Lede, O. Boutin, E. Ricart, A. Steinfeld, S. Moller, A. Weidenkaff, E. A. Fletcher and J. Bielicki, "The production of Zn from ZnO in a high-temperature solar decomposition quench process - I. The scientific framework for the process," *Chemical Engineering Science,* vol. 53, pp. 2503-2517, 1998.

[33] Z. Yu, Y. Yang, S. Yang, Q. Zhang, J. Zhao, Y. Fang, X. Hao and G. Guan, "Iron-based oxygen carriers in chemical looping conversions: A review," *Carbon Resources Conversion,* vol. 2, pp. 23-34, 2019.

[34] W. C. Cho, D. Lee, C. H. Kim, H. S. Cho and S. D. Kim, "Feasibility study of the use of by-product iron oxide and industrial off-gas for application to chemical looping hydrogen production," *Applied Energy,* vol. 216, pp. 466-481, 2018.

[35] Z. Ma, R. Xiao and L. Chen, "Redox reaction induced morphology and microstructure evolution of iron oxide in chemical looping process," *Energy Conversion and Management,* vol. 168, pp. 288-295, 2018.

[36] A. E. Farooqui, J. Llorca and M. Santarelli, "Reactivity assessment and oxidation kinetic model for CO2 splitting on Fe-based oxygen carrier," March 2019.

[37] T. Nakamura, "Hydrogen production from water utilizing solar heat at high temperatures," *Solar Energy,* vol. 19, pp. 467-475, 1977.

[38] S. Abanades and H. I. Villafán-Vidales, "CO2 valorisation based on Fe3O4/FeO thermochemical redox reactions using concentrated solar energy," *International Journal of Energy Research,* vol. 37, pp. 598-608, 2013.

[39] S. Abanades and H. I. Villafan-Vidales, "CO2 and H2O conversion to solar fuels via two-step solar thermochemical looping using iron oxide redox pair," *Chemical Engineering Journal,* vol. 175, p. 368–375, 2011.

[40] C. Lu, K. Li, H. Wang, X. Zhu, Y. Wei and M. Zheng, "Chemical looping reforming of methane using magnetite as oxygen carrier: structure evolution and reduction kinetics," *Applied Energy,* vol. 211, pp. 1-14, 2018.

[41] E. R. Monzam, R. W. Breault, R. Siriwardane, G. Richards and S. Carpenter, "Kinetics of the reduction of hematite (Fe2O3) by methane (CH4) during chemical looping combustion: A global mechanism," *Chemical Engineering Journal,* vol. 232, pp. 478-487, 2013.

[42] M. Zhu, Y. Song, S. Chen, M. Li, L. Zhang and W. Xiang, "Chemical looping dry reforming of methane with hydrogen generation on Fe2O3/Al2O3 oxygen carrier," *Chemical Engineering Journal,* vol. 368, pp. 812-823, 2019.

[43] J. Scheffe, D. Weibel and A. Steinfeld, "Lanthanum–Strontium–Manganese Perovskites as Redox Materials for Solar Thermochemical Splitting of H2O and CO2," *Energy & Fuels,* vol. 27, p. 4250–4257, 2013.

[44] A. H. McDaniel, E. C. Miller, D. Arifin, A. Ambrosini, E. N. Coker, R. O'Hayre, W. C. Chueh and J. Tong, "Sr- and Mn-doped LaAlO3_δ for Solar Thermochemical H2 and CO Production," *Energy & Environmental Science,* vol. 6, pp. 2424-2428, 2013.

[45] E. Alonso, C. Pérez-Rábago, J. González-Aguilar and M. Romero, "A Novel Lab-scale Solar Reactor for Kinetic Analysis of Non-volatile Metal Oxides Thermal Reductions," *Energy Procedia,* vol. 57, pp. 561-569, 2014.

[46] W. Chueh and S. Haile, "Ceria as a Thermochemical Reaction Medium for Selectively Generating Syngas or Methane from H2O and CO2," *ChemSusChem,* vol. 2, pp. 735-739, 2009.

[47] A. Riaz, M. U. Ali, T. G. Enge, T. Tsuzuki, A. Lowe and W. Lipiński, "Concentration-Dependent Solar Thermochemical CO2/H2O Splitting Performance by Vanadia–Ceria Multiphase Metal Oxide Systems," *Research,* pp. 1-12, 2020.

[48] M. Portarapillo, A. Aronne, A. Di Benedetto, C. Imparato, G. Landi and G. Luciani, "Syngas Production through H2O/CO2 Thermochemical Splitting," *Chemical Engineering Transactions,* vol. 74, pp. 43-48, 2019.

[49] B. Wei, R. Fakhrai, B. Saadatfar, G. Mohan and T. Fransson, "The Design of a Solar-driven Catalytic Reactor for CO2 Conversions," *Energy Procedia,* vol. 57, pp. 2752-2761.

[50] J. Pye and M. Dennis, "Receivers for concentrating solar power," 2019.

[51] P. d. Torino, "ENERGY CENTER Politecnico di Torino," [Online]. Available: http://www.energycenter.polito.it/chi_siamo.

[52] E. M. srl, "MANUALE USO E MANUTENZIONE Concentratore solare a disco," 2019.

[53] J. Pye, "Concentrator optics," 2019.

[54] F. Orsini, "Experimental and numerical analysis of thermochemical cycles using cerium oxides and iron oxides," 2020.

[56] H. Meskine, V. Albin, M. Cassir, A. Ringuedé and V. Lair, "Electrochemical investigations on CO2 reduction mechanism in molten carbonates in view of H2O/CO2 co-electrolysis," *International Journal of Hydrogen Energy,* pp. 1-9, 2020.

[57] C. Agrafiotis, M. Roeb and C. Sattler, "A review on solar thermal syngas production via redox pair-based water/carbon dioxide splitting thermochemical cycles," *Renewable & Sustainable Energy Reviews,* vol. 42, pp. 254-285, 2015.

[58] M. Galvez, A. Frei, G. Albisetti, G. Lunardi and A. Steinfeld, "Solar hydrogen production via a two-step thermochemical process based on MgO/Mg redox reactions-Thermodynamic and kinetic analyses," *International Journal of Hydrogen Energy,* vol. 33, no. 12, pp. 2880-2890, 2008.